

Development of n-type organic
semiconductors toward Mott-type Field-
effect-transistor investigation

Tianchai Chooppawa

Doctor of Philosophy

Department of Structural Molecular Science

School of Physical Sciences

SOKENDAI (The Graduate University for

Advanced Studies)

Development of n-type organic semiconductors toward Mott-type Field-effect-transistor investigation

Tianchai Chooppawa

A Thesis Submitted in Partial Fulfillment of the Requirements for the

Degree of Doctor of Philosophy

Department of Structural Molecular Science

School of Physical Sciences

The Graduate University for Advanced Studies (SOKENDAI)

Academic Year 2018

Copyright of SOKENDAI

Contents

	Page
Abstract	1
Chapter 1 Introduction	2
Chapter 2 Development of monolayer n-type field-effect-transistor	33
<u>Tianchai Chooppawa</u> , Masayuki Suda, Mikio Uruichi, Manaschai Kunaseth, Supawadee Namuangruk, Paitoon Rashatasakhon and Hiroshi M. Yamamoto, “Development of highly soluble perylenetetracarboxylic diimide derivative for n-type monolayer field-effect-transistor” <i>Molecular Crystals and Liquid Crystals</i> (Accepted) (Included in this thesis)	
Chapter 3 Field effect measurements on n-doped acceptor films	79
Chapter 4 Conclusion	102
Chapter 5 Appendix	103
Acknowledgements	121
List of Publications	122

Abstract

The author has designed 1,7-dibromo-*N,N'*-ditridecyl-3,4,9,10-perylenetetracarboxylic diimide (DB-PTCDI-C13) for the development of novel monolayer field-effect-transistor (FET) where the molecule is expected to show Mott-insulating state after n-type doping. Functionalization of PTCDI core with long alkyl chain and bulky bromine resulted in high solubility, and monolayer n-type FET device could be fabricated via solution deposition processes. Annealing effect of spin coated films and drop casted films have been discussed by dynamic force microscopy (DFM) and optical microscope images. From Differential Scanning Calorimetry (DSC) thermogram, liquid crystalline phase of DB-PTCDI-C13 played an important role to control the film morphology and mobility. The highest mobility of DB-PTCDI-C13 film was $5.8 \times 10^{-3} \text{ cm}^2/\text{V s}$ after annealing at 160°C for 1 hour. However, monolayer spin coated DB-PTCDI-C13 devices showed no FET behavior after potassium doping. On the other hand, synthesized K(TCNQ) crystals laminated on bottom-gate substrate exhibited p-type FET behavior. As K(TCNQ) is a spin-Peierls insulator based on a high-temperature Mott insulating state, this FET seems to be a first example of strongly-correlated-electron FET comprising acceptor type molecule.

Keywords: perylenetetracarboxylic diimide, field-effect-transistor, strongly correlated electrons

Chapter 1 Introduction

1.1. Organic field-effect-transistor (OFET)

Field-effect transistor (FET) was patented in 1930 by Lilienfeld. The first electric-field-effect on conductivity of organic thin film was measured by Kahng and co-workers in 1960¹. After that, there are some reports in middle of 1980's; for instance, Ebisawa, Kudo, Koezuka and their co-workers independently prepared OFET devices based on polyacetylene, merocyanine, and polythiophene, respectively. The material variety and the concept of charge accumulation can be found in many review papers such as the one by Horowitz published in 1998². OFET consists of metal (such as Au or Al) electrodes such as gate, source, and drain, insulating separator such as SiO₂, and a semiconductor thin film made of organic molecules. In FET, there are three types of operation mode, namely p-type and n-type and ambipolar type. In p-type semiconductor, to turn on the device, a negative gate voltage needs to be applied; and then, holes (positive charge carriers) will be injected into the channel from source/drain electrodes. As a result, the mobile holes convey electricity from source to drain when drain bias is applied (**Figure 1.1.1**). On the other hand, in n-type semiconductor, a positive gate voltage needs to be applied to turn on the device; then, the electrons (negative charge carriers) will be accumulated at the semiconductor/insulator interface. This will make the channel conducting again. In case of ambipolar FET, both electrons and holes work as charge carriers, although the major carrier can be switched depending on the gate voltage. A good conductivity at the ON state can be obtained by larger carriers' mobility, when the size of the FET is given.

OFET is being applied for (possibly) inexpensive, large area, printable and bendable devices³⁻⁵. It has already been used as intelligent ink, identified tag, sensors and light emitting displays⁶⁻⁹. In

molecular orbital, there are 2 important levels; namely HOMO (Highest Occupied Molecular Orbital) and LUMO (Lowest Unoccupied Molecular Orbital). HOMO is the highest level that contains electron while LUMO is the lowest electron vacancy level. Although hole mobility in HOMO band (p-type FET) and/or electron mobility in LUMO band (n-type FET)¹⁰ are important, other factors such as the contact resistance, ON/OFF ratio, and subthreshold swing are also important in practical use. Depending on the HOMO/LUMO levels of the molecules with respect to the work function of the electrodes, the injection barrier, or contact resistance, will be affected.

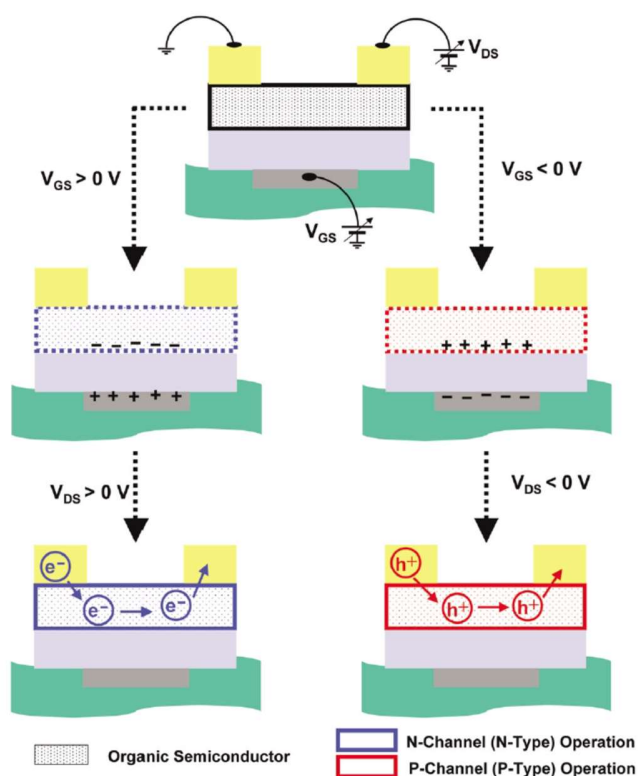


Figure 1.1.1 Schematic of p- and n- transistor¹⁰

Before the application of gate voltage, HOMO and LUMO are located at certain energy levels. For p-type FET, after applying a negative gate voltage, both HOMO and LUMO levels of the channel material are shifted up (**Figure 1.1.2c**). This will allow the energy level matching

between HOMO and Fermi level of the electrodes, when the hole carriers can flow into the FET channel. On the other hand, after applying a positive gate voltage, the HOMO and LUMO levels of n-type material are shifted down and then electron can flow into the channel¹¹.

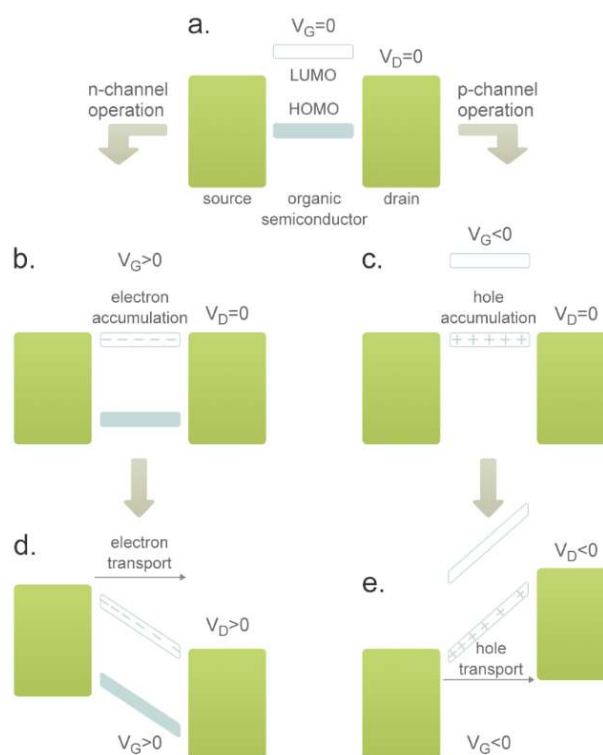


Figure 1.1.2 (a) Idealized energy diagram of OFET at $V_G = V_D = 0$. (b) At $V_G > 0$ and $V_D = 0$ (c) At $V_G > 0$ and $V_D > 0$ (d) at $V_G < 0$ and $V_D = 0$ (e) at $V_G < 0$ and $V_D < 0$ ¹¹.

Besides the above classification between p-type and n-type, one can also classify OFET devices via contact type, where top contact and bottom contact are typical. When the organic layer is deposited onto a bottom gate substrate before source and drain electrode preparation, this device is called top contact type (top-contact & bottom-gate). On the other hand, for bottom contact type,

source and drain electrodes are prepared before organic layer deposition (bottom-contact & bottom-gate) (**Figure 1.1.3**).

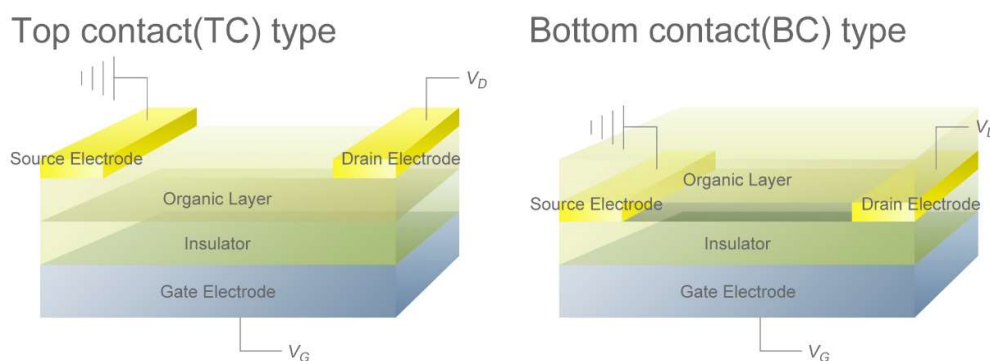
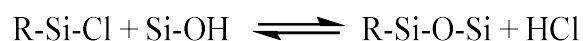


Figure 1.1.3 Scheme of top contact device and bottom contact device in OFET¹¹

To improve the semiconductor-insulator interface, self-assembled monolayer (SAM) is commonly used. This concept has been developed since 1978¹²⁻¹⁴. The substrate and a molecular layer are linked by chemical bond to improve wettability, work function, and flatness of the insulator surface. The popular derivatives used for SAM formation are phosphonic acids and chlorosilanes.

Especially, chlorosilanes are attractive reagent for SAM. They were used as dielectric layer¹⁵⁻¹⁸. The formation of monolayer follows the provided equation:



From the equations, hydroxyl moieties on substrate reacted with chlorosilane reagent to make crosslinks by R-Si-O-Si bonding. However, silane reagent is sensitive to moisture which lead to self-condensation.

1.2. Band insulator

In solid state, the electrons' energy becomes continuous to form energy bands. Valence band (VB) comprises HOMO, while conduction band (CB) comprises LUMO. If there is no doped carrier either in the VB nor CB, the solid becomes a semiconductor or an insulator (**Figure 1.2.1**). If the band gap between VB and CB is much larger than room temperature, typically more than 4 eV, it is called an insulator because there is no thermally excited carrier. If there are intrinsic carriers in CB, the solid becomes a metal.¹⁹

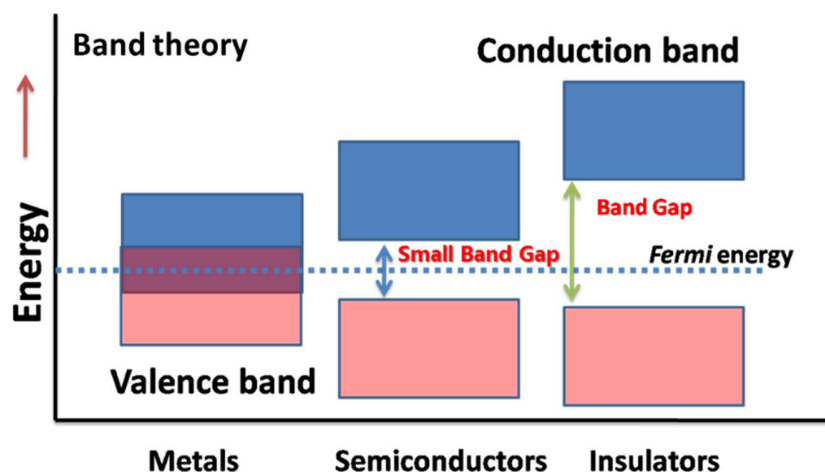


Figure 1.2.1 Metal, semiconductor and insulator in band theory²⁰

1.3. Charge-transfer salt

In 1954, Inokuchi and co-workers reported perylene-bromine complex that showed high conductivity as an organic material. This kind of material is very interesting because π -electronic compound can be oxidized or reduced by doping²¹ to capture conductivity. In this case, the band becomes partially filled because of the chemical doping. Not only oxidized donor molecules such

as perylene, but also reduced acceptor molecules such as TCNQ turned out be conducting after studies by many researchers.

1.4. Mott insulator and Mott FET

The band theory explains most of the conducting properties of the materials. However, Sir. Nevill Mott started to explain the reason why NiO (Nickel(II) oxide) becomes insulating, even though it should be metallic in terms of band theory, from different point of view. In his new theory, since Coulomb repulsion is strong among the carriers, an energy gap which is called Mott-Hubbard gap is formed. The Coulomb interaction called 'on-site Coulomb repulsion' generates empty UHB (upper Hubbard band) and filled LHB (lower Hubbard band) from half-filled band (**Figure 1.4.1**). The transportation of electrons is gapped in energy unless transfer energy is increased by pressure or band filling is modified by doping. If the channel semiconductor is replaced with Mott insulator,

theoretically, FET switching is possible in channel Mott insulator by applying gate voltage, or electrostatic doping.

After doping, the channel of Mott FET should be changed into a metal. Due to the commensulability between the carrier density and the lattice, Mott insulator becomes insulating only when the band filling is just half. This means that the Mott FET exhibits ambipolar behavior because both holes and electrons can make the channel layer metallic. The advantages of Mott FET are numerous. For instance, narrow channel length can be achieved, when the short channel tunneling effect is suppressed.

Mott FET has been theoretically proposed as a high performance device and been realized in

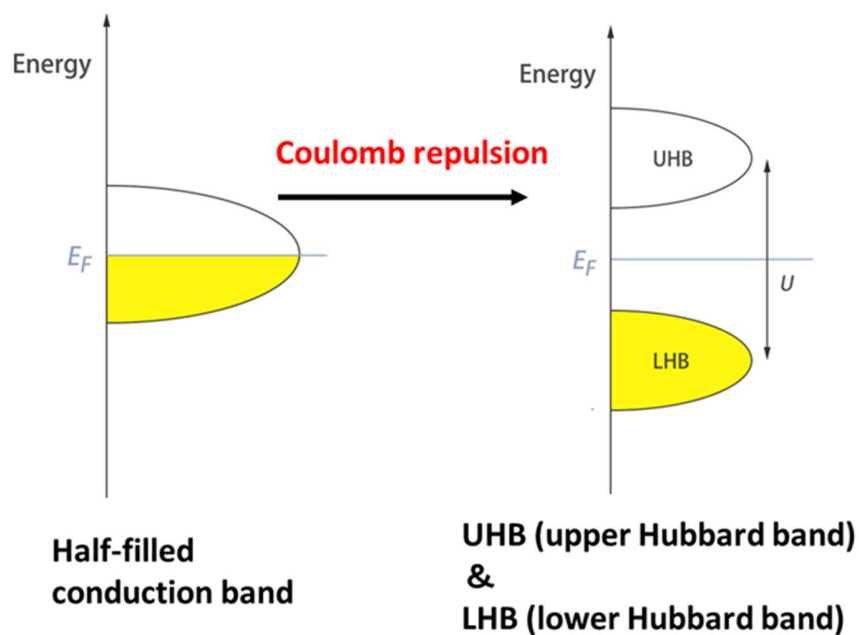


Figure 1.4.1 Half-filled conduction band separates into upper Hubbard band and lower Hubbard band because of Coulomb repulsion, creating Mott insulator.

inorganic devices by Newns and co-workers. They also proposed that the odd number of electron per unit cell results in an organic Mott insulating state²²⁻²⁴. Appropriate organic materials for this purpose are charge transfer salts²⁵⁻²⁸ and κ -type BEDT-TTF (bis(ethylenedithio)tetrathiafulvalene) cation radical salts are proved to show electric field induced Mott transition and superconducting transition²⁹⁻³⁰. Recently, the laboratory the author belongs to have also achieved room temperature operation of monolayer Mott FET when self-assembled-monolayer (SAM) of BEDT-TTF is heavily doped with F4-TCNQ(2,3,5,6-Tetrafluoro-7,7,8,8-tetracyanoquinodimethane)³¹.

1.5 One-dimensional conductor and Pierls instability

Beside electron donating molecules like BEDT-TTF, electron accepting molecules are also eligible for being Mott-insulator after n-type doping. In order to expand material diversity, it seems interesting to find a good acceptor molecule for Mott FET. Tetracyanoquinodimethane (TCNQ) is a well-known molecule for charge transfer complex formation, but its Mott FET operation is not known for the moment.

Doping TCNQ with electron donating reagents will result in a charge-transfer complex. As a result, high conductivity is obtained. For example, NMP-TCNQ (N-methyl-phenazinium-7,7,8,8-tetracyanoquinodimethanide) exhibits metallic behavior upon cooling to 200 K³².

When TCNQ was mixed with TTF, the resulting salt showed good conducting properties³³ and one-dimensional packing³⁴. However, because of high planarity of TCNQ, it easily formed one-dimensional conductor and changed into insulator upon cooling to 60 K because of Peierls instability in one-dimensional conductor (**Figures 1.5.1 & 1.5.2**).

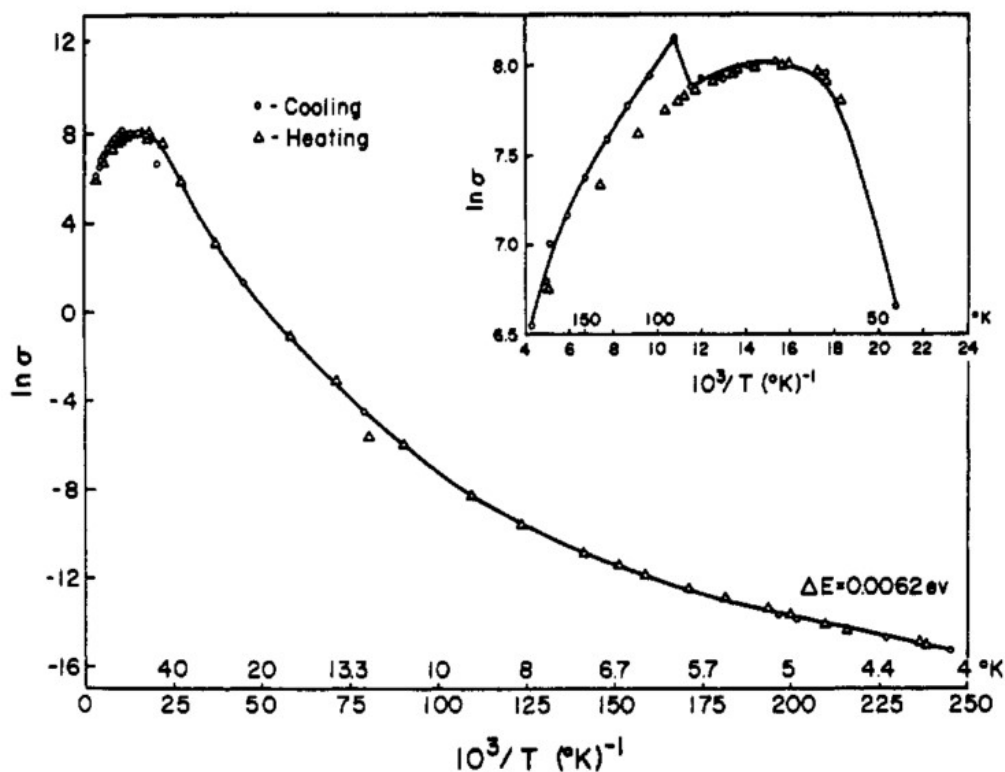


Figure 1.5.1 Temperature dependent conductivity of TTF-TCNQ charge transfer complex.

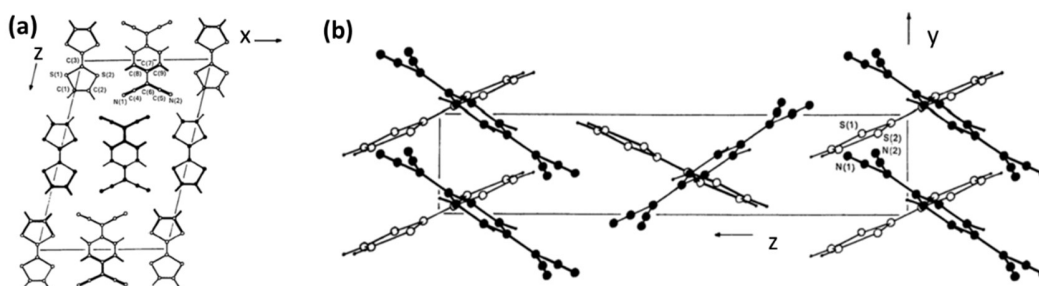


Figure 1.5.2 Single crystal structure of TTF-TCNQ. a) A view along y axis. b) A view along x axis. Both TTF and TCNQ showed one-dimensional stacking independently in single crystal.

To clarify the Peierls's concept, a diagram below (**Figure 1.5.3**) is used to describe the behavior of one-dimensional conductor. The black circle stands for crystal lattice. Upon cooling,

dimerization is formed because the band gap formed by dimerization can stabilize the electron energy. The deformation of crystal lattice is called Peierls's distortion. As a result, it shows insulating behavior due to band gap formation.

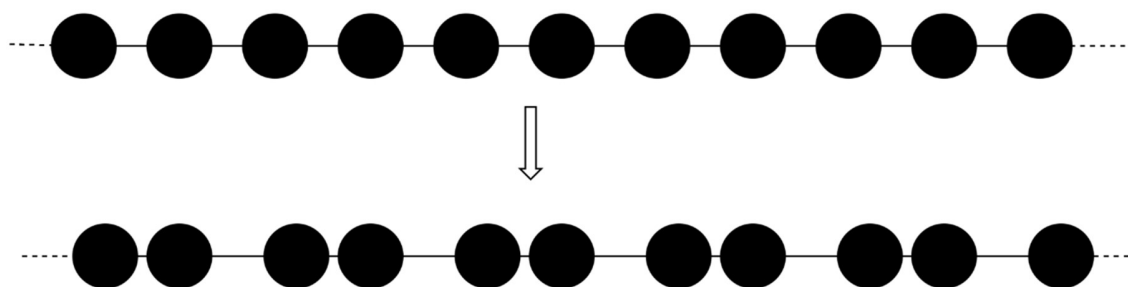


Figure 1.5.3 A brief scheme of Peierls distortion along one-dimensional chain. Filled black circle stands for crystal lattice. At first, each lattice have the same distance from neighboring one. If Peierls distortion occurs, dimerization of lattice will make crystal lattice dimerized (half-filling case) and this will create insulator phase.

In some of the TCNQ salts, one-dimensional Mott-insulating state can be obtained. But because of the Pierls instability mentioned above, they tend to form a lattice distorted material. For example K-TCNQ form spin-Peierls insulator at 345 K, although it is pure Mott-insulator at higher temperature. Nevertheless, one can expect corruption of underlying Mott-insulating phase even at room temperature when band-filling is modulated by electrostatic doping. Not only TCNQ, there are several compounds for doping (**Figure 1.5.4**)

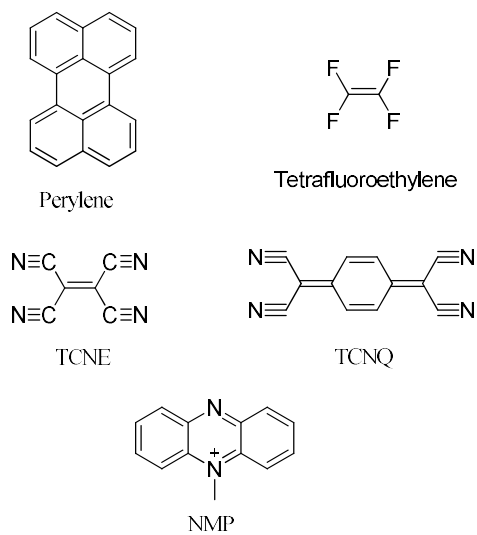


Figure 1.5.4 Molecular structures of perylene, tetrafluoroethylene, TCNE, TCNQ and NMP.

1.6. Perylene

Among n-type organic semiconductors, one of the most brilliant materials is 3,4,9,10-perylene-tetracarboxylic diimide derivatives (PTCDIs)³⁵. PTCDIs are used not only in FET application but also as organic light emitting transistor (OLET)³⁶, inverter³⁷⁻³⁸, chemical sensor³⁹ and organic photovoltaic (OPV)⁴⁰ since they have shown high electron mobility⁴¹⁻⁴³ due to strong π - π interaction of perylene core.

To enhance the efficiency, self-assembled monolayers (SAMs)⁴⁴ and silsesquioxane copolymer⁴⁵ were employed as dielectric layer and the mobility values were found to be increased due to forming of highly crystalline layer via hydrophobic interaction. Instead of forming SAMs on substrate, long-alkyl-chain-attached *N*-alkyl perylene diimide compounds were synthesized. It is reported that strong hydrophobic interaction of long chain could prevent the migration of first monolayer into bulk aggregate; as a result, electron mobility was enhanced after annealing (**Figure 1.6.1**)⁴⁶.

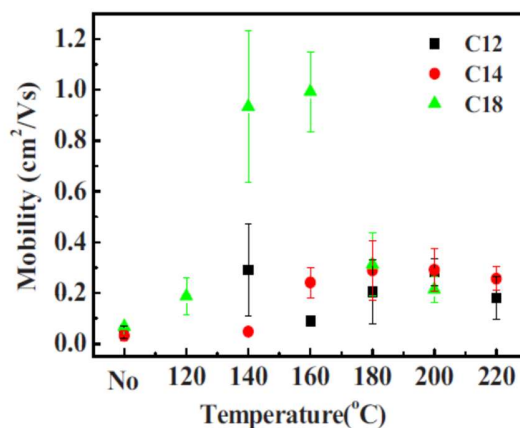


Figure 1.6.1 Electron mobility of various PTCDI with thermal treatment²⁷

Especially, *N,N'*-ditridecyl PTCDI (PTCDI-C13) is an attractive molecule for air stable OFET⁴¹ because of high electron mobility (2.1 cm²/V s) after annealing³⁵(**Figure 1.6.2**). Basically,

evaporation in high vacuum is employed to deposit those PTCDI films because of their poor solubility, to result in films with several molecular layer thickness⁴⁷⁻⁵⁰. In case of making Mott FET, however, monolayer or bilayer PTCDI film is necessary as it requires direct deposition of dopants. This situation drove us to investigate solution processable PTCDI derivatives.

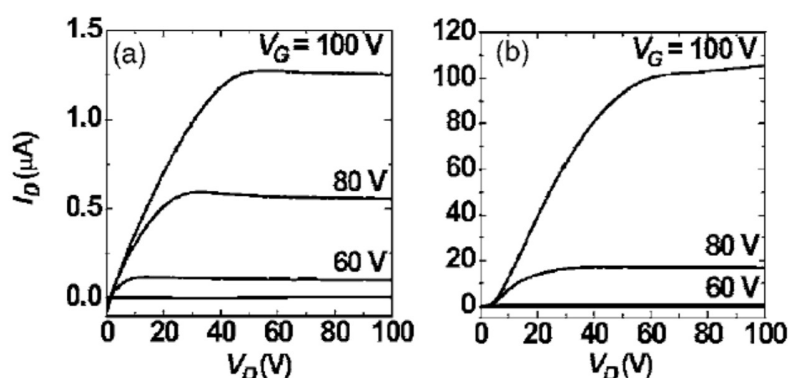


Figure 1.6.2 I_D - V_D of 30 nm PTCDI-C13 film (a) before (b) after annealing 140 °C³⁵

Perylene-3,4,9,10-tetracarboxylic diimide (PTCDI) was also used for preparing coronene derivatives. For instance, Wei Jiang and co-workers have successfully synthesized pyridyl-fused perylene bisimides in one pot. After Suzuki cross-coupling, light was used to prepare core-extended perylene bisimides whose photophysical properties were investigated in THF⁵¹ (**Figure 1.6.3**).

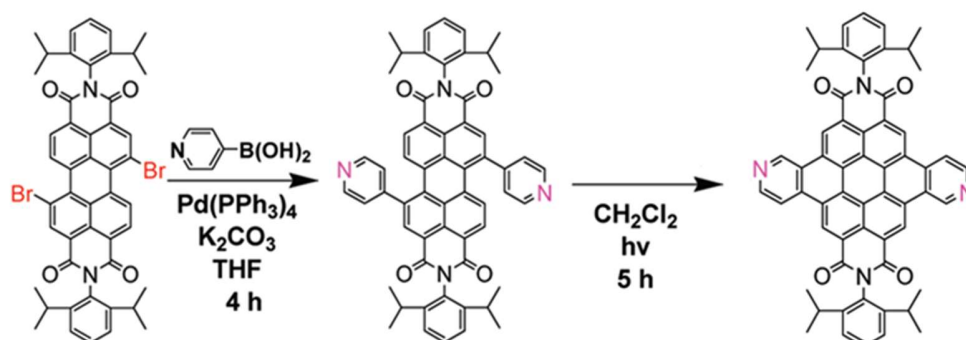


Figure 1.6.3 Synthesis route for pyridyl-fused perylene bisimides⁵¹

Müllen group also reported core-expanded perylenebis(dicarboximide) with which palladium catalyst was used to assist cycloaddition into adducts (**Figure 1.6.4**). The absorption bands were between 400 and 500 nm which displayed greenish-yellow appearance⁵².

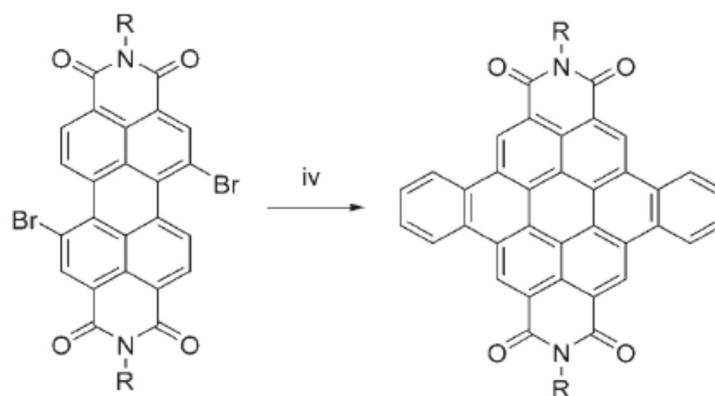


Figure 1.6.4 Synthesis route for core-expanded rylenebis(dicarboximide) (R = n-octyl; iv stands for 2-(trimethylsilyl)phenyl trifluoromethanesulfonate, [Pd(dba)₂], P(o-tolyl)₃, CsF, 110 °C, 24 h)⁵²

Not only pyridyl-fused perylene bisimides⁵¹, methoxynaphthoperylenetetracarbox diimide derivative (**Figure 1.6.5**) was achieved after exposure to light in the methylene chloride⁵³.

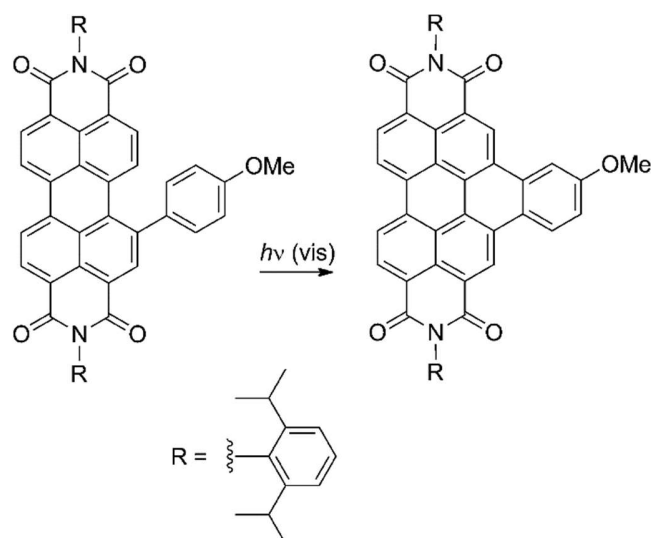


Figure 1.6.5 Synthesis route for methoxynaphthoperylenetetracarbox diimide derivative ⁵³

Furthermore, 1,7-difluoro-perylene-3,4,9,10-tetracarboxylic dianhydride (DF-PTCDA) was condensed with 1,2-phenylenediamine to obtain benzimidazole derivatives; however, crude mixtures of regioisomers were purified by triple sublimation in a three-zone sublimation unit. The highest mobility was $6.2 \times 10^{-5} \text{ cm}^2/\text{V s}$ at 125°C ⁵⁴. (**Figure 1.6.6**)

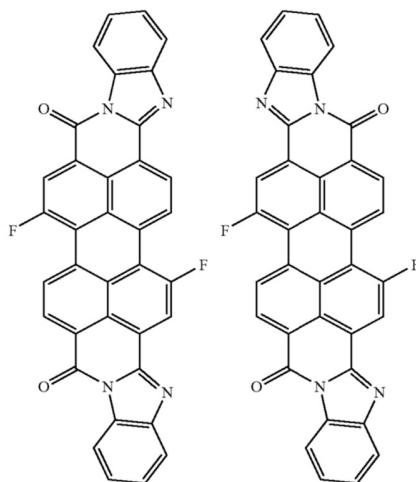


Figure 1.6.6 Structure of benzimidazole derivatives in a patent⁵⁴

In 1997, Heribert Quante and co-workers reported absorption and emission properties of syn/anti 1,6,7,12-tetrakis(aryloxy)-3,4,9,10-perylenetetracarboxdiimide derivatives in methylene

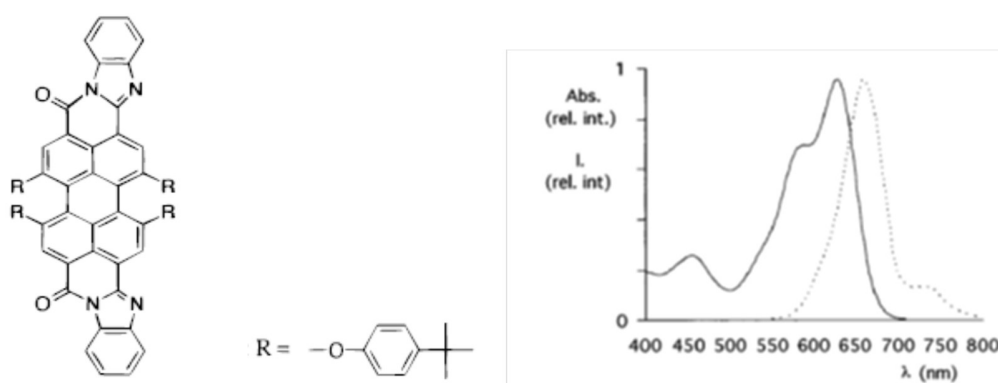


Figure 1.6.7 Structure and normalized absorption and emission spectrum of 1,6,7,12-tetrakis(aryloxy)-3,4,9,10-perylenetetracarboxdiimide derivatives⁵⁵

chloride at room temperature (**Figure 1.6.7**). This suggests that the introduction of substituent on perylene core might improve the solubility⁵⁵.

Not only aryloxy group, but CF_3 group in bis(trifluoromethyl)-substituted-3,4,9,10-perylene tetracarboxylic bis(benzimidazole) regioisomers were also reported in terms of absorption and emission spectrum in dichloromethane. The author assumes that the introduction of bulky CF_3 groups on perylene core might improve the solubility because of a possible twist of perylene core via steric effect⁵⁶. (**Figure 1.6.8**)

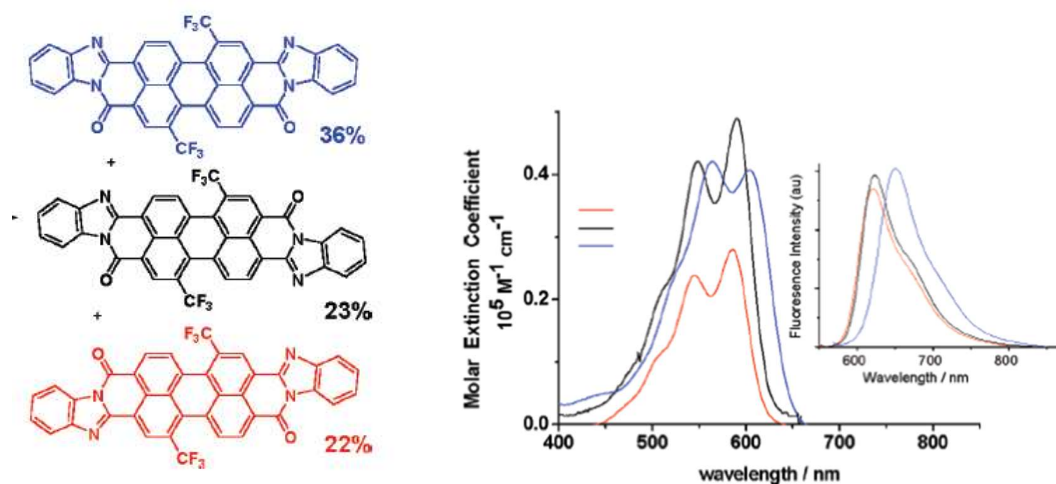


Figure 1.6.8 Structure and normalized absorption and emission spectrum of bis(trifluoromethyl)-substituted-3,4,9,10-perylene tetracarboxylic bis(benzimidazole) regioisomers⁵⁶

Asymmetric soluble perylene imide benzimidazole was synthesized and liquid crystalline properties were found (**Figure 1.6.9**). The alkyl chain was introduced to increase solubility. In conclusion, UV absorption spectrum was revealed in CHCl_3 ⁵⁷.

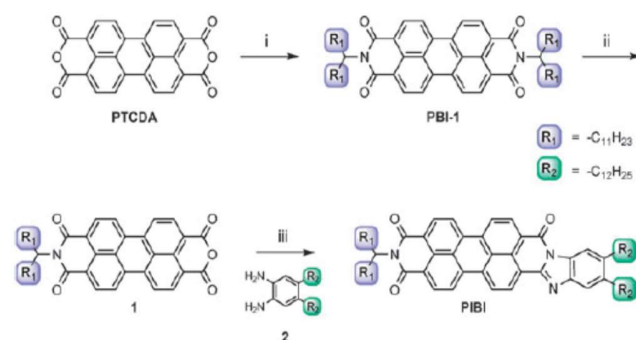


Figure 1.6.9 Synthesis of asymmetric soluble perylene imide benzimidazole⁵⁷

A thin film of perylenebis-benzimidazole was fabricated on polymer gate dielectric. The researchers found that the OFET performance was dominated by gate dielectric. The highest mobility is $1.6 \times 10^{-4} \text{ cm}^2/\text{V s}$ on poly-benzocyclobutane gate dielectric (**Figure 1.6.10**). However, Thermal evaporation process was employed to coat perylenebis-benzimidazole layer⁵⁸, which prevented monolayer formation.

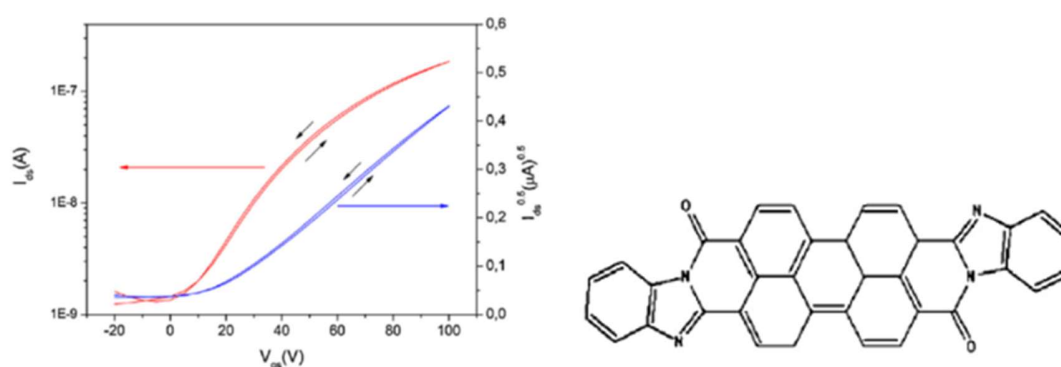


Figure 1.6.10 I_d - V_g and $I_d^{1/2}$ - V_g characteristics of Perylenebis-benzimidazole on benzocyclobutane⁵⁸

1.7. Coating technique

Basically, there are 2 types of coating technique for OFETs, namely molecular evaporation process and solution-deposition process. However, molecular evaporation process requires high vacuum and large energy for heating. This technique is not appropriate for the author's purpose because it is forming a rather thick layer than monolayer. In this context, the author concentrated in solution-deposition process⁵⁹. There are plenty of solution-deposition processes. For instance, the author describes popular technique such as dip coating, spin coating and drop casting. To coat the substrate, the compound needs to be dissolved in solvent. After solvation, it will be coated by variety of technique.

For dip coating, the substrate is immersed in the solution and is lifted. This technique should be optimized by changing lifting speed and concentration of solution. A monolayer was obtained in some cases⁶⁰⁻⁶¹.

Many compounds such as 5T⁶² and 7T⁶³ (septithiophene) are successfully coated by spin coating method. Briefly speaking, the solution was dropped on substrate and dried by spinning. This technique should be optimized by changing spin speed, solvent and concentration of solution.

About drop casting, the film is prepared by dropping the solution on the substrate and dried at ambient condition. This technique should be optimized by changing solvent and concentration of solution.

PTCDIs film has been prepared by Langmuir-Blodgett (LB) technique. However, the preparation process is complicated, and it was not successful in forming a uniform layer⁶⁴. Singh and co-workers had synthesized *N,N'*-bis-(1-pentyl)hexyl-3,4,9,10-perylene diimide and fabricated thin films with its solution in chlorobenzene to measure FET properties, but spin-coated monolayer film was not obtained and mobility was only $5 \times 10^{-4} \text{ cm}^2/\text{V s}$ ⁶⁵. **(Figure 1.7.1)**

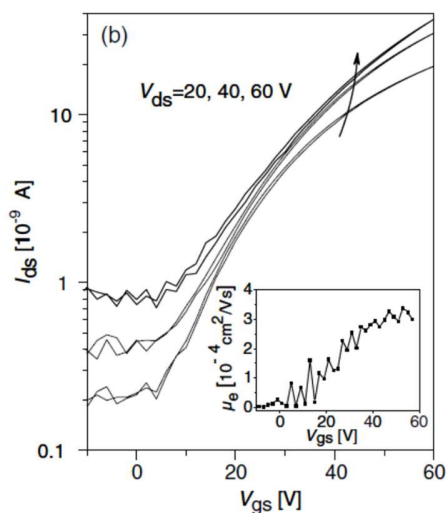


Figure 1.7.1 I_d - V_g of spin coated N,N' -bis-(1-pentyl)hexyl-3,4,9,10-perylene diimide film⁶⁵

In this case, the solubility of PTCDI is low and difficult to prepare the monolayer via solution deposition process which might require solubility in more volatile solvent. Therefore, not only an addition of long alkyl chain but also modification of π -core skeleton seems necessary to obtain a highly soluble material. Recently, in fact, dicyano PTCDI was dip coated to prepare

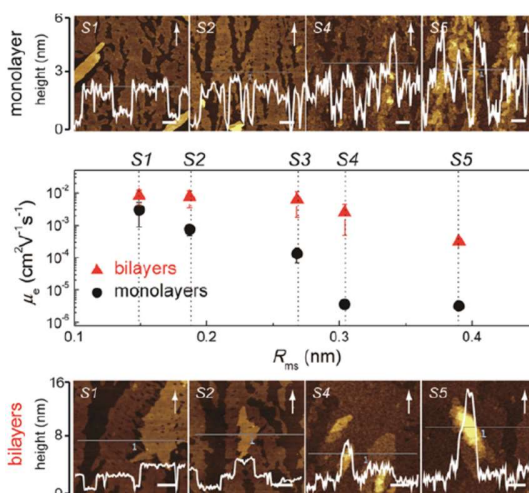


Figure 1.7.2 Mobility and AFM image of monolayer and bilayer dip coated dicyano PTCDI⁶⁶

monolayer or bilayer FET. Therefore, substitution of the π -core of PTCDI is very attractive way to obtain highly soluble PTCDI for n-type FET⁶⁶. (**Figure 1.7.2**)

To improve electronic structure, film should be optimized in terms of morphology, thickness and grain size. In addition to chemical structure⁶⁷, annealing temperature and surface of dielectric layer are important to control film quality which directly relates to electron mobility^{66, 68-70}. High structural ordering is conceived after annealing because spontaneous ordering in liquid crystalline phase can be expected after temperature history, if the molecule has long alkyl chain for example. There are many examples on annealing where device showed higher mobility after annealing⁷¹⁻⁷³.

1.8. Monolayer

One layer of molecules or atoms is called monolayer. Recently, OFET with monolayer film is attracting attention because monolayer FET can be prepared by trace amount of material to obtain the large area devices, which should be able to cut the cost in considerable extent. In fact, monolayer FET sometimes shows mobility larger than original π -core molecules, since charge transport is dominated by carrier motion in the first interface monolayer, even though the thin film may be made of multilayered molecules⁷⁴. In addition to the above advantages, the monolayer is suitable for heavy doping to the organic layer, as the active layer is naked and prone to interact with dopants when they are properly deposited on the top. Heavily doped semiconductor should be interesting as a Mott-insulator-based FET, where insulator-to-metal transition is expected at the channel⁷⁵⁻⁷⁶.

In past decades, there are several methods developed to prepare the monolayer such as Langmuir-Blodgett (LB) film (**Figure 1.8.1**). The requirements for LB film are amphiphilic molecule, immiscible solvent for molecule and surface tension⁷⁷. However, the quality of LB film

is known to be poor. Recent advances in solution process for monolayer formation such as spin-coating and dip-coating seem much better in terms of film quality.

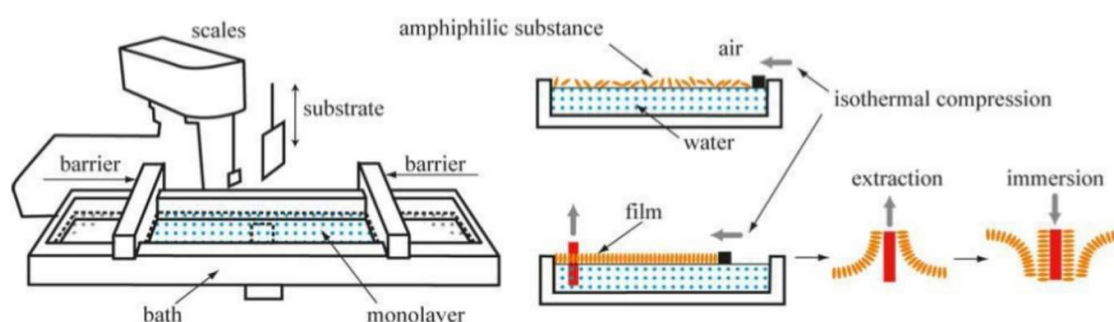


Figure 1.8.1 Langmuir-Blodgett film process⁷⁸

1.9. Objective

In this work, monolayer and bilayer of 1,7-dibromo-*N,N'*-ditridecyl-3,4,9,10-perylenetetracarboxylic diimide (DB-PTCDI-C13) were successfully fabricated by spin coating process. *N*-attached long alkyl chain and bulky and electron-withdrawing substituent (*i.e.* bromine) made synergistic effect which could align the molecular arrangement and could prevent the first layer migration from the substrate. Highly ordered monolayer with better mobility was obtained after annealing. In addition, we performed density functional theory (DFT) calculations to analyze structural and electronic property of DB-PTCDI-C13. Although potassium 1,7-dibromoperylene-tetracarboxylic diimide salt (K_x -(DB-PTCDI-C13)) have never been discussed, we have tried to dope DB-PTCDI-C13 monolayer film by potassium evaporation (**Figure 1.9.1**).

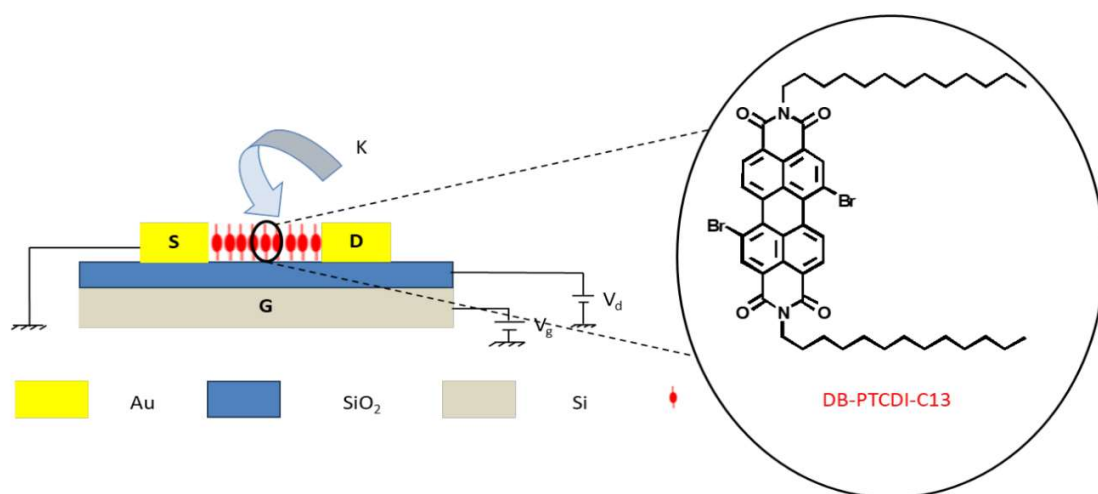


Figure 1.9.1 Conceptual device scheme for monolayer Mott FET prepared by spin-coated DB-PTCDI-C13

Before the author started to focus on DB-PTCDI-C13, the author also synthesized core-extended perylene diimide derivatives which were studied in terms of synthesis, characterization and electrical properties. Although the author was interested in OFET properties of these core-extended perylene diimide derivatives, poor solubility of these materials have prevented the author to study the FET performance. Anyway, the target molecules were designed with N-long alkyl chain, n-tridecyl moiety, for high solubility in organic solvent which might be suitable for solution-deposited process, and variety of hetero atom on boronic acid agents were used as coupling reagent to obtain various core-extended perylene diimide derivatives (**Figure 1.9.2**).

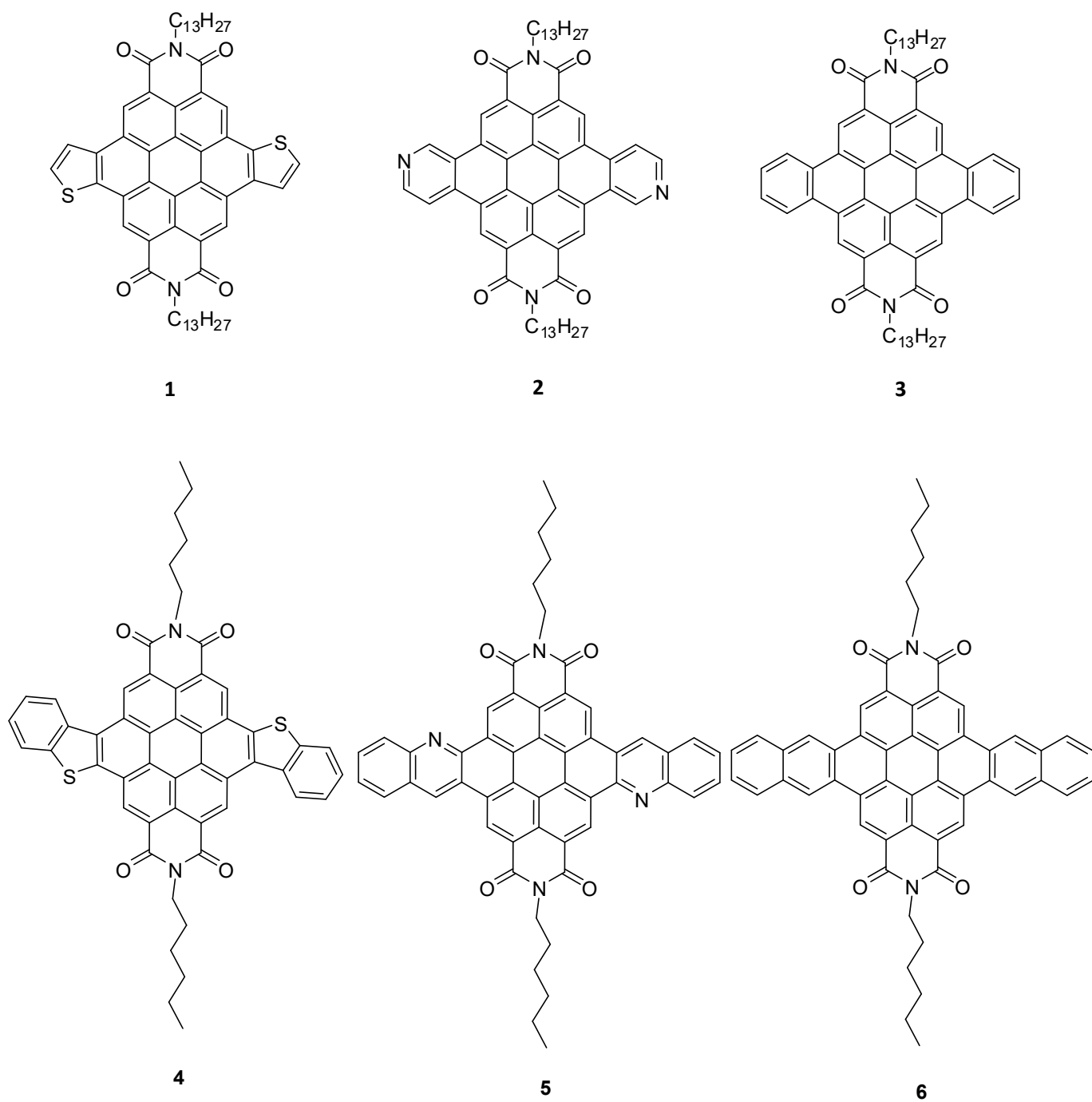


Figure 1.9.2 Our core-extended perylene diimide target compounds

In the same context, alkyl chains were attached to perylenebis-benzimidazole to enhance the solubility in common organic solvent. The author expected that the target perylenebis-benzimidazole can be solubilized to form a thin film for the OFET application via solution deposition process such as spin coating (**Figure 1.9.3**). However, the solubility was not good enough again to obtain a good quality thin film.

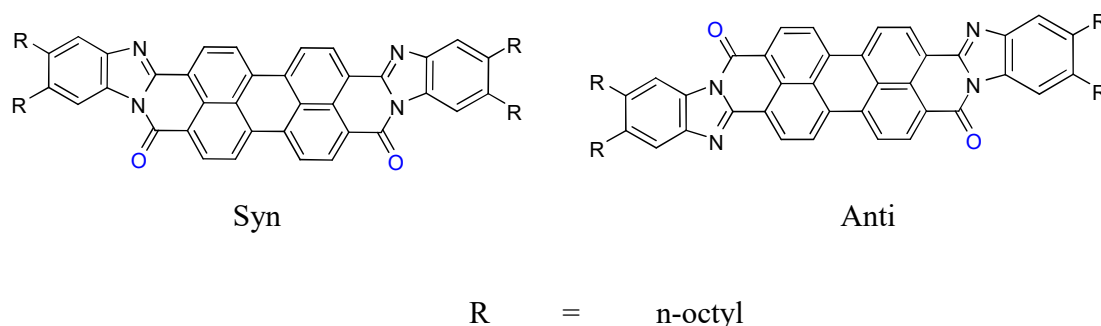


Figure 1.9.3 Target perylenebis-benzimidazole

Finally, the author tested a strongly correlated material K(TCNQ) for FET fabrication. Although monolayer channel could not be obtained by evaporation method, a thin single crystal laminated on SiO₂/Si substrate showed p-type FET behavior.

References

1. J. E. Lilienfeld, U.S. Patent 1745175, 1930; Y. Yamashita, *Sci. Technol. Adv. Mater.* **2009**, *10*, 024313.; D. Kahng, M. M. Atalla, *IRE Solid-State Devices Research Conference*, Carnegie Institute of Technology, Pittsburgh, PA **1960**.
2. F. Ebisawa, T. Kurokawa, S. Nara, *J. Appl. Phys.* **1983**, *54*, 3255.; K. Kudo, M. Yamashina, T. Moriizumi, *J. Appl. Phys.* **1984**, *23*, 130; H. Koezuka, A. Tsumura, T. Ando, *Synth. Met.* **1987**, *18*, 699; A. Tsumura, H. Koezuka, Y. Ando, *Synth. Met.* **1988**, *25*, 11.; G. Horowitz, *Adv. Mater.* **1998**, *10*, 365; Y. Sun, Y. Liu, D. Zhu, *J. Mater. Chem.* **2005**, *15*, 53.
3. A. R. Murphy, J. M. J. Fréchet, *Chem. Rev.* **2007**, *107*, 1066.
4. J. E. Anthony, *Angew. Chem. Int. Ed.* **2008**, *47*, 452.
5. S. Allard, M. Forster, B. Souharce, H. Thiem, U. Scherf, *Angew. Chem. Int. Ed.* **2008**, *47*, 4070.
6. V. Subramanian, P. C. Chang, J. B. Lee, S. E. Moles, S. K. Volkman, *IEEE Trans. Comp. Pack. Tech.* **2005**, *28*, 742.
7. A. Dodabalapur, *Mater. Today.* **2006**, *9*, 24.
8. H. E. Katz, X. M. Hong, A. Dodabalapur, R. Sarpeshkar, *J. Appl. Phys.* **2002**, *91*, 1572.
9. M. Muccini, *Nat. Mater.* **2006**, *5*, 605.
10. A. Facchetti, *Mater. Today.* **2007**, *10*, 28.
11. P. K. Weimer *Proceedings of the IRE* **1962**, *50*, 1462.; F. Yang, Fabrication and operation of monolayer Mott FET at room temperature, Tokyo Institute of Technology, Japan, 2017.
12. W. Bigelow, D. Pickett, W. Zisman. *J. Colloid Sci.* **1946**, *1*, 513.
13. E. Polymeropoulos, J. Sagiv. *J. Chem. Phys.* **1978**, *69*, 1836.
14. J. Sagiv. *J Am Chem Soc* **1980**, *102*, 92.

15. R. Maoz, J. Sagiv. *J Colloid Interf Sci* **1984**, *100*, 465.
16. D. Aswal, S. Lenfant, D. Guerin, J. Yakhmi, D. Vuillaume. *Anal Chim Acta* **2006**, *568*, 84.
17. D. Vuillaume, C. Boulas, J. Collet, J. Davidovits, F. Rondelez. *Appl Phys Lett* **1996**, *69*, 1646.
18. J. Collet, O. Tharaud, A. Chapoton, D. Vuillaume. *Appl Phys Lett* **2000**, *76*, 1941.
19. N. Mott, R. Peierls. *Proceedings of the Physical Society* **1937**, *49*, 72.
20. <https://nirajchawake.wordpress.com/2014/10/20/semiconductors-why-%E2%88%86e%E2%89%A43-2-ev/>
21. H. Akamatu, H. Inokuchi, Y. Matsunaga. *Nature* **1954**, *173*, 168.
22. D. M. Newns, J. A. Misewich, C. C. Tsuei, A. Gupta, B. A. Scott, A. Schrott, *Appl. Phys. Lett.* **1998**, *73*, 780.
23. D. M. Newns, T. Doderer, C. C. Tsuei, W. M. Donath, J. A. Misewich, A. Gupta, B. M. Grossman, A. Schrott, B. A. Scott, P. C. Pattnaik, R. J. V. Gutfeld, J. Z. Sun, *J. Electroceramics*. **2000**, *4*, 339.
24. C. Zhou, D. M. Newns, J. A. Misewich, P. C. Pattnaik, *Appl. Phys. Lett.* **1997**, *70*, 598.
25. J. B. Torrance, *Acc. Chem. Res.* **1979**, *12*, 79.
26. Z. G. Soos, *Chem. Phys. Lett.* **1979**, *63*, 179.
27. M. Sakai, H. Sakuma, Y. Ito, A. Saito, M. Nakamura, K. Kudo, *Phys. Rev. B.* **2007**, *76*, 045111.
28. T. Hasegawa, K. Mattenberger, J. Takeya, B. Batlogg, *Phys. Rev. B.* **2004**, *69*, 245115.
29. H. M. Yamamoto, M. Nakano, M. Suda, Y. Iwasa, M. Kawasaki, R. Kato, *Nature Commun.* **2013**, *4*, 2379.
30. Y. Kawasugi, H. M. Yamamoto, N. Tajima, T. Fukunaga, K. Tsukagoshi, R. Kato, *Phys. Rev. Lett.* **2009**, *103*, 116801.

31. F. Yang, M. Suda, H. M. Yamamoto, *Bull. Chem. Soc. Jpn.* **2017**, 90, 1259.
32. W. Siemons, P. Bierstedt, E. R. Kepler. *The Journal of Chemical Physics* **1963**, 39, 3523.
33. J. Ferraris, D. Cowan, V. T. Walatka, J. Perlstein. *J Am Chem Soc* **1973**, 95, 948.
34. T. J. Kistenmacher, T. E. Phillips, D. O. Cowan. *Acta Crystallographica Section B: Structural Crystallography and Crystal Chemistry* **1974**, 30, 763.
35. S. Tatemichi, M. Ichikawa, T. Koyama, Y. Taniguchi, *Appl. Phys. Lett.* **2006**, 89, 112108.
36. R. Capelli, J.J. Amsden, G. Generali, S. Toffanin, V. Benfenati, M. Muccini, D.L. Kaplan, F.G. Omenetto, R. Zamboni, *Org. Electron.* **2011**, 12, 1146.
37. Y. J. Jeong, J. Jang, S. Nam, K. Kim, L. H. Kim, S. Park, T. K. An, C. E. Park, *ACS Appl. Mater. Interfaces.* **2014**, 6, 6816.
38. J. D. Oh, J. Kim, D. Kim, J. Choi, *Org. Electron.* **2016**, 30, 131.
39. N. Wu, C. Wang, B. R. Bunes, Y. Zhang, P. M. Slatum, X. Yang, L. Zang, *ACS Appl. Mater. Interfaces.* **2016**, 8, 12360.
40. Y. Hsiao, Y. Liao, H. Chen, P. Chen, F. Chen, *ACS Appl. Mater. Interfaces.* **2016**, 8, 9275.
41. P. R. L. Malenfant, C. D. Dimitrakopoulos, J. D. Gelorme, L. L. Kosbar, T. O. Graham, A. Curioni, W. Andreoni, *Appl. Phys. Lett.* **2002**, 80, 2517.
42. G. Horowitz, F. Kouki, P. Spearman, D. Fichou, C. Nogues, X. Pan, F. Garnier, *Adv. Mater.* **1996**, 8, 242.
43. R. J. Chesterfield, J. C. McKeen, C. R. Newman, P. C. Ewbank, D. A. S. Filho, J. Brédas, L. L. Miller, K. R. Mann, C. D. Frisbie, *J. Phys. Chem. B.* **2004**, 108, 19281.
44. H. Cheng, J. Huai, L. Cao, Z. Li, *Appl. Surf. Sci.* **2016**, 378, 545.
45. W. Kang, G. An, M. J. Kim, W. H. Lee, D. Y. Lee, H. Kim, J. H. Cho, *J. Phys. Chem. C.* **2016**, 120, 3501.

46. H. Jeon, J. Hattori, S. Kato, N. Oguma, N. Hirata, Y. Taniguchi, M. Ichikawa, *J. Appl. Phys.* **2010**, *108*, 124512.
47. J. Roh, J. Lee, C. Kang, C. Lee, B. J. Jung, *Phys. Status Solidi RRL*. **2013**, *7*, 469.
48. S. H. Kim, M. Jang, J. Kim, H. Choi, K. Y. Baek, C. E. Park, H. Yang, *J. Mater. Chem.* **2012**, *22*, 19940.
49. J. Jang, S. Nam, D. S. Chung, S. H. Kim, W. M. Yun, C. E. Park, *Adv. Funct. Mater.* **2010**, *20*, 2611.
50. J. Jang, S. Nam, W. M. Yun, C. Yang, J. Hwang, T. K. An, D. S. Chung, C. E. Park, *J. Mater. Chem.* **2011**, *21*, 12542.
51. W. Jiang, Y. Li, W. Yue, Y. Zhen, J. Qu, Z. Wang, *Org. Lett.* **2010**, *12*, 228.
52. Y. Avlasevich, S. Müller, P. Erk, K. Müllen, *Chem. Eur. J.* **2007**, *13*, 6555.
53. B. Pagoaga, L. Giraudet, N. Hoffmann, *Eur. J. Org. Chem.* **2014**, 5178.
54. M. Könemann, P. Osswald, R. Schmidt, F. Würthner, U.S. Patent 0166614 A1, **2009**.
55. H. Quante, Y. Geerts, K. Müllen, *Chem. Mater.* **1997**, *9*, 495.
56. Z. Yuan, Y. Xiao, Z. Li, X. Qian, *Org. Lett.* **2009**, *11*, 2808.
57. A. Wicklein, P. Kohn, L. Ghazaryan, T. Thurn-Albrecht, M. Thelakkat, *Chem. Comm.* **2010**, *46*, 2328.
58. C. Tozlua, S. Erten-Elab, Th. B. Singh, N. S. Sariciftci, S. Içli, *Synth. Met.* **2013**, *172*, 5.
59. E. M. Mannebach, J. W. Spalenka, P. S. Johnson, Z. Cai, F. Himpsel, P. G. Evans. *Adv Funct Mater* **2013**, *23*, 554.
60. J. Jang, S. Nam, K. Im, J. Hur, S. N. Cha, J. Kim, H. B. Son, H. Suh, M. A. Loth, J. E. Anthony. *Adv Funct Mater* **2012**, *22*, 1005.

61. L. Li, P. Gao, K. C. Schuermann, S. Ostendorp, W. Wang, C. Du, Y. Lei, H. Fuchs, L. D. Cola, K. Müllen. *J Am Chem Soc* **2010**, *132*, 8807.
62. H. Chen, S. Dong, M. Bai, N. Cheng, H. Wang, M. Li, H. Du, S. Hu, Y. Yang, T. Yang. *Adv Mater* **2015**, *27*, 2113.
63. M. Defaux, F. Gholamrezaie, J. Wang, A. Kreyes, U. Ziener, D. V. Anokhin, D. A. Ivanov, A. Moser, A. Neuhold, I. Salzmann, R. Resel, D. M. de Leeuw, S. C. Meskers, M. Moeller, A. Mourran. *Adv Mater* **2012**, *24*, 973.
64. W. J. Doherty, A. G. Simmonds, S. B. Mendes, N. R. Armstrong, S. S. Saavedra, *Appl. Spectrosc.* **2005**, *59*, 1248.
65. Th. B. Singh, S. Erten, S. Günes, C. Zafer, G. Turkmen, B. Kuban, Y. Teoman, N.S. Sariciftci, S. Icli, *Org. Electron.* **2006**, *7*, 480.
66. M. Li, T. Marszalek, Y. Zheng, I. Lieberwirth, K. Müllen, W. Pisula, *ACS Nano.* **2016**, *10*, 4268.
67. X. Zhao, L. Ma, L. Zhang, Y. Wen, J. Chen, Z. Shuai, Y. Liu, X. Zhan, *Macromolecules.* **2013**, *46*, 2152.
68. P. Lutsyk, K. Janus, J. Sworakowski, G. Generali, R. Capelli, M. Muccini, *J. Phys. Chem. C.* **2011**, *115*, 3106.
69. Y. Chou, S. Takasugi, R. Goseki, T. Ishizone, W. Chen, *Polym. Chem.* **2014**, *5*, 1063.
70. L. Mao, J. Gan, J. Hwang, T. Chang, Y. Chueh, *Org. Electron.* **2014**, *15*, 920.
71. C. W. Struijk, A. B. Sieval, J. E. J. Dakhorst, M. Dijk, P. Kimkes, R. B. M. Koehorst, H. Donker, T. J. Schaafsma, S. J. Picken, A. M. Craats, J. M. Warman, H. Zuilhof, E. J. R. Sudhölter, *J. Am. Chem. Soc.* **2000**, *122*, 11057.
72. Y. Xu, S. Leng, C. Xue, R. Sun, J. Pan, J. Ford, S. Jin, *Angew. Chem. Int. Ed.* **2007**, *46*, 3896.

73. M. Funahashi, A. Sonoda, *Org. Electron.* **2012**, *13*, 1633.
74. M. Mottaghi, G. Horowitz, *Org. Electron.* **2006**, *7*, 528.
75. F. Yang, M. Suda, H. M. Yamamoto. *Bull. Chem. Soc. Jpn.* **2017**, *90*, 1259.
76. H. M. Yamamoto, M. Suda, Y. Kawasugi. *Jpn. J. Appl. Phys.* **2018**, *57*, 03EA02.
77. S. Fabiano, C. Musumeci, Z. Chen, A. Scandurra, H. Wang, Y. L. Loo, A. Facchetti, B. Pignataro, *Adv Mater.* **2012**, *24*, 951.
78. <http://eng.thesaurus.rusnano.com/wiki/article1797>

Chapter 2 Development of monolayer n-type field-effect-transistor

2.1 Scope

In chapter 2, the author describes about development of monolayer n-type FET. The author synthesized and characterized perylene diimide derivatives which consist of benzimidazole, coronene and bay-substituted perylene diimide. Among many perylene derivatives, bay-substituted perylene diimide was able to form a monolayer FET. Interestingly, spin coated 1,7-dibromo-*N,N'*-ditridecyl-3,4,9,10-perylenetetracarboxylic diimide (DB-PTCDI-C13) film exhibited improved FET behavior after annealing at 160°C for 1 hour. Annealing temperature, annealing time and modification of the substrate by SAM (Self-Assembled Monolayer) were examined with drop casted film and spin coated film. Not only solution deposition process, but also evaporation method in vacuum chamber was tested. Lastly, the author also tested DB-PTCDI-C18 to study about alkyl length effect.

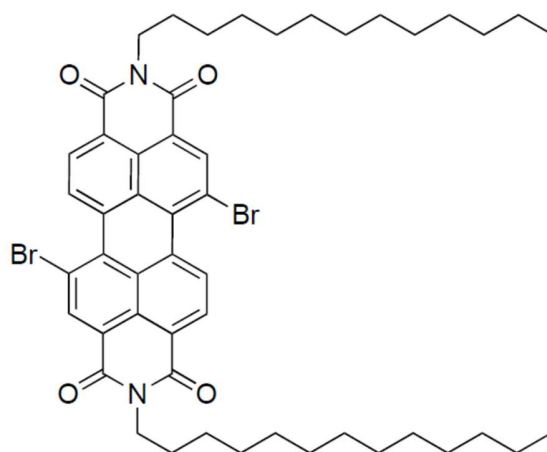
2.2 Experimental

2.2.1 Materials and instruments

1,7-dibromo-perylene-3,4,9,10-tetracarboxylic dianhydride and all boronic acid agents were purchased from Tokyo Chemical Industry (TCI, Japan). 1-aminotridecane, 1-aminooctadecane, propionic acid, tetrabutylammonium bromide, K_2CO_3 , 1-octene, 0.5 M 9-BBN, 4,5-dibromo-1,2-phenylenediamine, potassium iodide, tetrakis(triphenylphosphine) palladium(0) or $Pd(PPh_3)_4$, $PdCl_2(dppf)$ and common solvent were purchased from WAKO Pure Chemical Industries (Japan). All commercially available chemicals were used without purification. P-doped Si substrates covered with a 300 nm-thick SiO_2 layer (SiO_2/Si) were cut into size of 6 by 6 mm². The electrodes were patterned by photo lithography. The Au/Ti electrodes were deposited by sputtering method. The I-V characteristic study was conducted by 4200A-SCS parameter analyzer (Keithley). The temperature was regulated with LS336 temperature controller in combination with manual prober (Lake Shore Cryotronics). The morphology of the device surface was observed by DFM (dynamic force microscopy) while optical images for drop casted film were taken by microscope (Nikon, Japan).

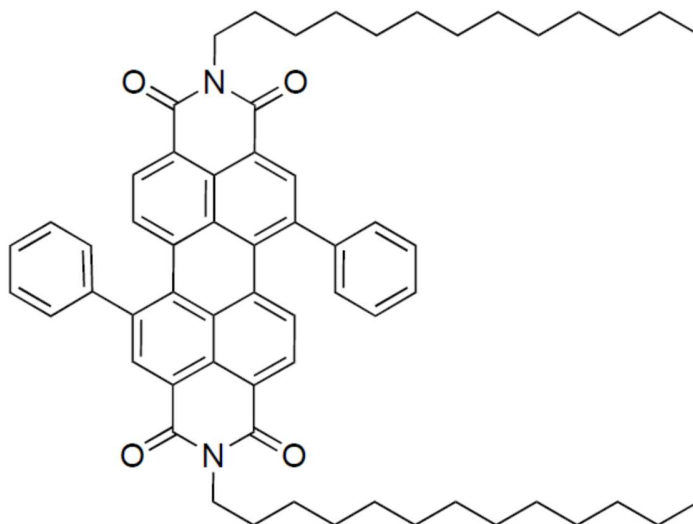
2.2.2 Synthesis

1,7-dibromo-*N,N'*-ditridecyl-3,4,9,10-perylenetetracarboxylic diimide (DB-PTCDI-C13)



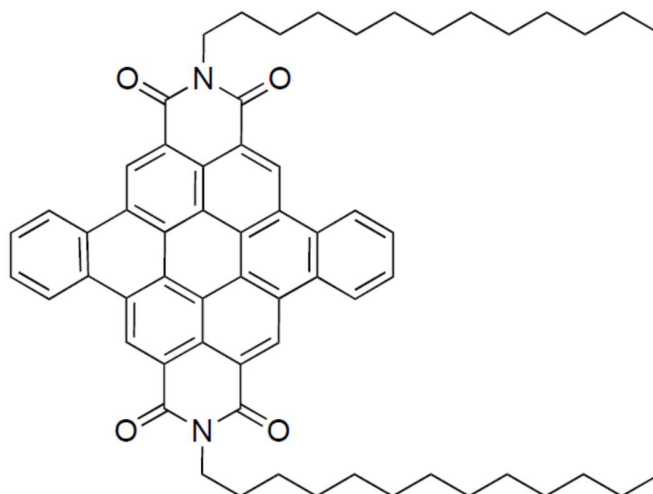
To synthesize DB-PTCDI-C13, a procedure described in literatures⁷⁹⁻⁸⁰ was modified. 1,7-dibromoperylene-3,4,9,10-tetracarboxylic dianhydride (2.015 g; 3.66 mmol) and 1-aminotridecane (6.030 g; 30.24 mmol) were added into 100 ml of propionic acid. The mixture was refluxed for 24 hours. 200 ml cold water was added in the reaction mixture to precipitate the product which was collected by suction filtration. The crude product was purified by column chromatography on silica gel (dichloromethane: hexane = 7:2). The red powder was obtained (35%). ¹H NMR (CDCl₃) δ (ppm): 0.86 (t, 6H), 1.35 (m, 40H), 1.74 (m, 4H), 4.19 (t, 4H), 8.69 (d, 2H, $J = 8.0$ Hz), 8.92 (s, 2H), 9.48 (d, 2H, $J = 8.0$ Hz) ¹³C NMR (CDCl₃) δ (ppm): 14.2, 29.4, 29.6, 29.7, 32.0, 40.9, 120.8, 122.8, 123.3, 127.0, 128.6, 129.3, 130.1, 132.9, 133.1, 138.1, 162.5, 163.0 Calc. for C₅₀H₆₀Br₂N₂O₄: C, 65.79; H, 6.63; N, 3.07. Found: C, 65.72; H, 6.61; N, 3.10%. MALDI-TOF MS: [M] 912.35; Crystal Data: Space group $P2_1/c$, $a = 22.969(4)$ Å, $b = 4.7258(7)$ Å, $c = 20.484(3)$ Å, $\beta = 97.771(4)^\circ$, C₅₀H₆₀Br₂N₂O₄, $Z = 2$, $R = 0.076$, G.O.F. = 1.094 CCDC 1833364

1,7-diphenyl-*N,N*-ditridecyl-perylene-3,4,9,10-tetracarboxylic diimide (DPH-PTCDI-C13)



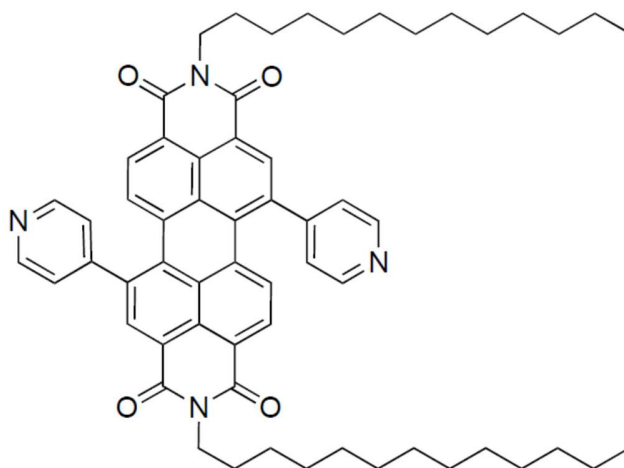
DB-PTCDI-C13 (1.033 g, 1.13 mmol), phenyl boronic acid (0.690 g, 5.66 mmol) and tetrabutylammonium bromide (0.365 g, 1.13 mmol) was stirred in 180 ml toluene and 26 ml aqueous 2 M K_2CO_3 under argon atmosphere. Then, tetrakis(triphenylphosphine) palladium(0) or $Pd(PPh_3)_4$ (0.196 g, 0.17 mmol) was added in the mixture. After that, the reaction was heated at 80 °C for 3 days. After addition of 500 ml CH_2Cl_2 , the reaction mixture was washed with 2 M HCl and water and dried with anhydrous Na_2SO_4 . The organic phase was evaporated to collect crude material which was then purified by column chromatography (hexane:ethyl acetate 10:1). The dark purple powder was obtained (75%). The synthesis procedure was modified from Yongjun Li⁸¹. 1H NMR ($CDCl_3$) δ (ppm): 0.91 (t, 6H), 1.35 (m, 40H), 1.74 (m, 4H), 4.19 (t, 4H), 7.50 (m, 6H), 7.52 (m, 4H), 7.82 (d, 2H, $J = 8.0$ Hz), 8.15 (d, 2H, $J = 8.0$ Hz), 8.63 (s, 2H) ^{13}C NMR ($CDCl_3$) δ (ppm): 14.2, 22.8, 29.4, 29.7, 32.0, 40.7, 121.9, 122.2, 127.5, 128.8, 129.1, 129.3, 130.3, 132.4, 134.7, 135.2, 141.0, 142.1, 163.3, 163.4 MALDI-TOF MS: [M cal.] 906.53 [M found] 906.57

***N,N'*-bis(*n*-tridecyl)-5,6:11,12-dibenzocoronene-2,3:8,9-bis(dicarboximide)**



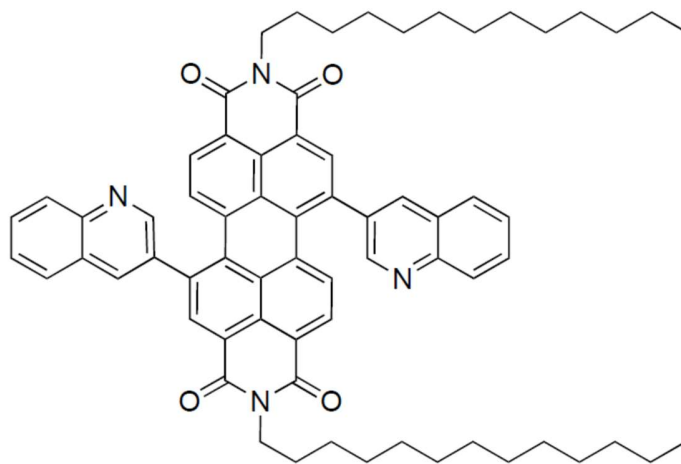
The synthetic method was the same with literature by Yongjun Li⁸¹. 500 mg DPH-PTCDI-C133 was dissolved in 1,250 ml methylene chloride and was irradiated under UV-light bulb lamp. The reaction propagation was followed by MALDI-TOF mass spectroscopy. Results will be discussed later in “results and discussion”.

1,7-dipyridyl-*N,N*-ditridecyl-perylene-3,4,9,10-tetracarboxylic diimide (DPY-PTCDI-C13)



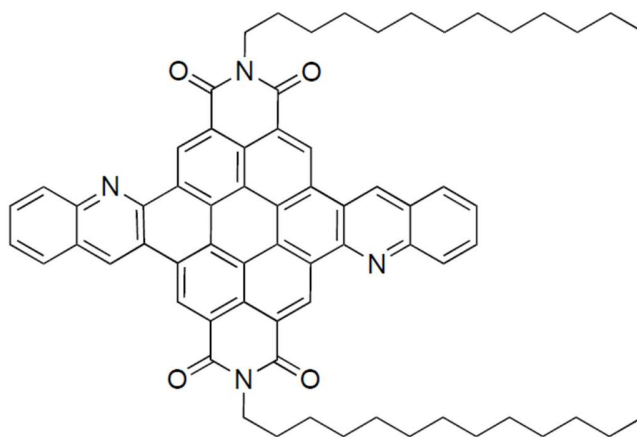
DB-PTCDI-C13 (1.010 g, 1.11 mmol), pyridyl-4-boronic acid (0.680 g, 5.53 mmol) and tetrabutylammonium bromide (0.357 g, 1.11 mmol) was stirred in 180 ml THF and 25 ml aqueous 2 M K_2CO_3 under argon atmosphere. Then, tetrakis(triphenylphosphine) palladium(0) or $Pd(PPh_3)_4$ (0.192 g, 0.16 mmol) was added into the solution. The reaction was heated at 80 °C for 3 days. After 500 ml CH_2Cl_2 was added, the mixture was washed with 2 M HCl, water and dried with anhydrous Na_2SO_4 . The organic phase was evaporated to collect crude material which was then purified by column chromatography (hexane : ethyl acetate = 6:4). The purified powder was obtained (49%). The synthesis procedure was modified from Wei Jiang⁸². 1H NMR ($CDCl_3$) δ (ppm): 0.91 (t, 6H), 1.35 (m, 40H), 1.74 (m, 4H), 4.17 (t, 4H), 7.50 (d, 4H, J = 8.0 Hz), 7.82 (d, 2H, J = 8.0 Hz), 8.23 (d, 2H, J = 8.0 Hz), 8.58 (s, 2H), 8.78 (d, 4H, J = 8.0 Hz) ^{13}C NMR ($CDCl_3$) δ (ppm): 14.2, 22.8, 27.2, 28.2, 29.4, 29.6, 29.7, 32.0, 40.8, 122.7, 122.9, 123.7, 128.0, 128.5, 128.9, 130.0, 131.0, 132.1, 132.2, 132.4, 133.7, 134.6, 138.2, 149.8, 151.8, 163.0 MALDI-TOF MS: [M cal.] 908.52 [M found] 908.58

1,7-diquinolidyl-*N,N*-ditridecyl-perylene-3,4,9,10-tetracarboxylic diimide (DQ-PTCDI-C13)



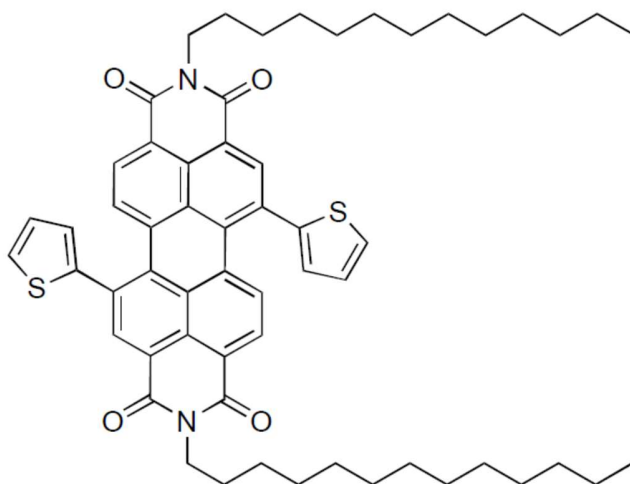
DB-PTCDI-C13 (1.008 g, 1.10 mmol), quinoline-4-boronic acid (0.955 g, 5.52 mmol) and tetrabutylammonium bromide (0.356 g, 1.10 mmol) was stirred in 180 ml THF and 25 ml aqueous 2 M K_2CO_3 under argon atmosphere. Tetrakis(triphenylphosphine) palladium(0) or $Pd(PPh_3)_4$ (0.192 g, 0.16 mmol) was added into the solution. After that, the reaction was heated at 80 °C for 3 days. To work up, 500 ml CH_2Cl_2 was added, washed with 2 M HCl, water and dried with anhydrous Na_2SO_4 . The organic phase was evaporated to collect crude material which was purified by column chromatography (hexane:ethyl acetate 3:1). The DQ-PTCDI-C13 powder was obtained in 55% yield. The synthesis procedure was modified from that by Wei Jiang⁸². MALDI-TOF MS: [M cal.] 1008.54 [M found] 1008.63

2,13-ditridecyldipyrido[3',4',5':3,4;3'',4'',5'':9,10]perylene[1,12-*abc*:7,6-*a'b'c'*]diacridine-1,3,12,14(2*H*,13*H*)-tetraone

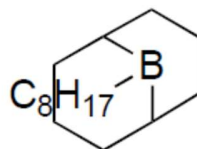


500 mg DQ-PTCDI-C13 was dissolved in 1,250 ml methylene chloride under light bulb lamp. The reaction propagation was followed by MALDI-TOF mass technique. Results will be discussed later in “results and discussion”. The preparation method was the same with that from Wei Jiang⁸².

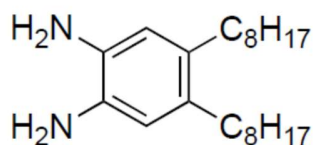
1,7-dithiophenyl-*N,N*-ditridecyl-perylene-3,4,9,10-tetracarboxylic diimide (DTP-PTCDI-C13)



DB-PTCDI-C13 (1.051 g, 1.15 mmol), 2-thiophene boronic acid (0.737 g, 5.76 mmol) and tetrabutylammonium bromide (0.371 g, 1.15 mmol) was stirred in 180 ml THF and 25 ml 2 M K_2CO_3 under argon atmosphere. Then, tetrakis(triphenylphosphine) palladium(0) or $Pd(PPh_3)_4$ (0.200 g, 0.17 mmol) was added in the mixture. After that, the reaction was heated at 80 °C for 3 days. To work up, 500 ml CH_2Cl_2 was added, washed with 2 M HCl, water and dried with anhydrous Na_2SO_4 . The organic phase was evaporated to collect crude material, whose result will be discussed later in “results and discussion”.

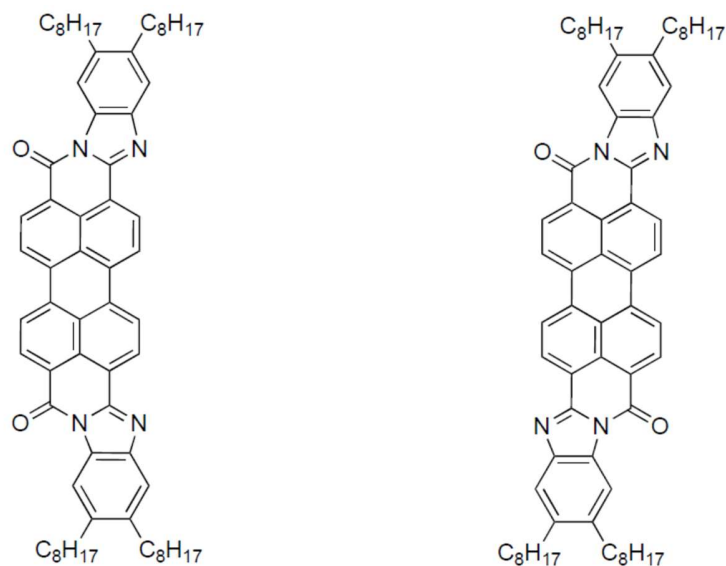
B-octyl-9-BBN

1-octene (1.403 g, 12.5 mmol) was added in 6 ml dried THF. At 0 °C, 25 ml 0.5 M 9-BBN in THF (1.525 g, 12.5 mmol) was added into the solution. Next, the reaction mixture was stirred at room temperature for 6 hours. The product was used in the next step without purification.

4,5-dioctyl-1,2-phenylenediamine

4,5-dibromo-1,2-phenylenediamine (1.556 g, 5.847 mmol), crude B-octyl-9-BBN and 10 ml 3 M NaOH was dissolved in 12 ml THF under argon atmosphere. Next, PdCl₂(dppf) (0.258 g, 0.351 mmol, 6 mol%) was added into the reaction mixture. The reaction was refluxed at 70 °C for 16 hours. After that, 40 ml hexane was added for dilution then 5 ml 30% H₂O₂, 50 ml brine. Dry over anhydrous MgSO₄. The crude was obtained after evaporation which was purified by column chromatography on silicagel (dichloromethane: ethyl acetate 4:1). The black oil was obtained (37%); LCMS [332].

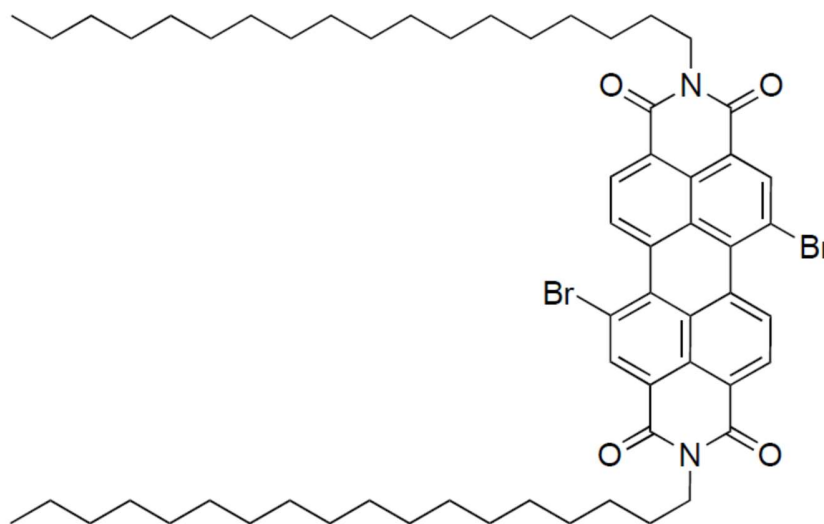
Perylene-3,4,9,10-tetracarboxylic bis(4,5-bis(octyl)-1,2-benzimidazole) (scheme 2.2.2.1)



Scheme 2.2.2.1 Structure of synthesized perylene benzimidazole derivatives

Perylene-3,4,9,10-tetracarboxylic dianhydride (0.982 g, 2.50 mmol), 4,5-dioctyl-1,2-phenylenediamine (4.978 g, 15.0 mmol) and zinc chloride (0.353 g, 2.59 mmol) were refluxed in 70 ml quinoline for 1 day. 100 ml cold water was added to precipitate the organics. The suction filtration was conducted to obtain residue which was washed with 1,000 ml hot ethanol. The residue was stirred in 1,500 ml hot alkaline solution (28 g NaOH and 28 g Na₂SO₄) for 30 minutes at 45°C. Lastly, residue was cleaned with 500 ml 3 M HCl then water until neutral. The residue was dried on water bath and kept as crude material (quantitative yield). MALDI-TOF MS [984.66]

1,7-dibromo-*N,N*-(dioctadecyl)-perylene-3,4,9,10-tetracarboxylic diimide (DB-PTCDI-C18)



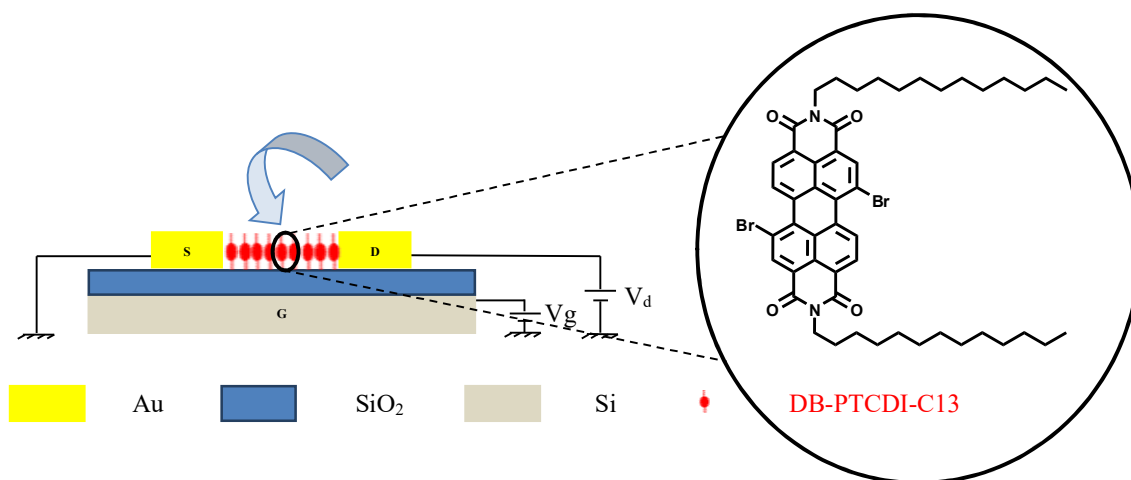
1,7-dibromo-perylene-3,4,9,10-tetracarboxylic dianhydride (0.501 g; 0.91 mmol) and *n*-octadecylamine (0.982 g, 3.64 mmol) were added in propionic acid 25 ml. The mixture was refluxed for 24 hours. 500 ml cold water was added in the reaction mixture to precipitate the product which was obtained by suction filtration. The crude product was purified by column chromatography on silicagel (dichloromethane: hexane 4:3). The red powder was obtained (9%).
 ^1H NMR (CDCl_3) δ (ppm): 0.86 (t, 6H), 1.35 (m, 60H), 1.74 (m, 4H), 4.19 (t, 4H), 8.69 (d, 2H, $J = 8.0$ Hz), 8.92 (s, 2H), 9.48 (d, 2H, $J = 8.0$ Hz)

2.2.3 Fabrication of monolayer

Fabrication method for DB-PTCDI-C13 monolayer

The author tested two solution-process methods for preparing monolayer. Molecules other than DB-PTCDI-C13 were not successful in monolayer formation due to the lack of solubility. For spin coating process, DB-PTCDI-C13 (1 mg) was dissolved in 1 ml toluene containing 1% of THF. After sonication, the solution was spin coated on SiO₂/Si substrate with patterned gold electrode with the rate of 1500 r.p.m. Next, coated substrate was heated for annealing under argon atmosphere. All spin coated device was prepared via this manner. (**Scheme 2.2.3.1**)

Drop cast film was prepared by similar manner. After sonication, the solution was dropped and dried at room temperature on SiO₂/Si substrate with patterned gold electrode. The annealing process was conducted under argon atmosphere.



Scheme 2.2.3.1. Conceptual device scheme for monolayer FET preparation based on DB-PTCDI-C13

2.2.4 Performance evaluation

The mobility (μ) was obtained from drain current (I_d) and gate voltage (V_g) plots. First, the normalized conductivity (σ) can be calculated by drain current, electrode gap length (L) and width of the electrode (W) using this equation:

$$\sigma = I_d * \frac{L}{W} \quad (\text{eq. 1})$$

After plot of conductivity dependence on the gate voltage, the mobility in linear regime is given by,

$$\mu = \frac{d}{\varepsilon_0 \varepsilon'} * \frac{d\sigma}{dV_g} \quad (\text{eq. 2})$$

The mobility can be also calculated in saturation regime, if the I_d - V_d plot shows saturation regime. The mobility is given by,

$$\mu = \frac{d}{\varepsilon_0 \varepsilon'} * 2 * \frac{L}{W} * \left(\frac{dI_d^{1/2}}{dV_g} \right)^2 \quad (\text{eq. 3})$$

where d is the thickness of SiO₂ insulating layer (300 nm), ε_0 is vacuum permittivity of electric constant (8.85×10^{-12} F/m) and ε is relative permittivity of SiO₂ (3.9).

2.2.5 Quantum chemical calculation

Structural optimization and vibrational analysis as well as band structure analysis were performed using computational methods based on density functional theory (DFT)⁸³. Here, Plane wave-based periodic DFT calculations were performed using Vienna Ab-initio Simulation Package (VASP) version 5.4.1⁸⁴. Projector-augmented wave method (PAW) were used to describe electrons close to the ionic core. Electron exchange and correlation functional was based on generalized gradient approximation (GGA) of Perdew, Burke, and Ernzenhof (PBE)⁸⁵. Brillouin zone integration was performed using a $1 \times 4 \times 1$ Γ -centered grid for k -point sampling with the cutoff energy of 450 eV and Gaussian smearing energy of 0.1 eV. Electronic relaxation was carried out using electronic self-consistent field (SCF) iteration criterion of 10^{-6} eV with non-spin polarized calculations based on Davidson block iteration scheme. Structural optimization was obtained using conjugated gradient method until the maximum force acting on each atom was smaller than 0.01 eV/Å. Vibrational analysis was performed using finite difference method with displacement size of 0.01 Å. In all calculations, all atoms were allowed to relax while the cell parameters were kept constant. Dispersion interaction was also included in the energy and force calculation using DFT-D3 method of Grimme⁸⁶. For bandgap and density of states (DOS) calculation, a single-point hybrid functional of HSE06⁸⁷ was used.

2.3 Results and discussion

2.3.1 Benzimidazole derivative

2.3.1.1. Purification and characterization of perylenebis-benzimidazole regioisomers

The author attempted to dissolve the synthesized crude perylenebis-benzimidazole (**Figure 2.3.1.1.1**). Unfortunately, this mixture was highly insoluble in toluene or methylene chloride. MALDI-TOF mass of crude perylenebis-benzimidazole is shown in **Figure S. 2.3.1.1.2**. The result exhibited that the author has successfully synthesized the target compound, however, the purification could not be conducted by column chromatography with silica gel or alumina gel due to poor solubility. As a result, synthesized perylenebis-benzimidazole cannot be used as n-type semiconductor for OFET application via solution-deposition process.

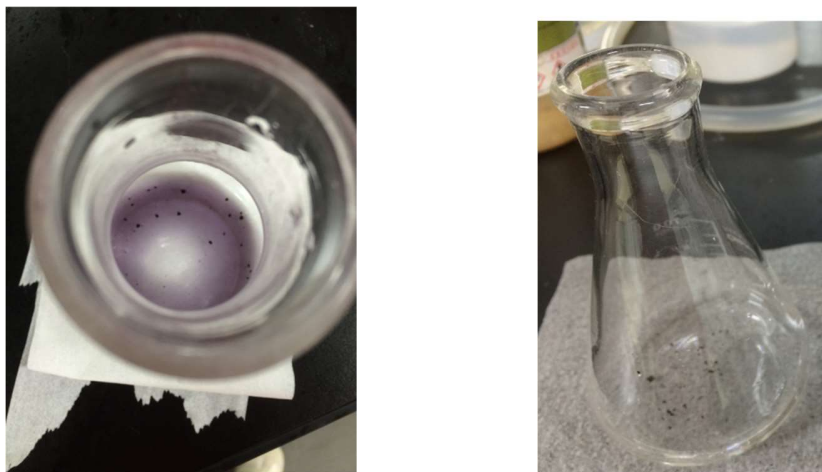


Figure 2.3.1.1.1 Solubility of synthesized perylene-benzimidazole regioisomers in methylenechloride (left) toluene (right)

2.3.2 Coronene derivatives

2.3.2.1. Purification and characterization of coronene derivatives

The synthesis of coronene derivatives is described in experimental part. Briefly speaking, diphenyl derivative (DPH-*N,N*-ditridecyl-perylene-3,4,9,10-tetracarboxylic diimide) was dissolved in methylene chloride and was irradiated with UV lamp. After that, the reaction mixture was checked from time to time by MALDI-TOF mass. From the results, we found that all synthesized products are labile. The molecular mass peak was decreased after light exposure, although the driving force of the reaction is also the light. The situation was the same with diquionolidyl (DQ) and dipyrindyl (DPY) derivatives. For instance, the 549.89 m/z peak, which was degradation peak of target, was increased after light exposure of DQ-PTCDI-C13 whose molecular mass peak is 1006.54 m/z (Figure 2.3.2.1.1.)

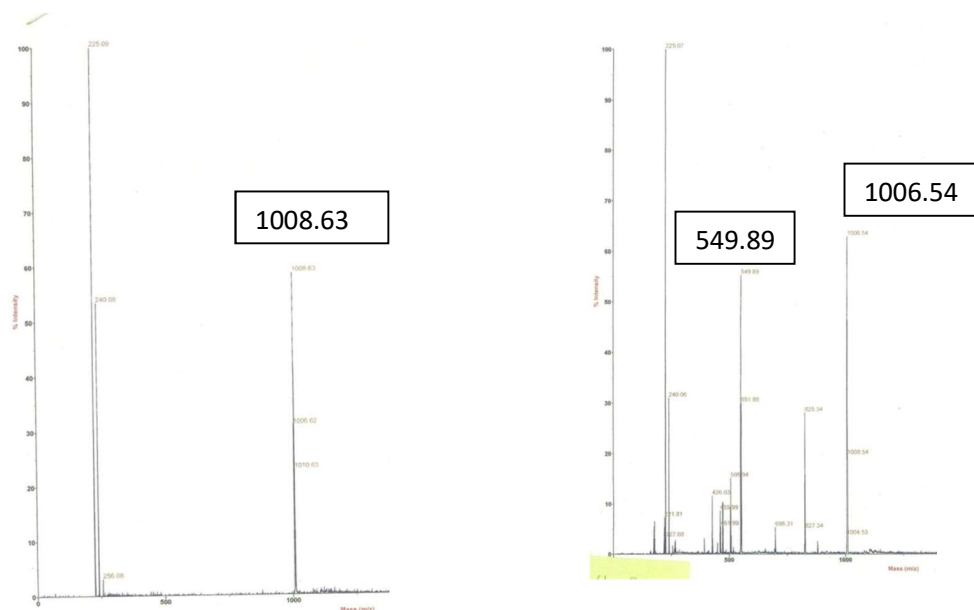


Figure 2.3.2.1.1 MALDI-TOF mass spectrum of DQ-PTCDI-C13 before light exposure (left; starting material) and after light exposure for 6 hours (right)

Not only DQ-PTCDI-C13, but also DPY-PTCDI-C13 and DP-PTCDI-C13 were decomposed after light exposure (**Figure S. 2.3.2.1.1 – 2.3.2.1.6**). (In case of DTP-PTCDI-C13 ((1,7-dithiophenyl)-*N,N*-ditridecyl-perylene-3,4,9,10-tetracarboxylic diimide), Suzuki coupling step was not successful (**Figure S. 2.3.2.1.7**.) Unfortunately, there are 2 main obstacles to purify coronene derivatives. First, the coronene products are highly sensitive to light exposure. Even under ambient light, the molecular mass peak was decomposed into the lower mass peaks. In addition, during light exposure, starting material was remaining with decomposed peak. In other words, light exposure was not only activator for our target but is also a decomposing force at the same time. Another major reason is that they were poorly soluble in common organic solvent such as methylene chloride. Although toluene was recommended in literatures to be used as solvent for crystallization, our coronene derivatives were very poor in solubility. Hence, it is hard to purify by column chromatography and to crystallize them even in a closed dark box to prepare OFET devices by solution deposition process.

2.3.3 DB-PTCDI-C13

2.3.3.1. Purification and characterization of DB-PTCDI-C13

Since the final purpose of this research is to form a thin layer Mott FET, flat and thin uniform film is necessary for alkaline metal doping in succeeding experiments. Unlike non-substituted PTCDI-C13 that can be solubilized only in a strong solvent such as chlorobenzene, DB-PTCDI-C13 was able to be dissolved in common organic solvent such as methylene chloride and toluene. From the X-ray diffraction analysis (XRD), DB-PTCDI-C13 in single crystal exhibited one-dimensional π - π stacking whose inclination angle alternates among the neighboring columns as shown in **Figure 2.3.3.1.1** Each unit cell contains 2 molecules that form a two-dimensional conduction layer. Although this layer structure in crystal might not be preserved in thin layer form, some clues on thin film structure can be obtained from this crystal structure. Bromine atoms show two non-equivalent positions which can be optimized as a disorder in 7:3 ratio. In the major structure, the molecular π -core seems to be twisted to avoid steric repulsion between H and Br atoms, although the atomic position of all the carbon atoms stay in the same plane. In comparison to PTCDI-C13, this twisting effect seems to make the solubility better for DB-PTCDI-C13. According to a quantum chemical calculation, indeed, the most stable conformation of this molecule is a twisted shape as shown in **Figure 2.3.3.1.2**. This kind of corrugated molecular shape is good for suppressing the one-dimensionality: the same strategy has been used for the development of BEDT-TTF where bulky terminal ethylene group is preventing strong π - π interaction to form two-dimensional conductors. Normally, van der Waals contact between H atom and Br atom is 3.05 Å. For DB-PTCDI-C13, our DFT calculation found that H-

Br distance was 2.35 Å which is much shorter than the van der Waals contact. Hence, repulsion can cause twist of the π -core which is in a good agreement with X-ray analysis. The molecular vibration modes were also calculated, and strong out-of-plane vibration of Br atom was obtained at 21.8, 24.2 and 27.1 cm^{-1} . In addition, the rotational modes of the aromatic core causing similar movement of the Br atom were also found at 191.7 and 193.5 cm^{-1} . These relatively low wavenumber on Br-focused vibrational modes indicate that Br atoms tend to vibrate easily. Because the flat planer structure of the Br and π -core observed in X-ray analysis as a minor configuration is energetically unfavorable due to the strong repulsion, these vibrational modes seem to make the molecule look like in a 7:3 disordered structure.

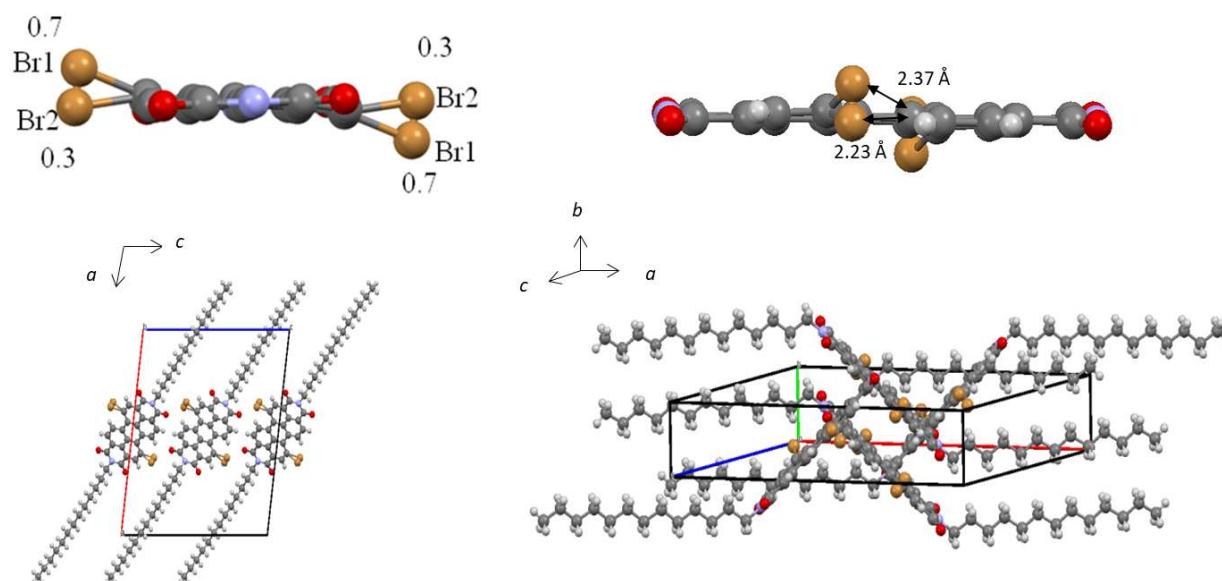


Figure 2.3.3.1.1. X-ray crystallographic data of (a) DB-PTCDI-C13 viewed along the long axis (left) and along the short axis (right) of the π -core, and (b) packing of DB-PTCDI-C13 in unit cell. The alkyl chains are omitted for clarity in (a).

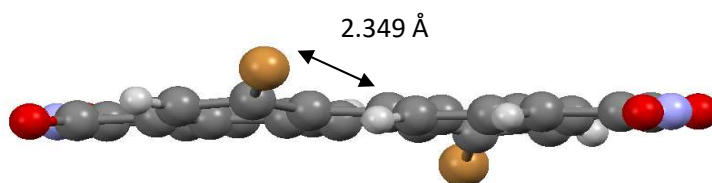


Figure 2.3.3.1.2. Calculated molecular structure in a crystal of DB-PTCDI-C13, viewed along the short axis of the π -core. (alkyl chains are omitted for clarity.)

Density of states (DOS) of DB-PTCDI-C13 was obtained using hybrid DFT calculation, whose results are shown in **Figure 2.3.3.1.3**. Total DOS result shows that calculated bandgap of DB-PTCDI-C13 is 1.63 eV. In addition, Partial DOS results suggest that Br, C, and O atoms occupy both highest occupied molecular orbital (HOMO) and lowest occupied molecular orbital (LUMO), while N orbital is neither involved in HOMO nor LUMO states. In addition, the aligned partial DOS peaks of Br, C, and O orbitals at HOMO and LUMO states (see arrows in **Figure 2.3.3.1.3**) indicate the coupling role of these three species in terms of conductivity for DB-PTCDI-C13.

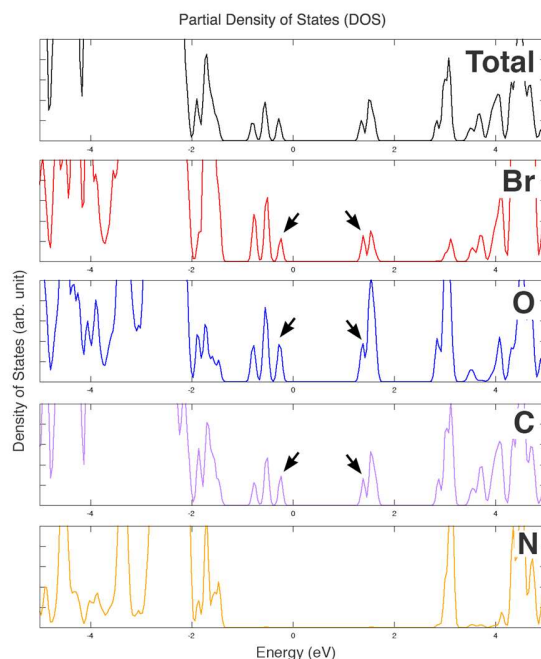


Figure 2.3.3.1.3. Total density of states (DOS) DB-PTCDI-C13 and Partial Density of States for Br, O, C, and N atomic orbitals.

Thermal characterization of DB-PTCDI-C13 was performed by DSC to investigate the relationship between annealing temperature and mesomorphic phases. The thermogram in **Figure 2.3.3.1.4** shows heating and cooling calorimetry. In the heating mode (bottom) the compound exhibited two consecutive endothermic peaks around 148°C and it completely melted at 188°C. The peak at 148°C seems to be related to liquid crystalline formation due to the long flexible hydrocarbon chain of tridecyl moieties⁸⁸. X-ray diffraction also showed smectic-like diffuse patterns in this temperature range. In the cooling mode (top), two exothermic peaks at 188°C and 169°C were observed. From this experiment, no peak below 148°C was observed. In this regard, 169°C seems not to be a crystallization point but is the temperature where liquid crystal mesophase transition (smectic A to smectic C, for example) takes place. After the temperature history, molecular packing will be reorganized from polycrystalline to highly ordered liquid crystal. These

results are consistent with DFM measurement that will be discussed later, where highly ordered film was obtained after annealing. It is suggested in literatures⁸⁹ that heating to melting point or nematic phase could cause low molecular order to result in poor mobility. Therefore, appropriate annealing temperature seems to be around 160°C, at which we optimized the film quality and mobility in the next section.

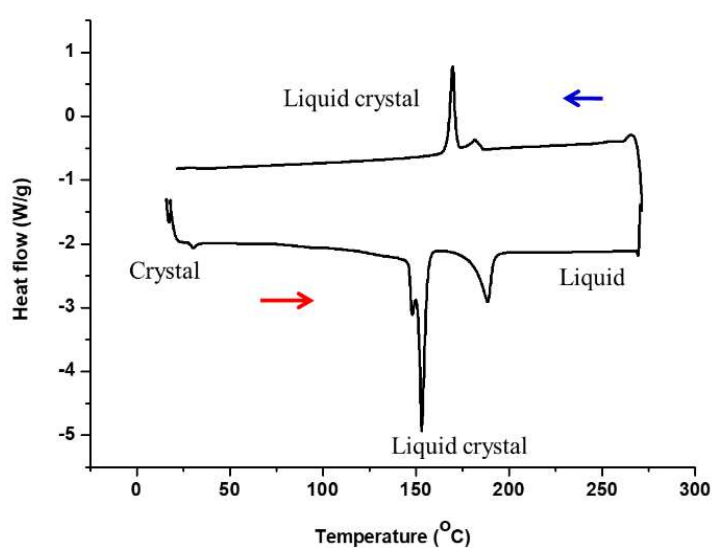


Figure 2.3.3.1.4. DSC heating and cooling curves of DB-PTCDI-C13 with scan rate 10 °C/min.

2.3.3.2. Film process of DB-PTCDI-C13 film

2.3.3.2.1 Evaporation of DB-PTCDI-C13

To compare our synthesized compound (DB-PTCDI-C13) with non-brominated compound, PTCDI-C13 was dissolved in toluene and methylene chloride. Unfortunately, PTCDI-C13 was poorly soluble in common organic solvent. In the other words, thin film PTCDI-C13 was not able to be prepared by solution deposition process. Generally, preparation of PTCDI-C13 film is achieved by evaporation method. The FET property of evaporated PTCDI-C13 film was n-type as same as DB-PTCDI-C13. The reported mobility was $2.1 \text{ cm}^2 \text{ V}^{-1} \text{ s}^{-1}$ after annealing at 140°C for 1 hour³⁵. In the opposite way, DB-PTCDI-C13 was not suitable for evaporation method. After evaporation of DB-PTCDI-C13, MALDI-TOF mass was measured (**Figure 2.3.3.2.1.1**). The results showed that bromine atoms were lost in the film. Unlike annealed PTCDI-C13, evaporated DB-PTCDI-C13 films showed low mobility. The evaporated DB-PTCDI-C13 might be changed into amorphous PTCDI-C13 film with many defects.

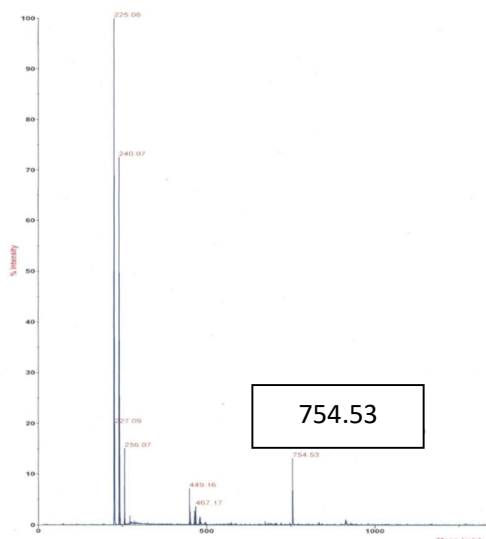


Figure 2.3.3.2.1.1 MALDI-TOF mass spectrum of DB-PTCDI-C13 after evaporation. The mass peak at m/z 754.5 corresponds to PTCDI-C13 (without bromine).

2.3.3.2.2 Drop casted DB-PTCDI-C13

2.3.3.2.2.1 Optical microscope images of device with and without annealing

Because of the better solubility originated from the molecular shape, DB-PTCDI-C13 (m/z 912.31) in **Figure S. 2.3.3.1.3** dissolved in pure toluene was tried for spin coating and drop casting for film formation. However, it did not give a uniform film, and systematic solvent survey was conducted to avoid 3-dimensional crystal growth⁹⁰. At the end, DB-PTCDI-C13 solution with toluene containing 1% THF was used for spin coating and drop casting to result in monolayer or few layers uniform film. It should be noted that evaporation of DB-PTCDI-C13 in vacuum only resulted in a deposition of non-substituted PTCID-C13 film (m/z 754.53), which was confirmed by MALDI mass spectroscopy in **Figure 2.3.3.2.2.1.1** (The molecule seems to decompose at high temperature). Therefore, solution process coupled with annealing is the best method for film growth of this material.

Drop cast method was examined. Optical microscope image was captured for these devices before and after annealing which are shown in **Figure 2.3.3.2.2.1.1-2**. In the optical microscope image, the amorphous film was transformed into poly-domain film when the annealing temperature was increasing as revealed by **Figure 2.3.3.2.2.1.3**



Figure 2.3.3.2.2.1.1 Optical microscope image of drop casting device before annealing (cross-Nicols)

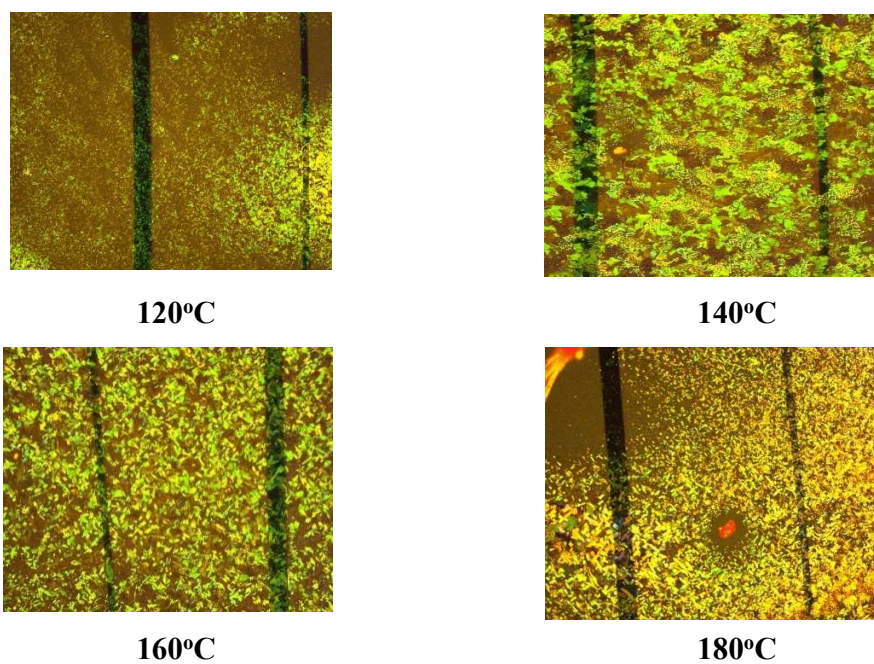
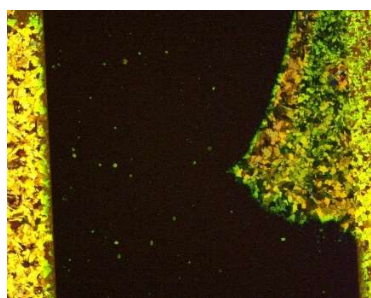


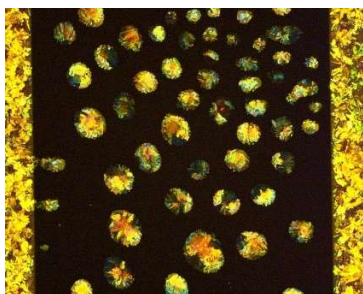
Figure 2.3.3.2.2.1.2 Optical microscope images around 5-10 μm electrode gap of annealed drop casting devices (cross-Nicols)



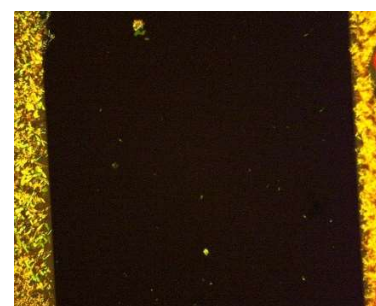
120°C



140°C



160°C



180°C

Figure 2.3.3.2.2.1.3 Optical microscope images at 200 μm gap of annealed drop casting devices (cross-Nicols)

Unfortunately, the film was broken apart and grown to three-dimensional islands when the annealing was conducted with drop casted film. Basically, perylene derivatives films grow in Stranski-Krastanov mode⁹¹⁻⁹² in which heat diffusion breaks metastable layer under annealing condition. Thus, thick three-dimension islands were obtained to preclude further measurements for conductivity in a drop casted film.

2.3.3.2.2.2 Electrical characterization of annealing device

20 μL DB-PTCDI-C13 solution was dropped on substrate with patterned gold electrode SiO_2/Si . After annealing, the electron mobility was measured under vacuum. The electron mobility is exhibited in **Figure 2.3.3.2.2.1** The highest electron mobility obtained was the data from 1 hour sample. The increasing annealing time to 12 hours quenched the electron mobility.

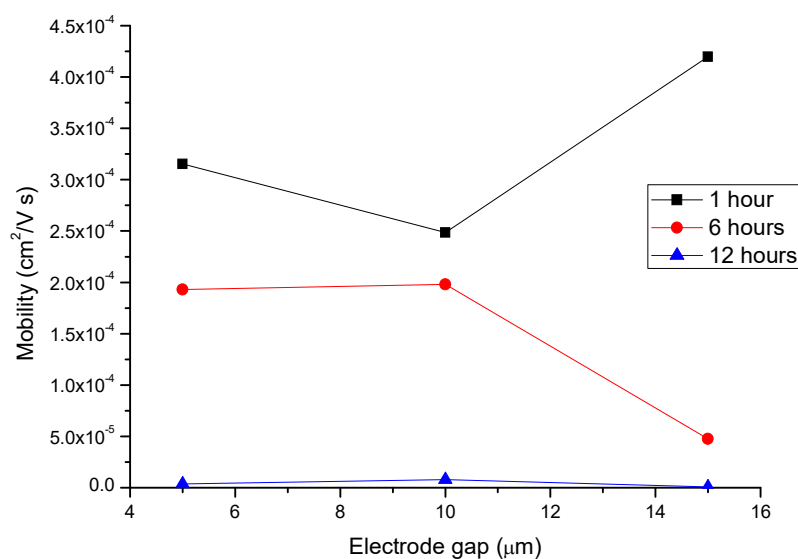


Figure 2.3.3.2.2.1 Electron mobility from drop casting method with variety annealing time

2.3.3.2.2.3 Optical microscope images and electrical characterization on SAM substrate

The drop-cast films were made on SAM-modified substrates. The optical microscope images of drop casting samples are shown in **Figure 2.3.3.2.2.3.1** The FET measurement result is displayed in **Table 2.3.3.2.2.3.1**. In conclusion, the SAM improved the mobility of the drop casting film, from no-FET property (without SAM sample) to poorly active FET. However, monolayer with better mobility was not obtained with this combination.

Table 2.3.3.2.2.3.1 The mobility of DB-PTCDI-C13 drop casting samples on SAM substrate

Sample	E2	F2	E4	F4	average
Mobility ($\times 10^{-4} \text{ cm}^2/\text{V s}$)	1.82	8.41	5.57	0.08	3.97

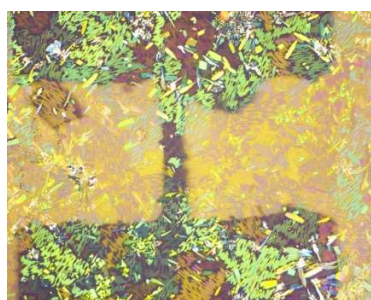
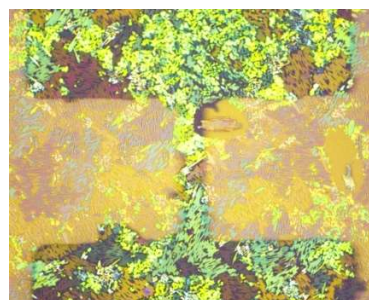
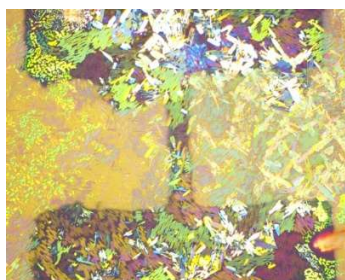
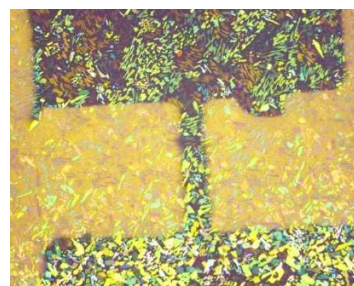
**E 2****F 2****E 3****F 3**

Figure 2.3.3.2.2.3.1 The optical microscope images of annealing drop casting samples after conductivity measurement

2.3.3.2.3 Spin coated DB-PTCDI-C13

2.3.3.2.3.1 Optical microscope and DFM images of samples with and without annealing

DB-PTCDI-C13 solution was spin coated on substrate with patterned gold electrode SiO_2/Si for 3 times. To ensure the annealing effect, the optical microscope image was checked after annealing. The images are shown in **Figure 2.3.3.2.3.1.1-2** The annealing temperature was 120, 140, 160 and 180°C.

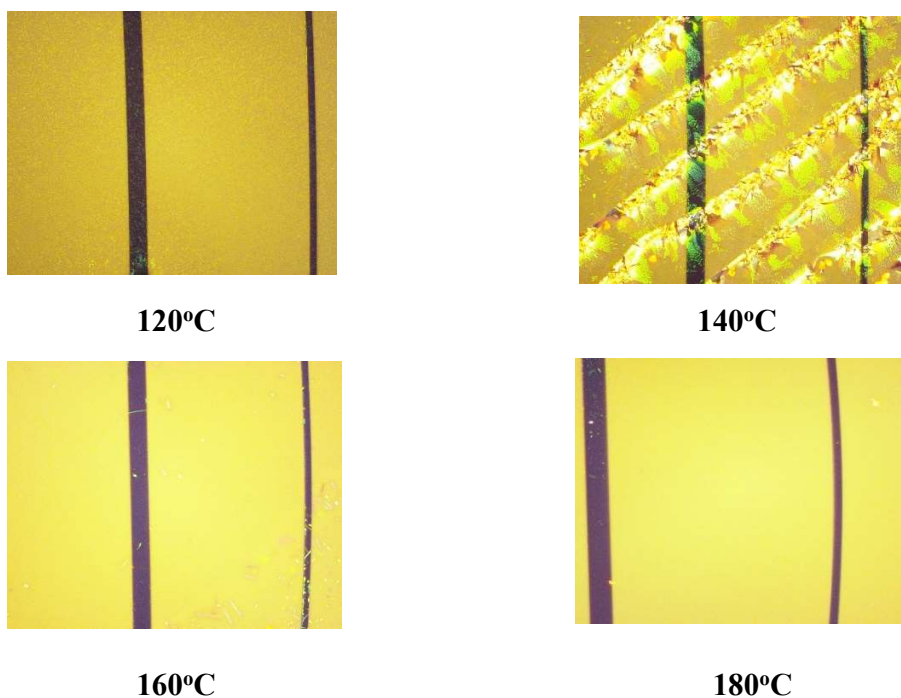


Figure 2.3.3.2.3.1.1 Optical microscope images around 5-10 μm gap electrodes of annealed spin coating devices (cross Nicols)



Figure 2.3.3.2.3.1.2 Optical microscope image of spin coating device before annealing. (cross Nikols)

At first, the optical image was captured at the center of the substrate but there was nothing in the image. At the edge of the substrate, on the other hand, spin coated film showed an image that implied amorphous orientation as **Figure 2.3.3.2.3.1.3left**. After annealing at 160°C for 1 hour, the poly domain layer was obtained as **Figure 2.3.3.2.3.1.3right**. In other words, the molecular arrangement was ordered after annealing.

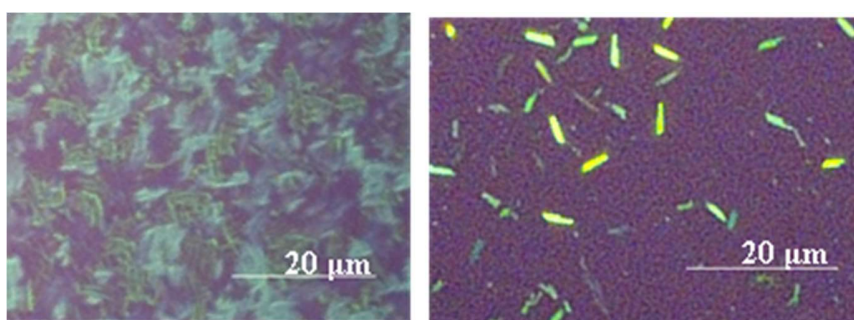


Figure 2.3.3.2.3.1.3. Zoom optical microscope image of (left) spin coated film before annealing (right) spin coated film after annealing at 160°C for 1 hour of DB-PTCDI-C13 film with polarizers in crossed Nicols configuration.

The DFM morphology characterization of spin coated film is also displayed in **Figure 2.3.3.2.3.1.4**. This is performed at the center of the substrate before and after the annealing. Usually, the thickness of spin coated monolayer of DB-PTCDI-C13 is 2 nm in DFM image that corresponds to a molecular longitudinal length. The result found that steps on the film were changed from the round protrusions to well-defined molecular steps by annealing at 160°C for 1 hour (see **Figure 2.3.3.2.3.1.4b**). It means that rough surface in deposited film, a result from amorphous-like crystallization during solvent evaporation, was ameliorated by annealing. Hence, annealing process can improve molecular ordering as displayed in images at the center of the substrate.

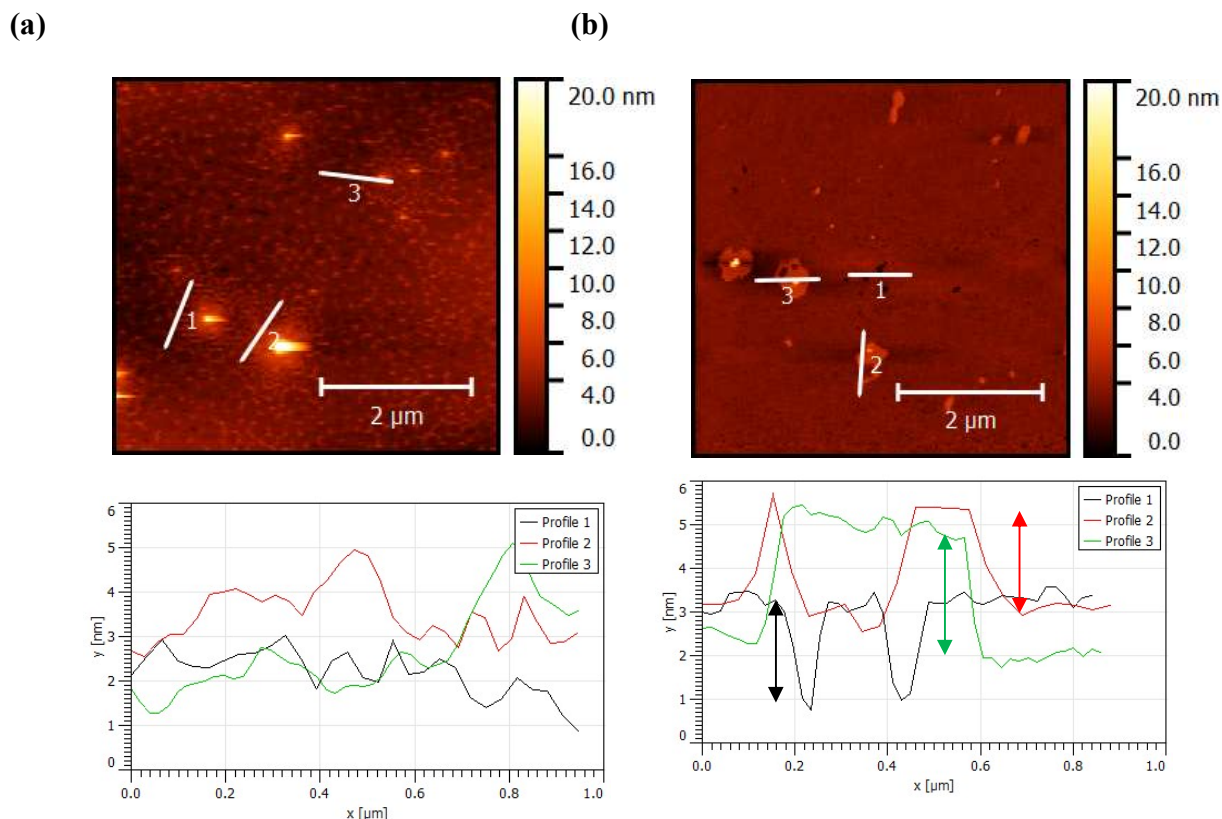
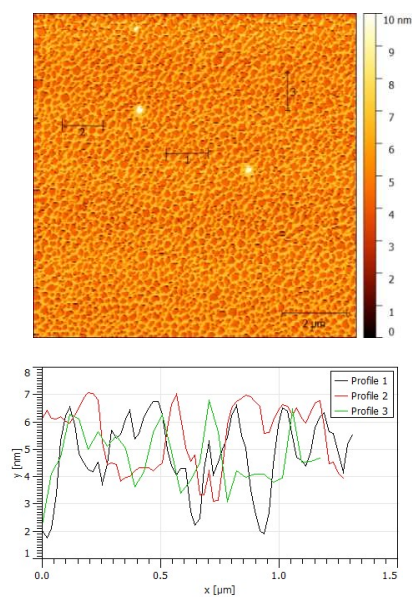


Figure 2.3.3.2.3.1.4. DFM images of (a) before annealing (b) after annealing of spin coated DB-PTCDI-C13 at 160°C for 1 hour (black arrow 2.0 nm, red arrow 2.5 nm, green arrow 3.0 nm)

In summary, the author prepared monolayer of DB-PTCDI-C13 by spin-coating 1000 ppm solution of DB-PTCDI-C13. In fact, this relates to our preliminary results with spin-coating of 500 ppm solution of DB-PTCDI-C13 whose results are added below. We found that it formed loose network with 2 nm thickness in DFM image as shown below. In other words, we found clear height difference between the substrate and the first DB-PTCDI-C13 layer (monolayer DB-PTCDI-C13) whose height was 2 nm (**Figure 2.3.3.2.3.1.5**). After that, we changed concentration of DB-PTCDI-C13 to 1000 ppm. We discovered the network was fulfilled to result in a dense flat film as DFM image in **Figure 2.3.3.2.3.1.4b**. Therefore, we claimed that 1000 ppm spin coated film was monolayer.

(a)



(b)

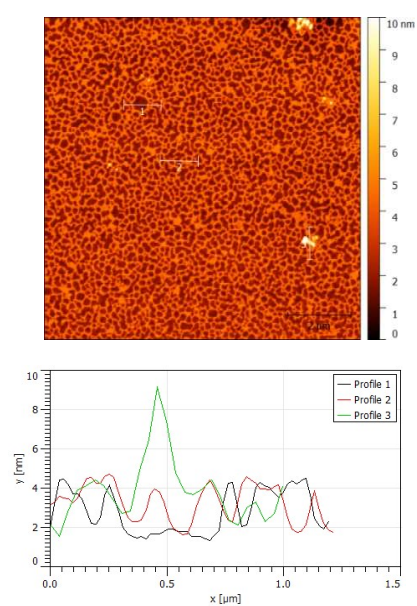


Figure 2.3.3.2.3.1.5 DFM images of (a) before annealing (b) after annealing at 60°C for 30 minutes of spin coated DB-PTCDI-C13 at 500 ppm in toluene

2.3.3.2.3.2 Electrical characterization of annealed device

The FET performance of DB-PTCDI-C13 film on SiO₂ (300 nm)/Si substrate was measured in a vacuum chamber. The $I_d - V_d$ characteristic of typical DB-PTCDI-C13 film is shown in **Figure 2.3.3.2.3.2.1left**. Judging from the fact that positive V_g enhances I_d , n-type FET behavior was confirmed. The non-ohmic behavior at low V_d region suggested high injection barrier at contact. The on/off ratio at maximum was 10^4 . From linear regime the mobility was $4.6 \times 10^{-4} \text{ cm}^2 \text{ V}^{-1} \text{ s}^{-1}$ at 20 V drain voltage. The mobility was calculated at $5.8 \times 10^{-3} \text{ cm}^2 \text{ V}^{-1} \text{ s}^{-1}$ (averaged value for three samples) from saturation regime after annealing at 160°C for 1 hour as **Figure 2.3.3.2.3.2.1right**. We have tested annealing temperature other than 160°C (120 – 180°C), but the measurement results were very poor and even a saturation regime could not be obtained. Nonetheless, conductance was totally diminished after 12 hours annealing at any annealing temperature. Three-dimensional crystalline state might be obtained for long time annealing. The $I_d^{1/2} - V_g$ characteristic of typical DB-PTCDI-C13 film is shown in **Figure 2.3.3.2.3.2.1right**. The threshold voltage (V_{th}) is estimated at high value, 75 V, which seems to be originating from high trap density. Such a high density trap may also be one of the causes of high injection barrier observed in the $I_d - V_d$ characteristics. The smaller linear regime mobility compared to that of saturation regime can be also understood by the influence of injection barrier.

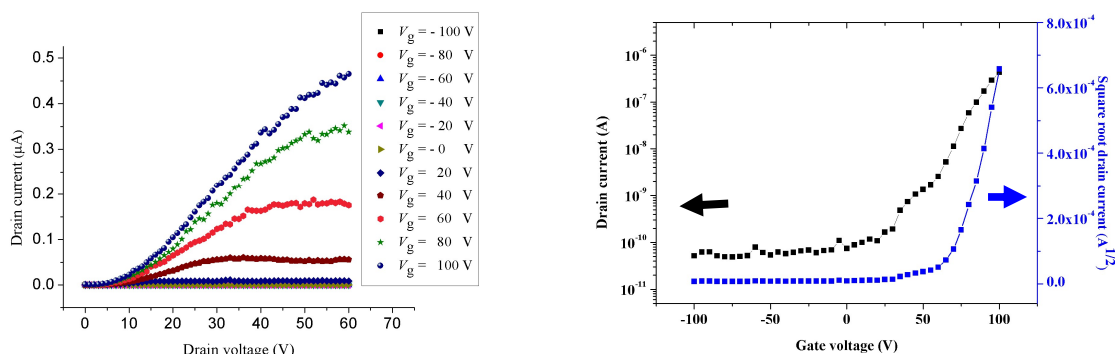


Figure 2.3.3.2.3.2.1. Electrical characterization (left) I_d - V_d characteristic, (right) I_d - V_g and $I_d^{1/2}$ - V_g characteristic at $V_d = 60$ V of spin-coating sample annealed at 160°C for 1 hour.

The mobility values are summarized in **Table 2.3.3.2.3.2.1**. The results concluded that FET mobility was significantly improved by structural ordering of DB-PTCDI-C13 during annealing. The highest electron mobility was obtained from 160°C annealed device. However, the increasing or decreasing annealing temperature from 160°C suppressed the electron mobility. Above 160°C, DB-PTCDI-C13 could be melted to liquid phase. From previous reports on similar materials⁸⁹, heating to melting point could cause low molecular order which resulted in poor mobility. Below 160°C, on the other hand, low molecular order in the films was probably retained. For instance, Marchetto and co-workers found that annealing at low temperature can cause growth of multilayer film by mean of so-called Franck-van der Merwe behavior⁹¹. It is also in good agreement with a report on PTCDI-C13 in which well-aligned crystalline films were obtained at their mesomorphic temperature⁸⁹. In conclusion, the high FET efficiencies were obtained in the well-aligned film which has been characterized by DFM image in **Figure 2.3.3.2.3.2.4**. Furthermore, we found that the mobility values were increased with the increase of electrode gap where the contact resistance

due to the injection barrier was dominating the transport at shorter gap devices. The relationship between electrode gap and mobility was summarized in **Figure 2.3.3.2.3.2.2.**

Nonetheless, mobility was totally diminished after 12 hours annealing. Low molecular order might be obtained for long time annealing. The electron mobility was summarized in **Figure 2.3.3.2.3.2.3.** The highest electron mobility was obtained from 160°C annealing device for 1 hour.

Table 2.3.3.2.3.2.1. Summary of mobility values for spin coated DB-PTCDI-C13

Annealing temperature (°C)	Mobility ($\times 10^{-4} \text{ cm}^2/\text{V s}$)			
	10 μm gap		100 μm gap	
	Linear	Saturation	Linear	Saturation
	regime	regime	regime	regime
120	1.45 (1.43)	NA	NA	NA
140	2.69 (3.56)	NA	NA	NA
160	4.55 (2.36)	6.29 (4.85)	26.4 (11.1)	58.6 (43.8)
180	1.71 (1.46)	NA	NA	NA

NA stands for Not Available. The values in parentheses are standard deviations.

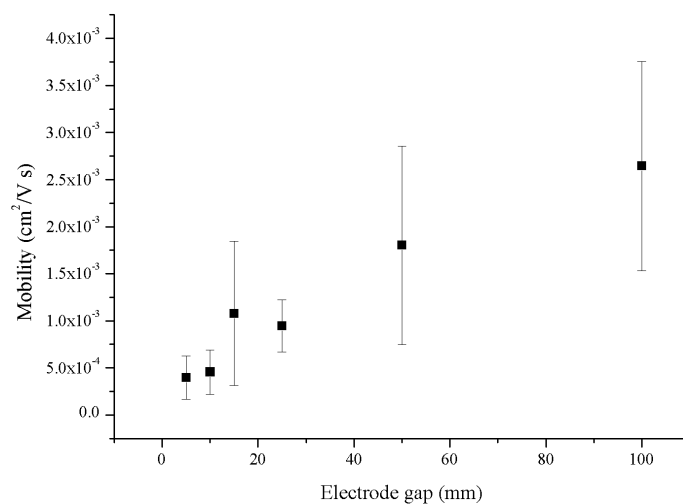


Figure 2.3.3.2.3.2.2. Mobility values of spin coated DB-PTCDI-C13 film as a function of electrode gap

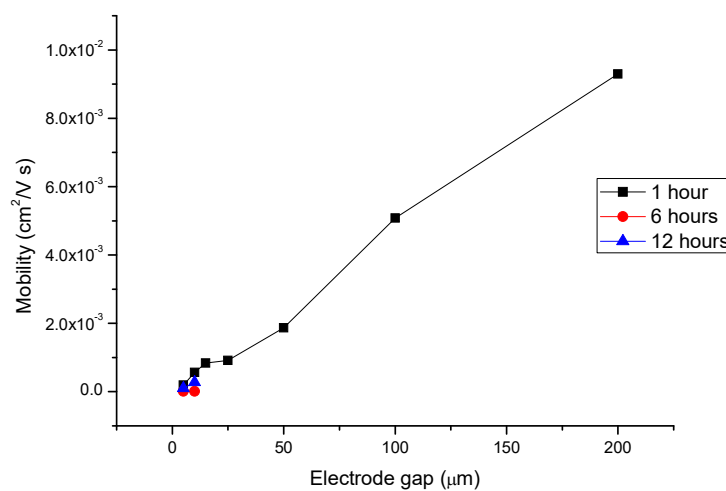


Figure 2.3.3.2.3.2.3. Electron mobility from spin coating method 5-200 μm with variety annealing time

2.3.3.2.3.3 Electrical characterization with SAM substrate

DB-PTCDI-C13 solution was spin coated on SAM modified SiO₂/Si for 3 times. The result displayed that mobility was increased by SAM (Self-assembled monolayer). As a result, the mobility of sample without annealing became similar to those with 160°C annealing for 1 hour (Figure 2.3.3.2.3.3.1).

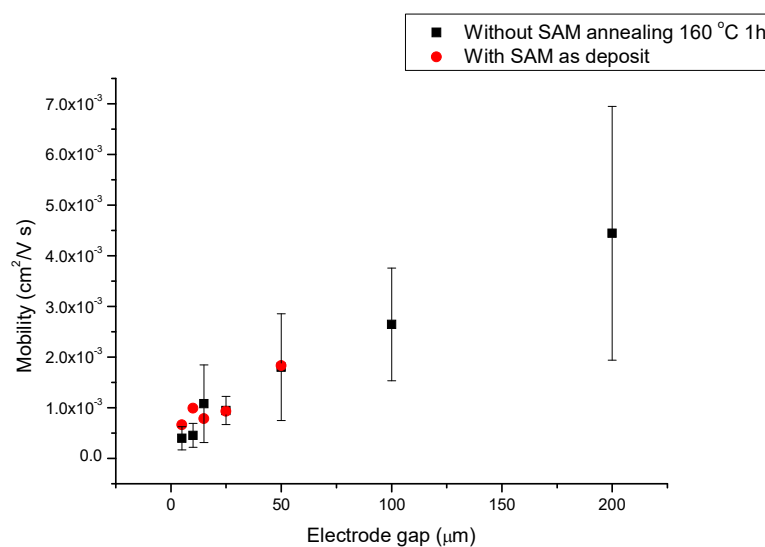


Figure 2.3.3.2.3.3.1 Mobility with and without SAM of spin coating sample

2.3.4 DB-PTCDI-C18

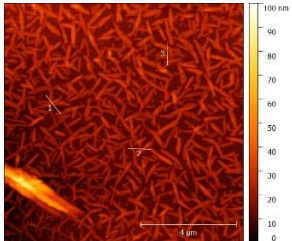
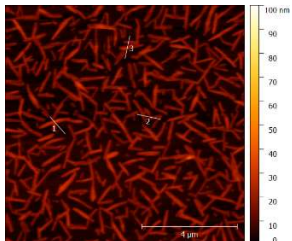
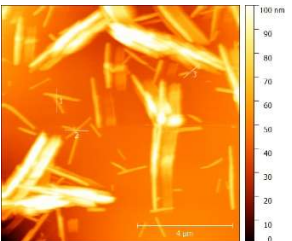
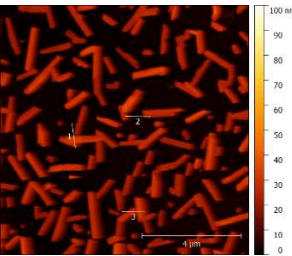
2.3.4.1. Purification, characterization of DB-PTCDI-C18

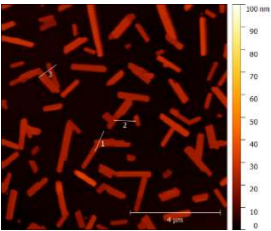
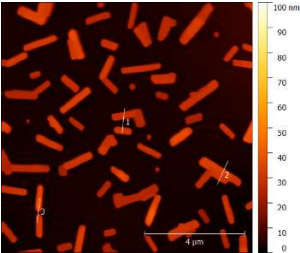
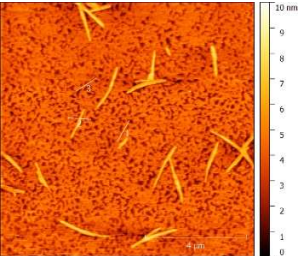
Synthesis of DB-PTCDI-C18 was similar to DB-PTCDI-C13 procedure. However, the yield was lower than DB-PTCDI-C13 since steric hindrance of alkyl moiety might have interrupted the nucleophilic attack. The red powder was obtained after chromatography. The chemical property was basically the same as DB-PTCDI-C13, which means its high solubility in common organic solvent such as methylene chloride and toluene.

2.3.4.2. Film process of DB-PTCDI-C18

DB-PTCDI-C18 was dissolved in 1% THF-containing toluene and the solution was used for spin coating. After annealing at 160°C for 1 hour, DFM image of DB-PTCDI-C18 displayed surface textures containing three-dimensional islands. All results are summarized in **Table 2.3.4.2.1**. The mobility values were extremely low or could not be obtained. Since appropriate annealing temperature is known to be decreased when alkyl chain increased⁸⁸⁻⁸⁹, lower annealing temperature was also tested. However, the situation could not be improved.

Table 2.3.4.2.1 Annealing temperature effect on DFM image of DB-PTCDI-C18 film

Exp. No.	Spin coating (times)	Annealing	DFM	FET
051217-1	3	80°C 1 hour	 041217-1	No conductivity
051217-2	3	100°C 1 hour	 041217-2	No conductivity
051217-3	3	120°C 1 hour	 041217-3	No conductivity
051217-4-21B	3	140°C 1 hour	 041217-4	n-type 6.39×10^{-7} $\text{cm}^2/\text{V s}$ (100 μm gap)

051217-5	3	160°C 1 hour	<div><p>041217-5</p></div>	No conductivity
051217-6	3	180°C 1 hour	<div><p>041217-6</p></div>	No conductivity
041217-7	3	-	<div><p>041217-7</p></div>	-

2.4 Conclusion

N-alkyl chain and bulky bromine atoms in DB-PTCDI-C13 improved solubility of PTCDI skeleton due to flexible long alkyl chain and twisting of the π -core, the latter of which has been confirmed by DFT calculation and XRD analysis. A 2 nm-thick spin coated film of this molecule (monolayer film of DB-PTCDI-C13) exhibited n-type FET behavior. The molecular ordering and associated electron mobility of solution-deposited films were affected by annealing temperature and time. From DSC thermogram, phase transitions related to liquid crystalline phases of DB-PTCDI-C13 were suggested to be an important factor to control the film quality and mobility. The highest mobility of DB-PTCDI-C13 film was $5.8 \times 10^{-3} \text{ cm}^2 \text{ V}^{-1} \text{ s}^{-1}$ after annealing at 160°C for 1 hour. Thus, DB-PTCDI-C13 is a successful reagent for monolayer FET with annealing.

Unfortunately, the development of monolayer n-type FET is not successful for perylene-coronene or pererylene-benzimidazole derivatives because of their own poor solubility. The purification and solution-deposition process could not be conducted. Unlike coronene and benzimidazole, DB-PTCDI-C18 was dissolved easily in common organic solvent as same as DB-PTCDI-C13. However, FET efficiencies of annealed spin-coating DB-PTCDI-C18 film were almost unable to be measured because of three-dimension island formation upon annealing at all temperature.

2.5 References

79. C. Huang, S. Barlow, S. R. Marder, *J. Org. Chem.* **2011**, *76*, 2386.
80. T. Choppawa, M. Sukwattanasinitt, S. Sahasithiwat, V. Ruangpornvisuti, P. Rashatasakhon, *Dyes Pigm.* **2014**, *109*, 175.
81. Y. Li, H. Zheng, Y. Li, S. Wang, Z. Wu, P. Liu, Z. Gao, H. Liu, D. Zhu, *J. Org. Chem.* **2007**, *72*, 2878.
82. W. Jiang, Y. Li, W. Yue, Y. Zhen, J. Qu, Z. Wang, *Org. Lett.* **2010**, *12*, 228.
83. W. Kohn, L. J. Sham, *Phys. Rev.* **1965**, *140*, A1133.
84. G. Kresse, J. Furthmüller, *Comput. Mater. Sci.* **1996**, *6*, 15.
85. J. P. Perdew, K. Burke, M. Ernzerhof, *Phys. Rev. Lett.* **1996**, *77*, 3865.
86. S. Grimme, J. Antony, S. Ehrlich, H. Krieg, *J. Chem. Phys.* **2010**, *132*, 154104.
87. A. V. Krukau, O. A. Vydrov, A. F. Izmaylov, G. E. Scuseria, *J. Chem. Phys.* **2006**, *125*, 224106.
88. H. Iino, T. Usui, J. Hanna, *Nat. Commun.* **2015**, *6*, 1.
89. M. Funahashi, *Polym. J.* **2009**, *41*, 459.
90. I. Vladimirov, M. Kellermeier, T. Geßner, Z. Molla, S. Grigorian, U. Pietsch, L. S. Schaffroth, M. Kühn, F. May, R. T. Weitz, *Nano Lett.* **2018**, *18*, 9.
91. H. Marchetto, T. Schmidt, U. Groh, F. C. Maier, P. L. Lévesque, R. H. Fink, H. J. Freunda, E. Umbachac, *Phys. Chem. Chem. Phys.* **2015**, *17*, 29150.
92. K. Vasseur, C. Rolin, S. Vandezande, K. Temst, L. Froyen, P. Heremans, *J. Phys. Chem. C.* **2010**, *114*, 2730

Chapter 3 Field effect measurements on n-doped acceptor films

3.1 Introduction

Mott FET (= field effect transistor) is an electronic element that switches conductance of a Mott insulator by applying gate voltage, which has been theoretically proposed as a high performance device and been realized both in organic and in inorganic devices. Appropriate organic materials for this purpose are charge transfer salts. In this work, potassium (K) was doped to n-type material. First, monolayer and bilayer of 1,7-dibromo-*N,N'*-ditridecyl-3,4,9,10-perylenetetracarboxylic diimide (DB-PTCDI-C13) were successfully fabricated by spin coating process as discussed in the previous chapter. Although potassium 1,7-dibromoperylenetetracarboxylic diimide salt (K_x -(DB-PTCDI-C13)) have never been discussed, we have tried to dope DB-PTCDI-C13 monolayer film by potassium evaporation. Not only DB-PTCDI-C13, but also K(TCNQ) crystals (TCNQ = tetracyanoquinodimethane) was tested for FET measurement. I-V characteristics of potassium doped DB-PTCDI-C13 and TCNQ will be discussed in this part.

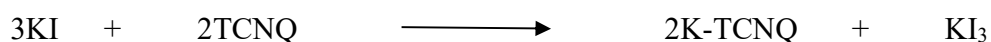
3.2 Experimental

3.2.1 Materials and instruments

Commercial 1,7-dibromo-perylene-3,4,9,10-tetracarboxylic dianhydride and TCNQ were purchased from Tokyo Chemical Industry (TCI, Japan). 1-aminotridecane, propionic acid, potassium iodide and common solvent were purchased from WAKO Pure Chemical Industries (Japan). $K_2Cr_2O_7$ was purchased from SAES. All commercially available chemicals were used without purification. P-doped Si substrates covered with a 300 nm-thick SiO_2 layer (SiO_2/Si) were cut into size of 6 by 6 mm². The electrodes were patterned by photo lithography. The Au/Ti electrode was deposited by sputtering method. Commercial $K_2Cr_2O_7$ tube was heated to evaporate potassium. The I-V characteristic study was conducted by 4200A-SCS parameter analyzer (Keithley). The temperature was regulated with LS336 temperature controller in combination with manual prober (Lake Shore Cryotronics). The morphology of the device surface was observed by DFM (dynamic force microscopy) while optical images for drop casted film were taken by microscope (Nikon, Japan).

3.2.2 Synthesis

3.2.2.1 Crystallization method (K-TCNQ crystals)



TCNQ (1.020 g, 5.00 mmol) was boiled in 100 ml of acetonitrile. Next, 15 ml boiled KI (2.491 g, 15.01 mmol) solution was added into hot TCNQ solution. After that, the mixture was boiled and kept overnight. The reddish purple crystals of K-TCNQ (92%) were obtained after

cooling to room temperature and were collected by vacuum filtration followed by washing with acetonitrile and ether.

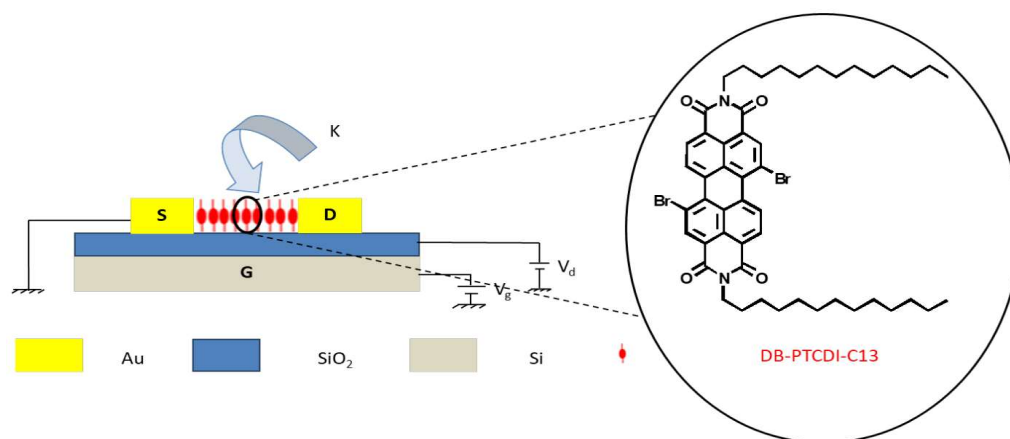
3.2.3 Fabrication of devices

3.2.3.1 Fabrication for potassium doped DB-PTCDI-C13 device

For spin coating process, DB-PTCDI-C13 (1 mg) was dissolved in toluene containing 1% THF (1 ml). After sonication, the solution was spin coated on SiO₂/Si substrate with the rate of 1500 r.p.m. Next, coated substrate was heated for annealing under argon atmosphere. All spin coated devices were prepared via this manner. (**Scheme 3.2.3.1.1**)

Drop cast film was prepared by similar manner. After sonication, the solution was dropped and dried at room temperature on bare SiO₂/Si. The annealing process was conducted under argon atmosphere.

In order to dope potassium, annealed DB-PTCDI-C13 devices were loaded in the vacuum chamber. At 10⁻⁶ torr, K₂Cr₂O₇ tube was heated and potassium was deposited on the devices. The annealing was again conducted to facilitate the charge transfer process.



Scheme 3.2.3.1.1. Conceptual device scheme for monolayer Mott FET preparation based on DB-PTCDI-C13

3.2.3.2 Fabrication of K-TCNQ devices

3.2.3.2.1 Evaporation method (K-TCNQ amorphous film)

To achieve the K-TCNQ film, 30 nm TCNQ thin film was deposited by evaporation on SiO₂/Si substrate. After that, 2 nm K was sublimed on top of TCNQ/SiO₂/Si substrate without thermal treatment.

3.2.3.2.2 Recrystallization method (K-TCNQ thin crystal)

In order to prepare the device, 1mg K-TCNQ was dissolved in boiled 1 ml acetonitrile; and then, cleaned SiO₂/Si substrate with gold-patterned source/drain electrodes was immersed and kept overnight. The K-TCNQ crystal was obtained on the bottom-gate SiO₂/Si substrate.

3.2.4 Performance evaluation

The mobility (μ) was obtained from drain current (I_d) and gate voltage (V_g) plots. First, conductivity (σ) presents the relationship with drain current, electrode gap length (L) and width of the electrode (W) which follow this equation:

$$\sigma = I_d * \frac{L}{W} \quad (\text{eq. 1})$$

After plot of conductivity depending on the gate voltage, the mobility in linear regime is given by,

$$\mu = \frac{d}{\varepsilon_0 \varepsilon'} * \frac{d\sigma}{dV_g} \quad (\text{eq. 2})$$

where d is the thickness of SiO₂ insulating layer (300 nm), ε_0 is vacuum permittivity of electric constant (8.85×10^{-12} F/m) and ε is relative permittivity of SiO₂ (3.9).

3.3 Results and discussion

3.3.1 K_x (DB-PTCDI-C13)

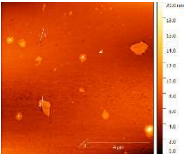
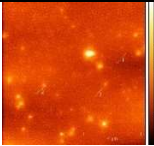
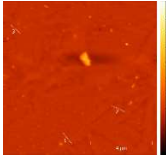

3.3.1.1 Potassium (K) doping of DB-PTCDI-C13 film

DB-PTCDI-C13 solution was spin coating on patterned SiO₂/Si for 3 times. After 5 nm K-doping, the conductivity of all devices was measured. Next, the DFM technique was applied to check morphology of the film made of DB-PTCDI-C13 and K. The annealing process was set up in 2 types, namely, the pre-annealing and the post-annealing. The annealing condition is at 160°C for 1 hour. The pre-annealing is the process that heated the device before K-doping. And then, the conductivity was measured in vacuum chamber. In the opposite way, post-annealing is the process that heated the device after K-doping. Unfortunately, most of devices did not show any conducting behaviors, whose results are exhibited in **Table 3.3.1.1.1**. The DFM images were recorded as shown in the table. The images displays that the compound layer is divided into small islands (**Table 3.3.1.1.1**. Run 4), even though post-annealing was avoided. In case of the post-annealing process, (**Table 3.3.1.1.1**. Run 3) the molecules are totally lost. The K might be blended with DB-PTCDI-C13 in Run 4. However, the author could not obtain any evidence to indicate such a reaction.

The author also tried potassium concentration optimization. The thickness was decreased by 10 times. After 0.5 nm K-doping, the conductivity of all devices was measured. Unfortunately, none of devices showed any conducting behaviors again.

In conclusion, K-doping was not successful. In the other word, since the three-dimensional sparse islands were obtained after potassium doping, the conductivity could not be measured even though a charge transfer salt might be generated after doping.

Table 3.3.1.1.1 Conclusion of potassium doping with 3 times spin coated DB-PTCDI-C13 film

Run	Pre annealing	K	Post annealing	AFM	FET
1	160 °C 1 hour	-	-		n-type 2.64×10^{-3} $\text{cm}^2/\text{V s}$ (100 μm gap)
2	-	-	-		No conductivity
3		5 nm	160 °C 1 hour		No conductivity
4	160 °C 1 hour	5 nm	-		No conductivity
5	-	0.5 nm	160 °C 1 hour	-	No conductivity
6	160 °C 1 hour	0.5 nm	160 °C 1 hour	-	No conductivity

In order to connect the island-like doped materials, the author also tried with 10 times spin coating to expect bridging of the islands to the electrodes. DB-PTCDI-C13 solution was spin coating on SiO₂/Si for 10 times. The annealing process was set up at 160°C for 1 hour. After 0.5 nm K-doping and 10 nm of guanine for moisture protection, all devices were measured for the conductivity evaluation. The diffusion methods are 2 types, annealing and non-annealing. The annealing is the process that heated the device at 160°C for 1 hour after doping. And then, the conductivity was measured in the vacuum chamber. On the other hand, non-annealing is the process that kept device after doping for 1 day under argon atmosphere at room temperature. Unfortunately, all of devices did not show any FET behaviors which are shown in **Figure 3.3.1.1.1**. The DFM images were captured in **Table 3.3.1.1.2 (101117)**. The images display that the K might be blended with DB-PTCDI-C13.

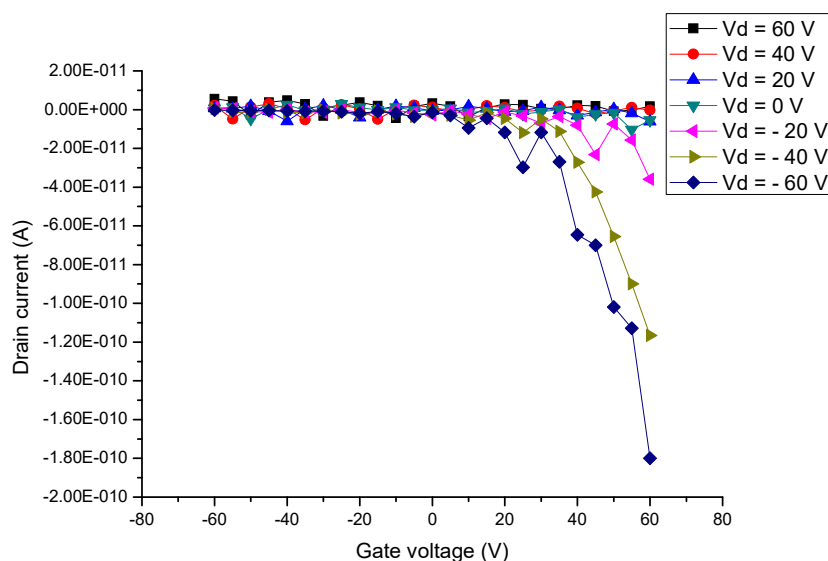


Figure 3.3.1.1.1 Conductivity measurement results with 0.5 nm K-doping with DB-PTCDI-C13 by pre-annealing process at 100 μ m gap

Next, we also increased amount of potassium to 5 nm while 10 nm of guanine was again coated for moisture protection⁹³. The conductivity of all devices was measured with semiconductor parameter analyzer. The diffusion methods were 2 types, namely annealing and non-annealing. The results are exhibited in **Figure 3.3.1.1.2**. However, the conductivity was very poor. The DFM images are also shown in **Table 3.3.1.1.2 (Run 3 and 4)**. The images display that the potassium seems to be blended with DB-PTCDI-C13.

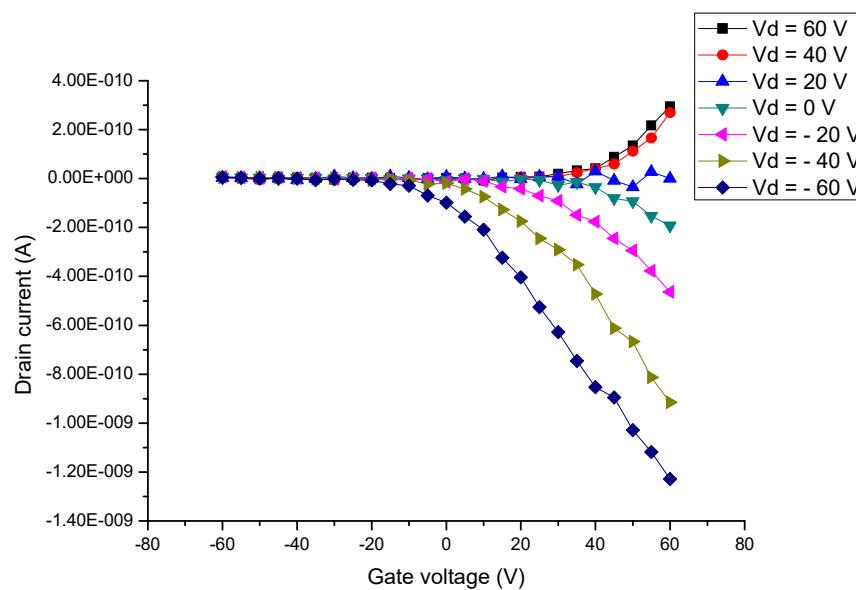
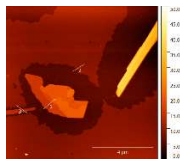
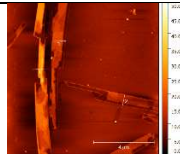
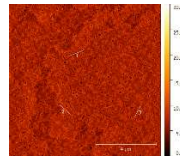

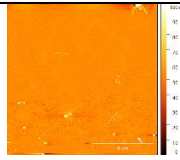
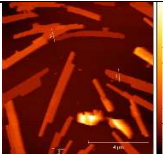
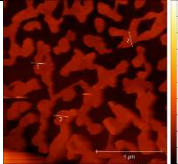
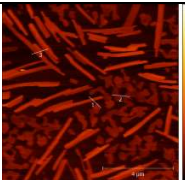
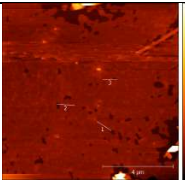
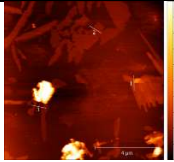


Figure 3.3.1.1.2 I_d - V_g plot for DB-PTCDI-C13 film doped by 5-nm potassium with annealing process, measured at 100 μ m gap

Table 3.3.1.1.2 Conclusion of potassium doping with 10 times spin coated DB-PTCDI-C13 film

Run	Pre annealing	K	Post annealing	AFM	FET
1	160 °C 1 hour	0.5 nm (10 nm guanine)	-	 101117-f4	No conductivity
2	-	0.5 nm (10 nm guanine)	160 °C 1 hour	 101117-a4	No conductivity
3	-	5 nm (10 nm guanine)	160 °C 1 hour	 161117-2-a4	No conductivity
4	160 °C 1 hour	5 nm (10 nm guanine)	-	 161117-1-f4	No conductivity
5	-	-	-	 131117-nonanneal160	No conductivity
6	160 °C 1 hour	-	-		-

				 131117-anneal160	
7	140 °C 1 hour	-	-	 201117-140°C	No conductivity
8	120 °C 1 hour	-	-	 201117-120°C	No conductivity
9	100 °C 1 hour	-	-	 201117-100°C	No conductivity
10	80 °C 1 hour	-	-	 201117-80°C	n-type $2.65 \times 10^{-4} \text{ cm}^2/\text{V s}$ (100 μm gap)

3.3.1.2 Cesium (Cs) doping of DB-PTCDI-C13 film

DB-PTCDI-C13 solution was spin coated on SAM-modified SiO_2/Si for 3 times. After 3 nm Cs-doping, all devices were measured for the conductivity evaluation. The diffusion method was non-annealing, which kept device still after doping for 1 day under argon atmosphere. Unfortunately, none of devices showed any conducting behaviors.

3.3.2 K-TCNQ

3.3.2.1 Evaporation method

In the previous section, the author tested K-doping to DB-PTCDI-C13 film with combination of annealing. However, doped film of the PTCDI derivative was not suitable for FET measurement. They formed three-dimensional islands after doping whose length was not long enough to bridge the electrodes. Not only potassium, but also cesium gave the same result.

The same doping procedure was conducted with evaporated TCNQ (yellow powder) film. When potassium is deposited after TCNQ film evaporation, the color of the device surface was changed from yellow into blue (**Figure 3.3.2.1.1**). Although there was no FET behavior, it was conducting as the film was bridging the electrodes. Thus, our potassium evaporation process was successful to dope electrons into organic layer such as TCNQ. Hence, we concentrated on FET properties of spin-Peierls insulator K(TCNQ), that is emerging from high temperature Mott-insulating state of this material.

After potassium doping, the yellow film was changed into blue. It was not only color

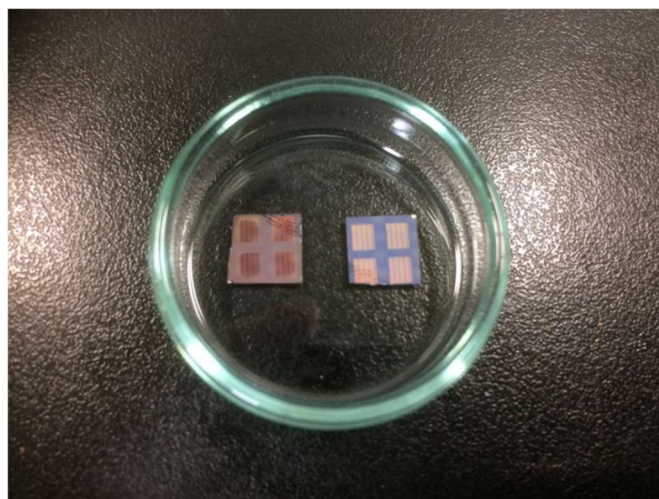


Figure 3.3.2.1.1 Prepared device of 30 nm TCNQ before potassium evaporation (left) after potassium evaporation 2 nm (right)

change but also electric characteristic change. Drain current (I_d) - drain voltage (V_d) plot of K-TCNQ film were conducted with variation of gate voltage (V_g). This is contrasting to the fact

that the device without potassium doping showed no conducting or FET behavior, which could be ascribed to amorphous state of TCNQ. If the quality of the film becomes improved, this device could be a Mott FET.

The morphology was investigated by DFM (dynamic force microscopy) image (**Figure 3.3.2.1.2b**). The DFM image explained that connection of dot-like particle was reasonable description.

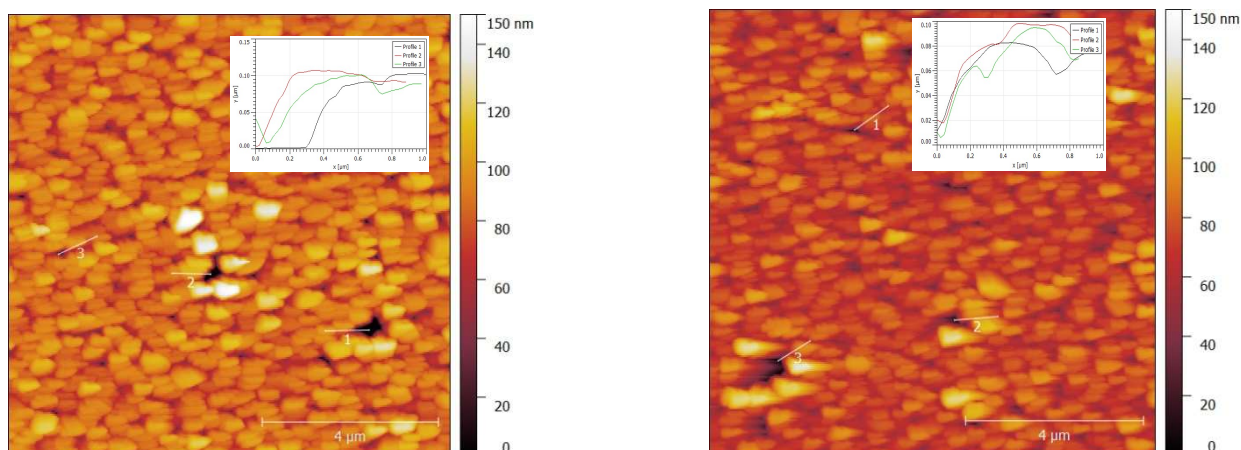


Figure 3.3.2.1.2. DFM image of (left) annealing device (right) non-annealing device (insets) the height profile of the films

3.3.2.2 Recrystallization method

1 mg K-TCNQ was recrystallized in 1 ml acetonitrile. After that, the cleaned SiO₂/Si substrates were immersed in the prepared solution. After drying the solvent, the conductivity of all devices was measured. The electronic property of synthesized K-TCNQ crystals was acquired from drain current (I_d) and drain voltage (V_d) curve (**Figure 3.3.2.2.1.**). This curve displayed that a decrease of gate voltage could cause an increase of drain current. Thus, this device can be classified as p-type FET. This contrasts to the literature reports on TCNQ, where the FET shows n-type behavior. Therefore, the doping inverted the FET behavior into p-type FET. It is expected that the band structure is totally changed by spin-Peierls transition, and the property of K(TCNQ) is not at all the same with the original TCNQ.

The mobility of K-TCNQ crystals was calculated in the previously mentioned manner. At 30 μm , gap, K-TCNQ crystals showed the highest mobility (**Figure 3.3.2.2.2a**). Conductivity was suppressed during the expansion of electrode gap to 50 μm . To ensure this phenomenon, the morphology was investigated by optical microscope image (**Figure 3.3.2.2.2b**). The OPM image tells us that smaller crystal size than 50 μm with random orientation could be related to the suppression of mobility. The author also observed decreasing of drain current during the measurement (**Figure S 3.3.2.2.1-3.3.2.2.3 in Appendix**), probably because of degradation of the contact.

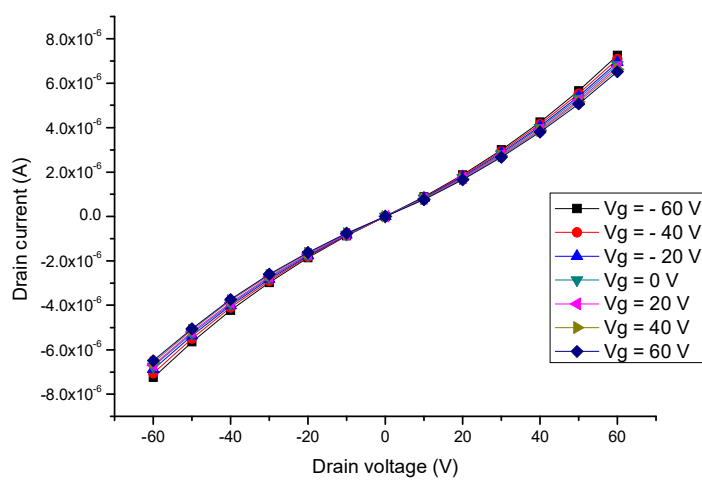
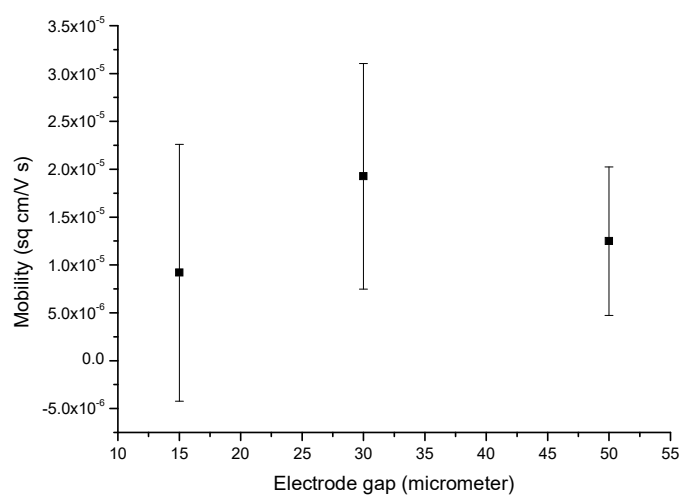


Figure 3.3.2.1. I_d - V_d characteristic of K-TCNQ crystals at 30 μ m electrode gap

(a)



(b)

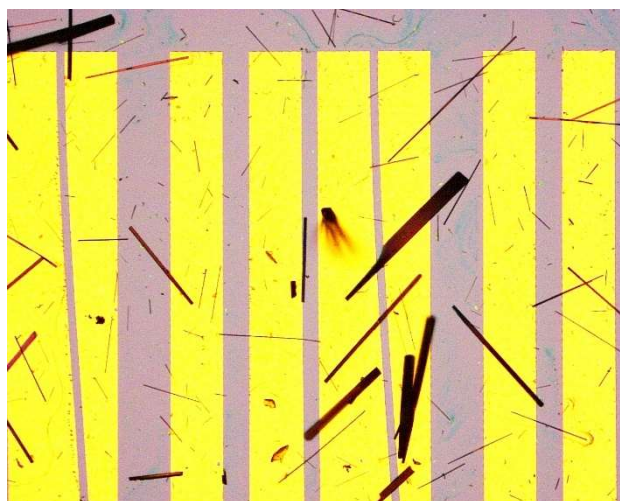


Figure 3.3.2.2.2 (a) Mobility of K-TCNQ crystals (b) OPM image of K-TCNQ on substrate

3.3.2.3. Electrochemical method

The crystals were synthesized by electrochemical synthesis at room temperature. To prepare the crystals, TCNQ and potassium benzene 1,2 disulphonate was dissolved in mixture of acetonitrile:toluene 3:2. After sonication, the solution was filtered and added in a glass chamber under inert atmosphere. After that, electrochemical reduction was conducted at the platinum electrode. At 10 μ A for 1 day, the crystals were obtained.

The plot between current density and drain voltage is displayed in **Figure 3.3.2.3.1**. The results exhibited that thin single crystal showed FET property but several thin crystals showed as conductor in **Figure 3.3.2.3.2**. The crystal morphology was characterized by Optical Microscope in **Figure 3.3.2.3.3 and 3.3.2.3.4**.

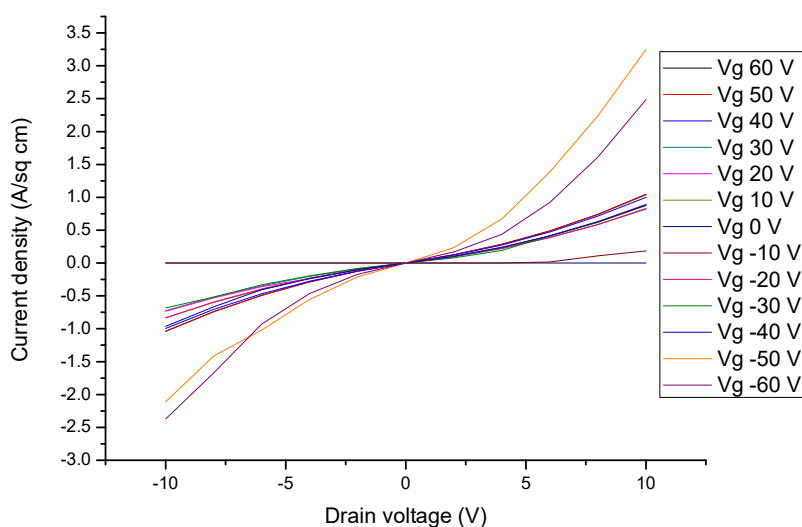


Figure 3.3.2.3.1 Current density and drain voltage plot of single crystal device

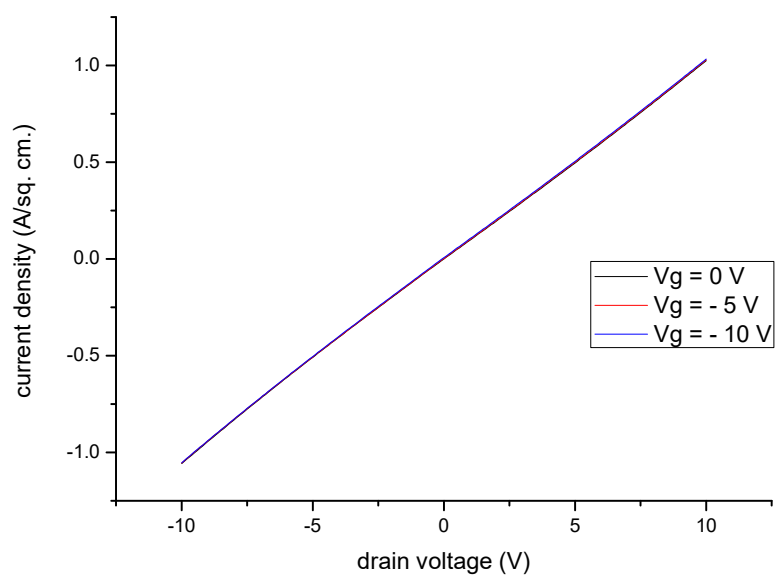


Figure 3.3.2.3.2 Current density-drain voltage result several crystals device

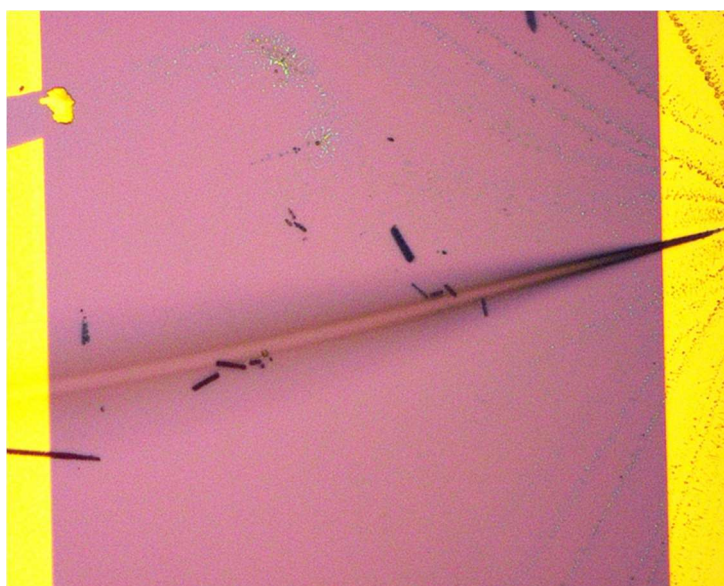


Figure 3.3.2.3.3 Optical microscope image of single crystal device



Figure 3.3.2.3.4 Optical microscope image of several crystals device

The I_d (drain current) and V_g (gate voltage) relationship of single crystal device is exhibited in **Figure 3.3.2.3.5**. The result showed ambipolar behavior. The p-type mobility value is $0.047 \text{ cm}^2/\text{V s}$ from -50 to -60 of gate voltage. The n-type mobility value is $0.036 \text{ cm}^2/\text{V s}$ from 50 to 60 of gate voltage. Although the switching is very sharp in this device, this might be due to a mechanical motion of the crystal that is not connected tightly to the electrodes.

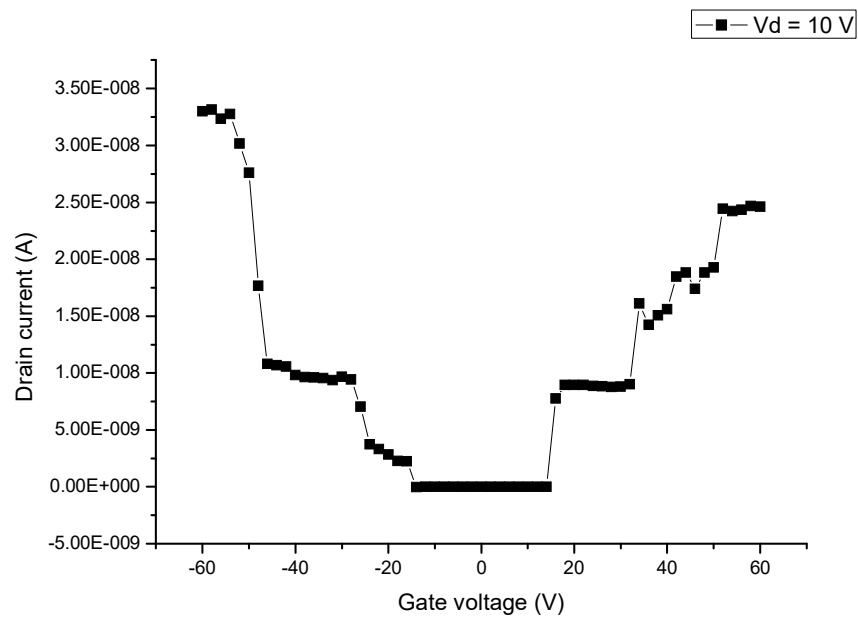


Figure 3.3.2.3.5 I_d (drain current) and V_g (gate voltage) relationship of single crystal device

3.4 Conclusion

DB-PTCDI-C13 solution was successfully spin coated on SiO_2/Si substrate and annealed at 160 °C for 1 hour. After deposition of potassium and cesium, all devices were measured for the conductivity evaluation. DFM image was also measured to check morphology of DB-PTCDI-C13 after reaction with potassium and cesium. Unfortunately, most of devices did not show any conducting behaviors and the DFM image showed sparse island morphology. The image implied that two-dimensional film was transferred to the three-dimensional islands after doping to diminish the electrical connection. Consequently, Mott-insulating state from potassium doped DB-PTCDI-C13 device was not able to be confirmed. Measurement on potassium doped DB-PTCDI-C13 will be tried in future experiments.

K-TCNQ film (potassium tetracyanoquinodimethane) was successfully synthesized via sublimation in high vacuum chamber. I-V characteristic study exhibited conducting behavior at room temperature. In this work, TCNQ film before potassium deposition didn't show any FET or conducting behavior. This indicated this film might be Mott (or Spin-Peierls) insulator.

Moreover, we tried K(TCNQ) synthesis. The K(TCNQ) crystals were successfully obtained. After recrystallization on SiO_2/Si substrate, these devices exhibited p-type behavior. Generally, TCNQ is n-type FET. As a result, doping turned the FET behavior into p-type. The result seems that field-effect on Spin-Peierls state of K(TCNQ) device was confirmed.

3.5 References

93. Jeon, P. J.; Lee, K.; Park, E. Y.; Im, S.; Bae, H. Ultrasensitive low power-consuming strain sensor based on complementary inverter composed of organic p- and n-channels . *Org. Electron.* 32 (2016): 208-212.

Chapter 4 Conclusion

In this study, the author tried to fabricate monolayer FET that can be doped and transformed into Mott-insulator FET. Although many types of pi-conjugated acceptor molecules were successfully synthesized, they were not very stable or very soluble in common organic solvents. The author obtained monolayer FET only with DB-PTCDI-C13. Spin coated monolayer film of DB-PTCDI-C13 molecule exhibited n-type FET behavior. The molecular ordering and associated electron mobility of solution deposited films were improved by annealing temperature and time. However, doped DB-PTCDI-C13 film was transformed into three-dimensional islands after reaction, which precluded further investigation as FET.

Despite that TCNQ could not form a monolayer, K(TCNQ) could show p-type FET behavior when its single crystal is laminated on bottom gate substrate. This FET polarity is totally different from that of neutral TCNQ. Therefore this FET seems to be a spin-Peierls FET. In future, more examples of Mott FET and spin-Peierls FET will be obtained by improving the fabrication processes and molecular designs.

Chapter 5 Appendix

#:1 保持時間:2.555(スキャン#:112)
 ピーク数:817
 スペクトル:シングル 2.555(112) ベースピーク:135.10(1514)
 バックグラウンド:なし グループ 1 - イベント 1

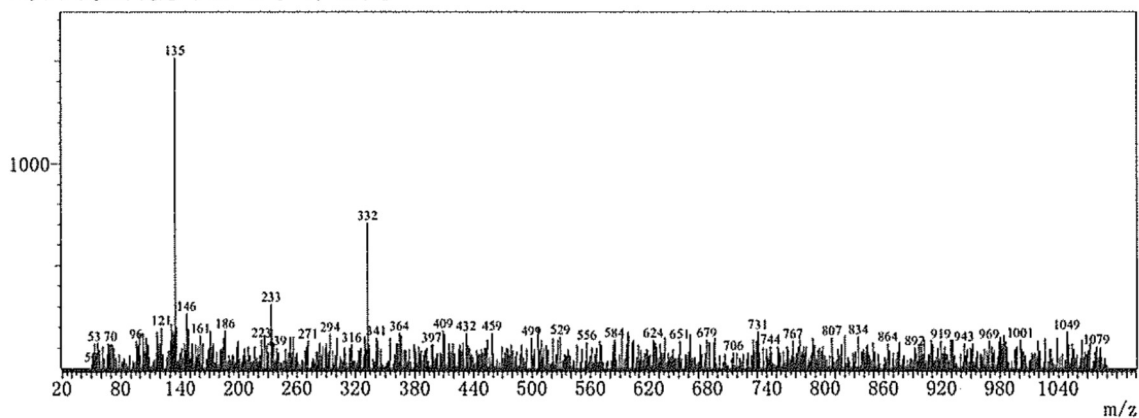


Figure S. 2.3.1.1.1 GC-MS spectrum of 4,5-dioctyl-1,2-phenylene diamine

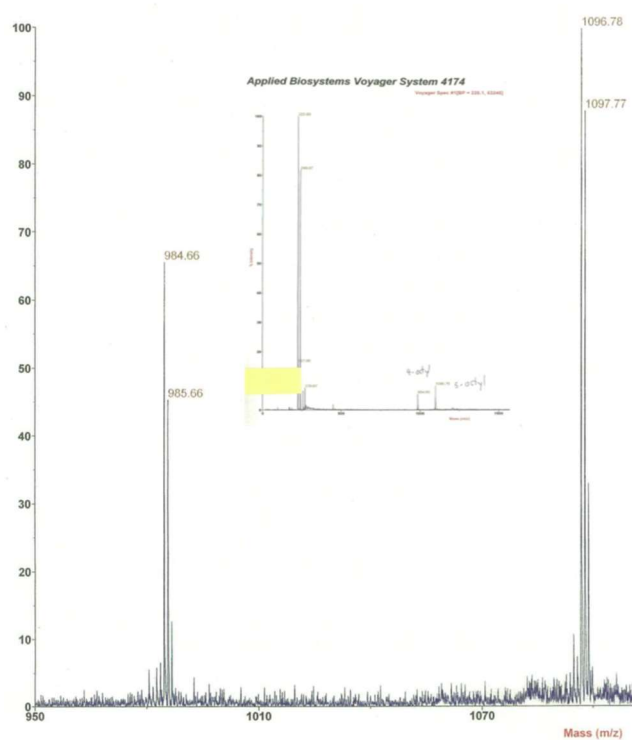


Figure S. 2.3.1.1.2 MALDI-TOF mass spectrum of synthesized perylenebis-benzimidazole

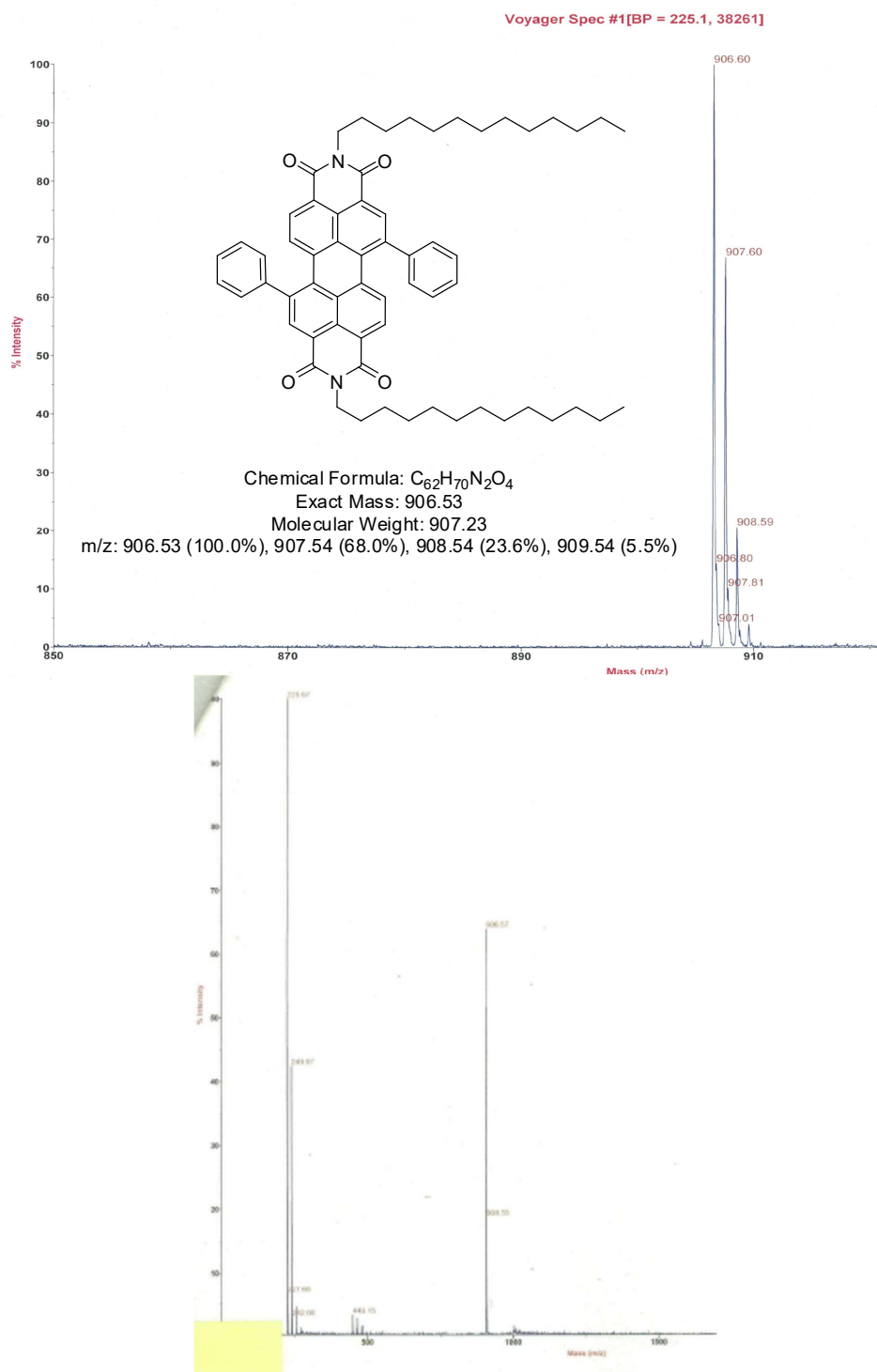


Figure S. 2.3.2.1.1 MALDI-TOF mass spectrum of 1,7-diphenyl-*N,N*-ditridecyl-perylene-3,4,9,10-tetracarboxylic diimide (DPH-PTCDI-C13) before light exposure

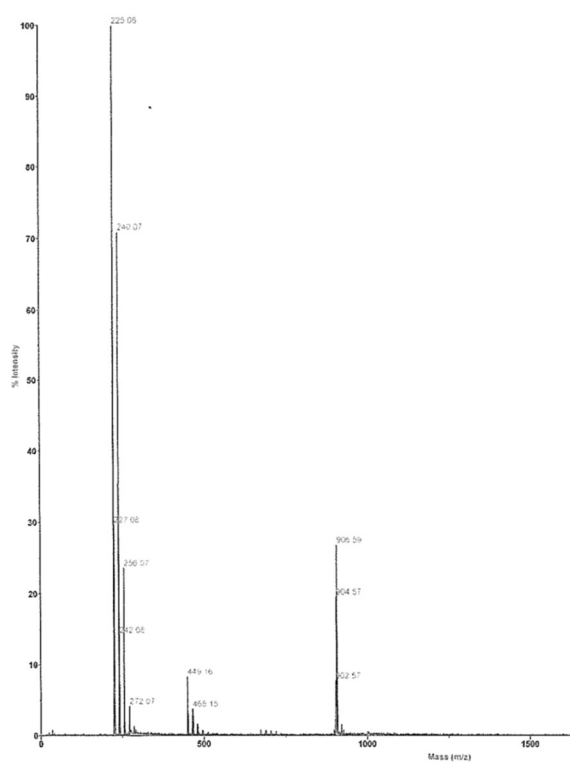
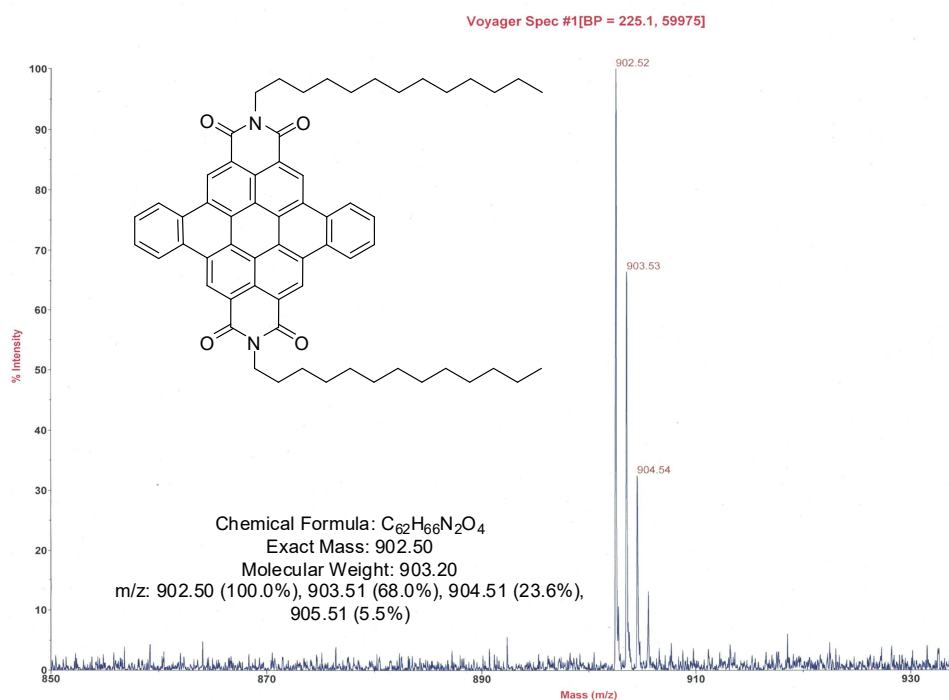


Figure S. 2.3.2.1.2 MALDI-TOF mass spectrum of 1,7-diphenyl-*N,N*-ditridecyl-perylene-3,4,9,10-tetracarboxylic diimide (DPH-PTCDI-C13) after light exposure 48 hours

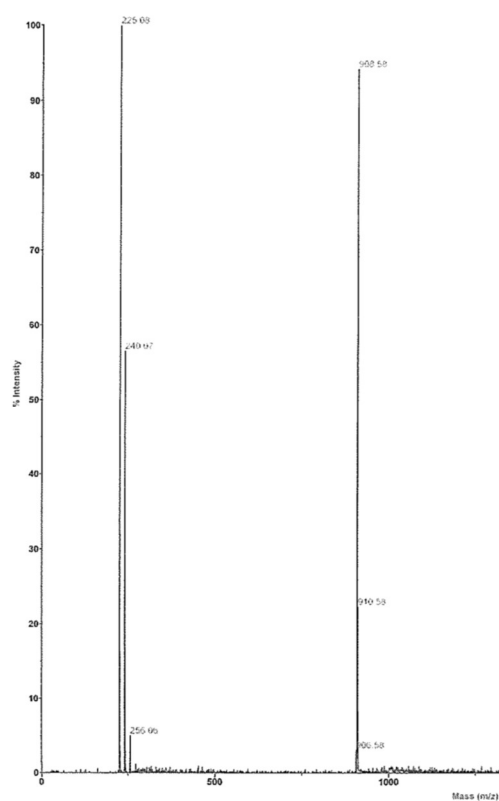
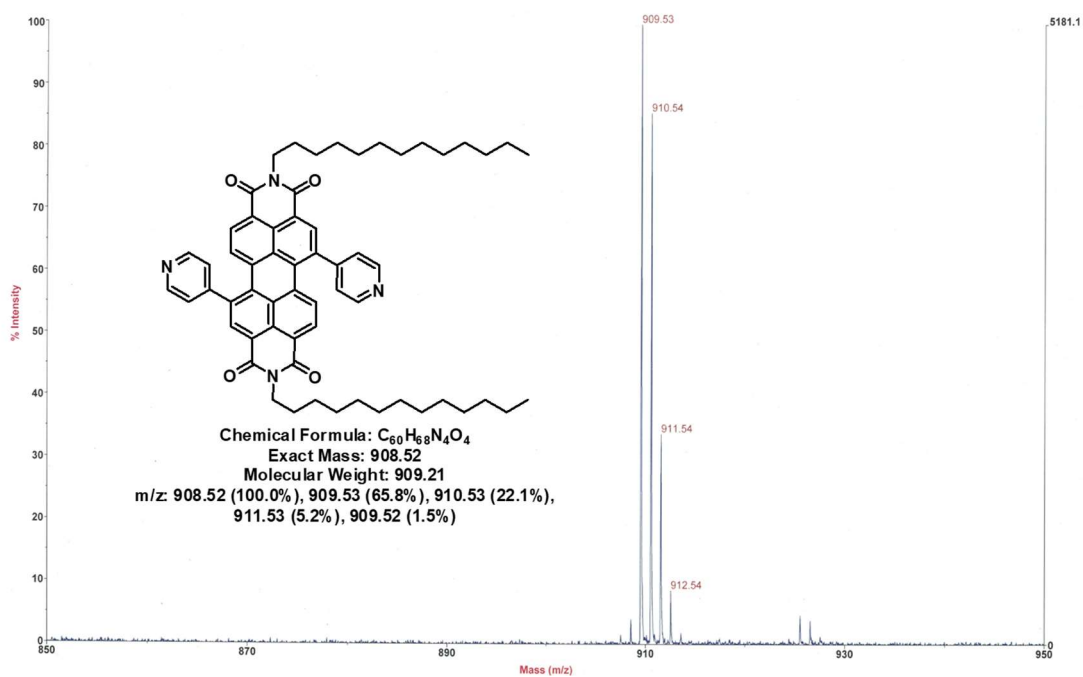


Figure S. 2.3.2.1.3 MALDI-TOF mass spectrum of 1,7-dipyridyl-*N,N*-ditridecyl-perylene-3,4,9,10-tetracarboxylic diimide (DPY-PTCDI-C13) before light exposure

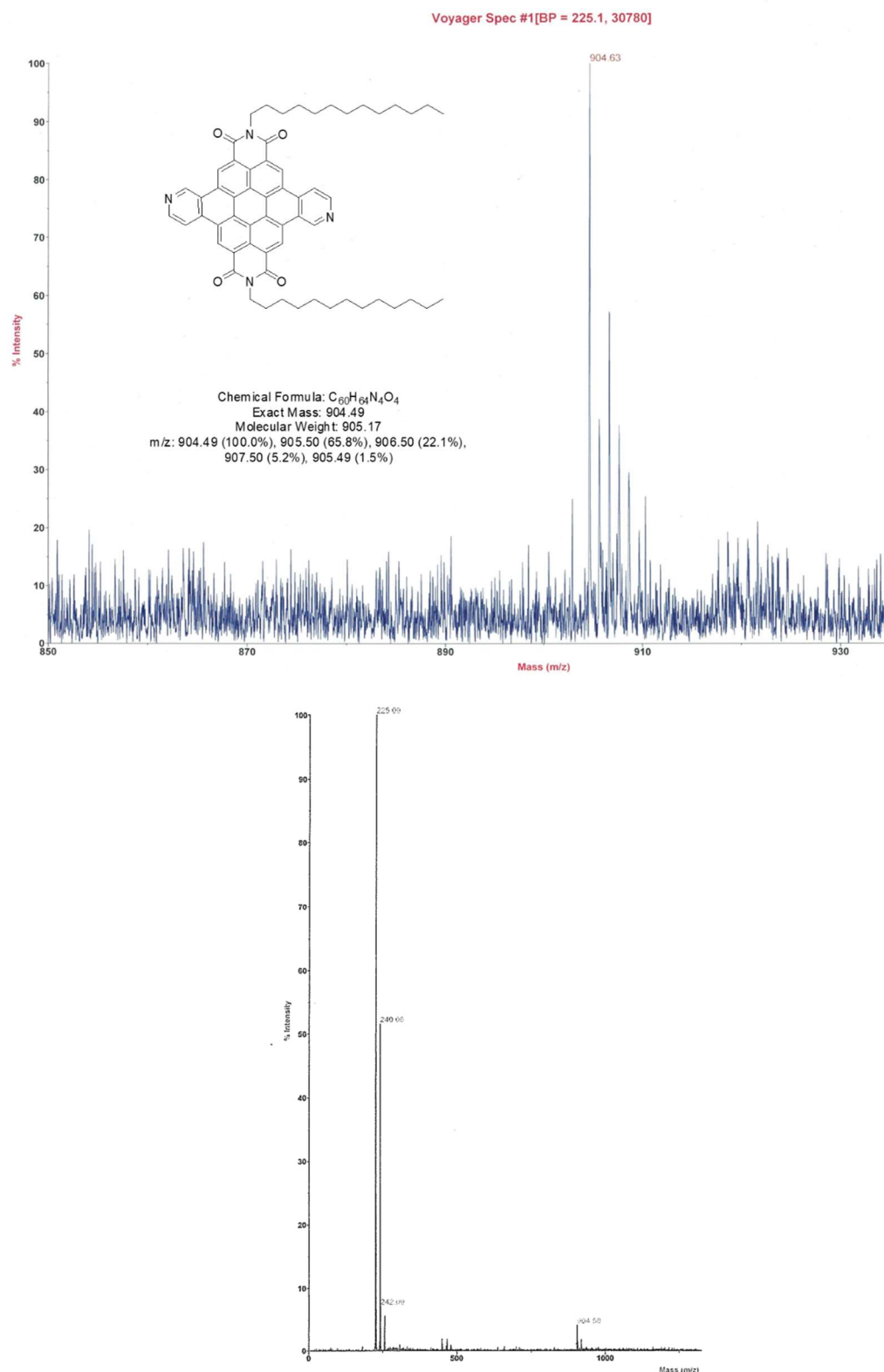


Figure S. 2.3.2.1.4 MALDI-TOF mass spectrum of 1,7-dipyridyl-*N,N*-ditridecyl-perylene-3,4,9,10-tetracarboxylic diimide (DPY-PTCDI-C13) after light exposure 48 hours

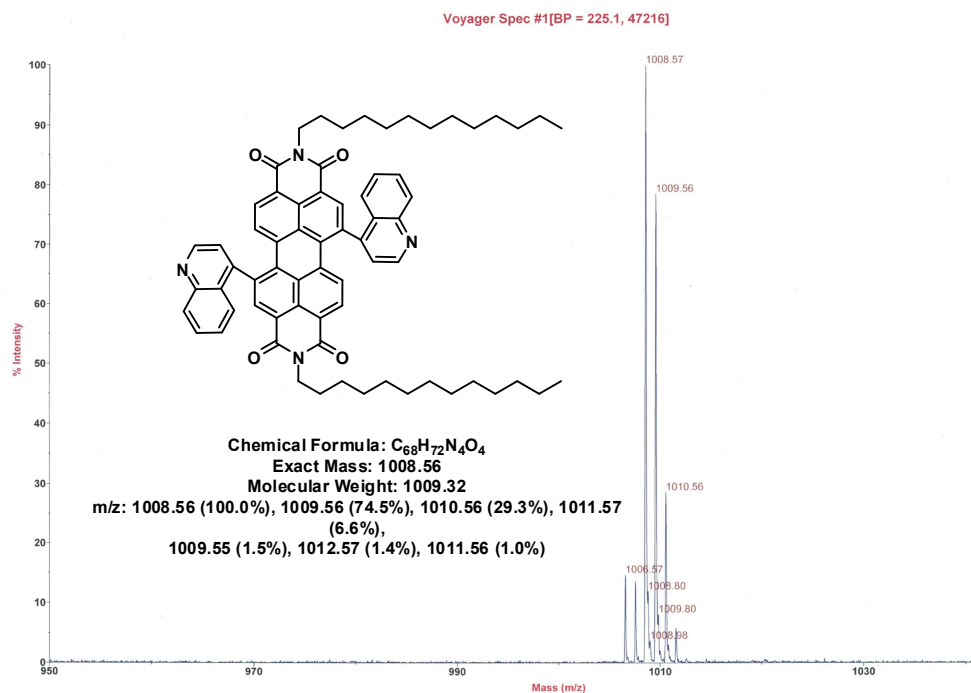


Figure S. 2.3.2.1.5 MALDI-TOF mass spectrum of 1,7-diquinolidyl-*N,N*-ditridecylperylene-3,4,9,10-tetracarboxylic diimide (DQ-PTCDI-C13) before light exposure

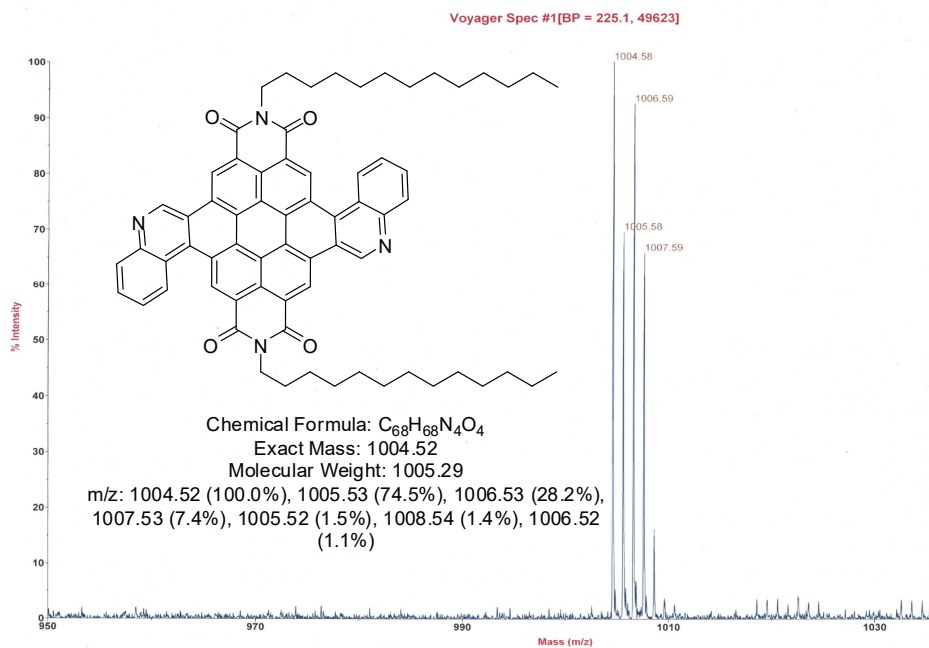


Figure S. 2.3.2.1.6 MALDI-TOF mass spectrum of 1,7-diquinolidyl-*N,N*-ditridecylperylene-3,4,9,10-tetracarboxylic diimide (DQ-PTCDI-C13) after light exposure 48 hours

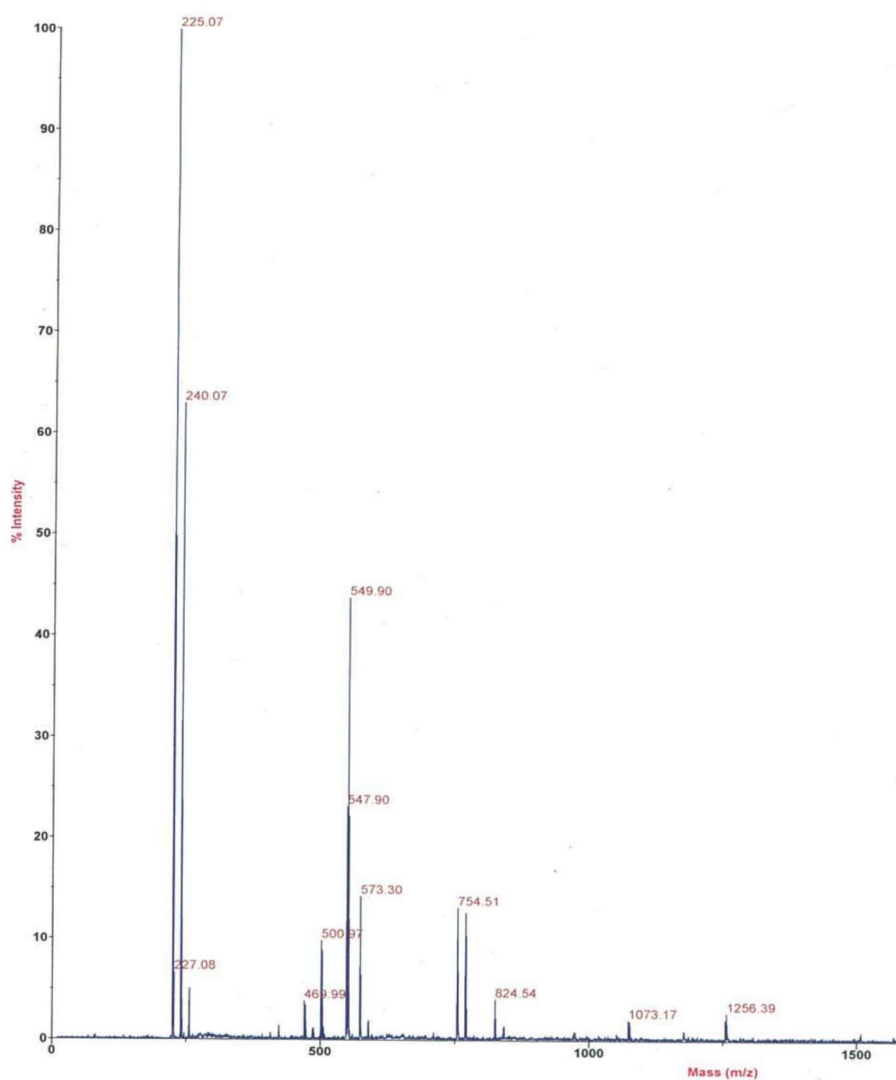


Figure S. 2.3.2.1.7 MALDI-TOF mass spectrum of 1,7-dithiophenyl-*N,N*-ditridecylperylene-3,4,9,10-tetracarboxylic diimide (DTP-PTCDI-C13) before light exposure

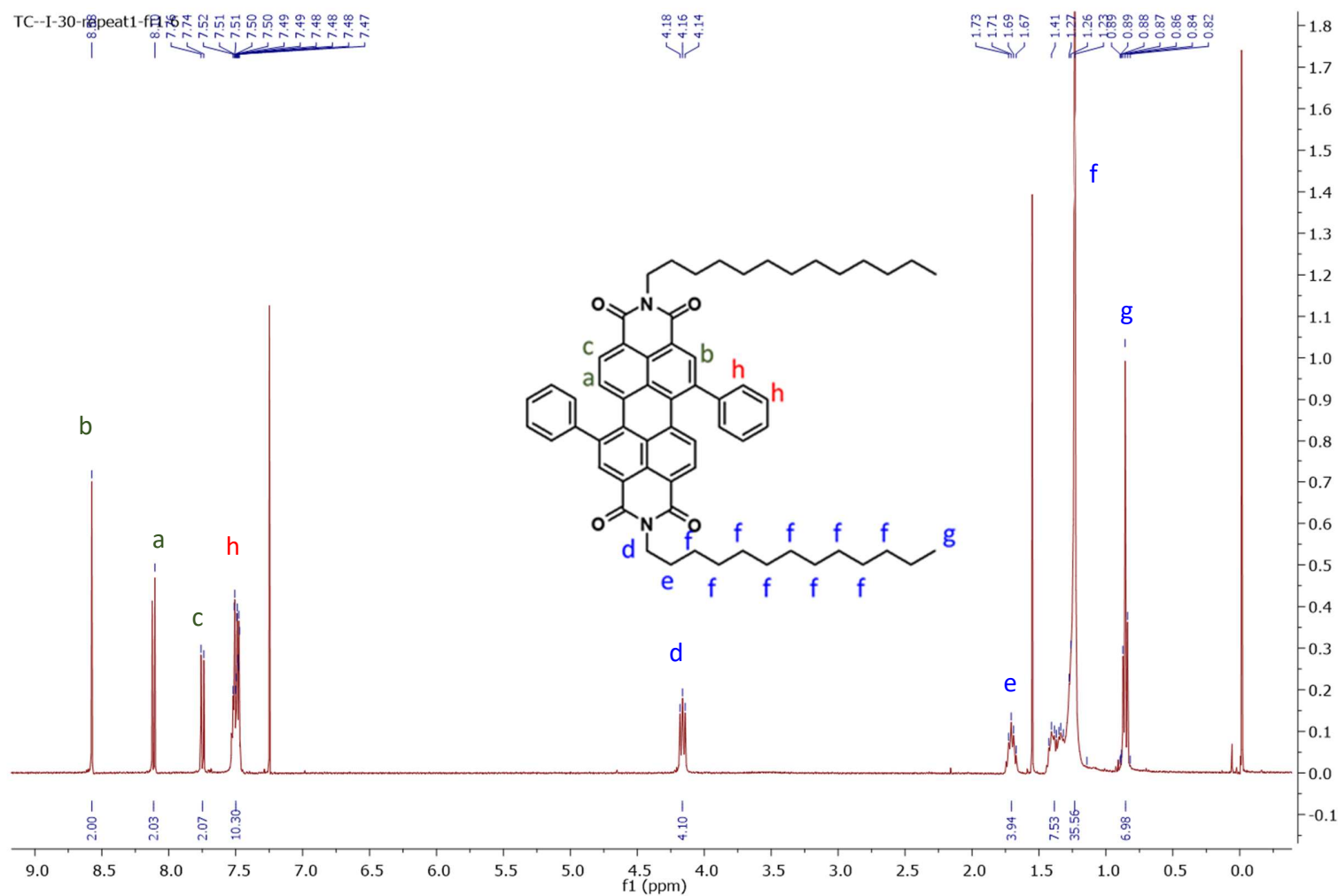


Figure S. 2.3.2.1.8 ^1H -NMR spectrum of 1,7-diphenyl-*N,N*-ditridecyl-perylene-3,4,9,10-tetracarboxylic diimide (DPH-PTCDI-C13) before light exposure

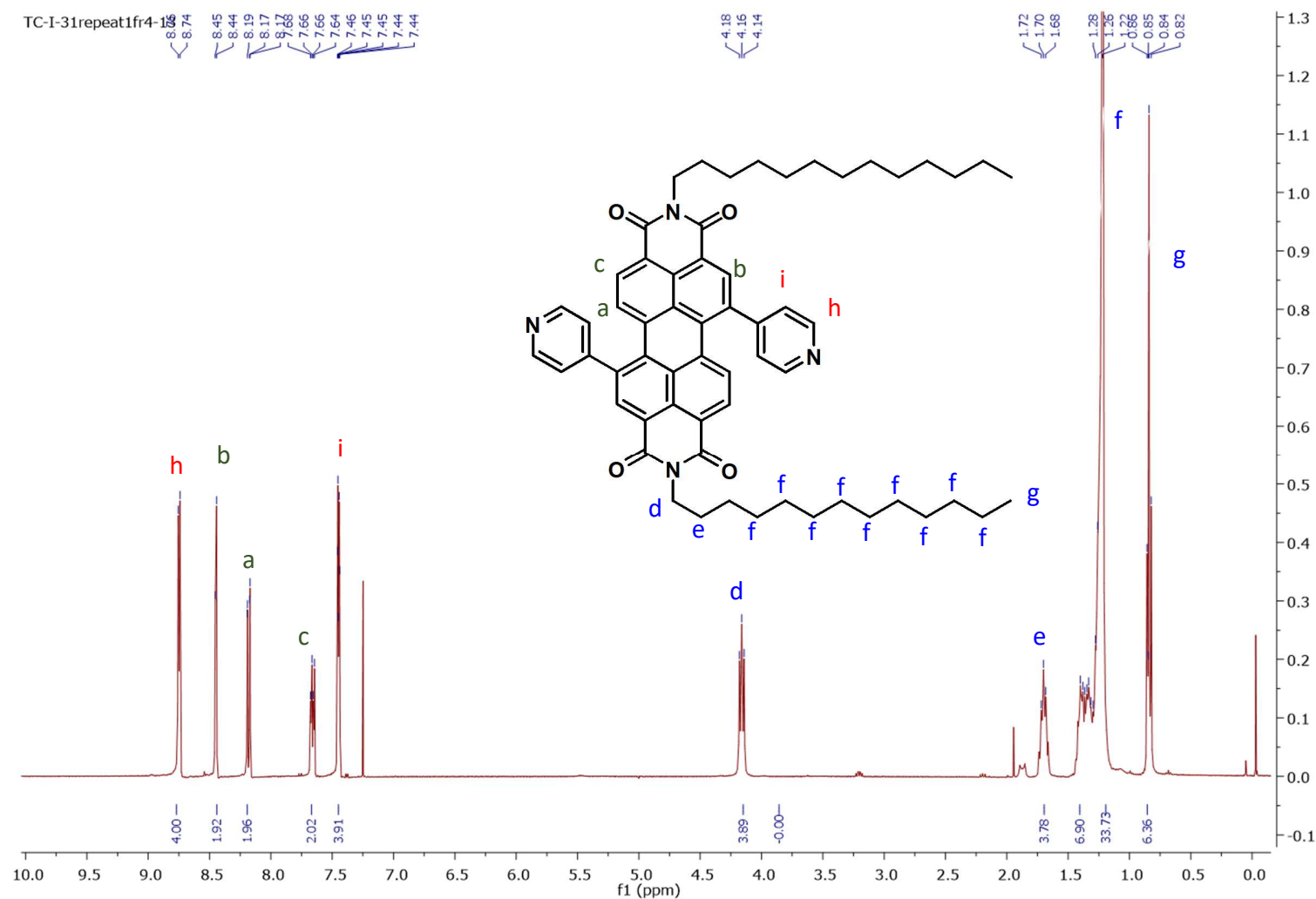


Figure S. 2.3.2.1.9 ^1H -NMR spectrum of 1,7-dipyridyl-*N,N*-ditridecyl-perylene-3,4,9,10-tetracarboxylic diimide (DPY-PTCDI-C13) before light exposure

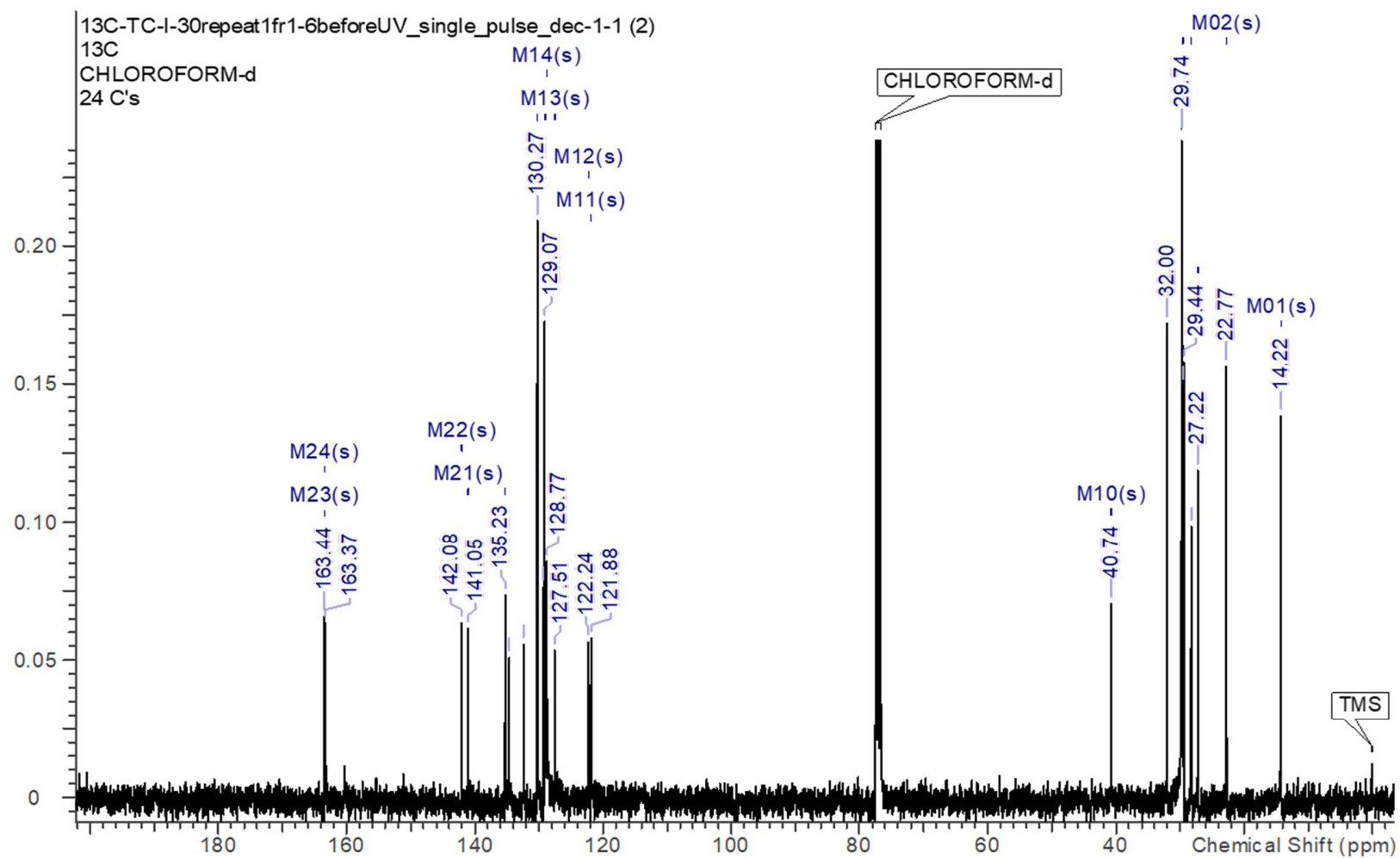


Figure S. 2.3.2.1.10 ^{13}C -NMR spectrum of 1,7-diphenyl-*N,N*-ditridecyl-perylene-3,4,9,10-tetracarboxylic diimide (DPH-PTCDI-C13) before light exposure

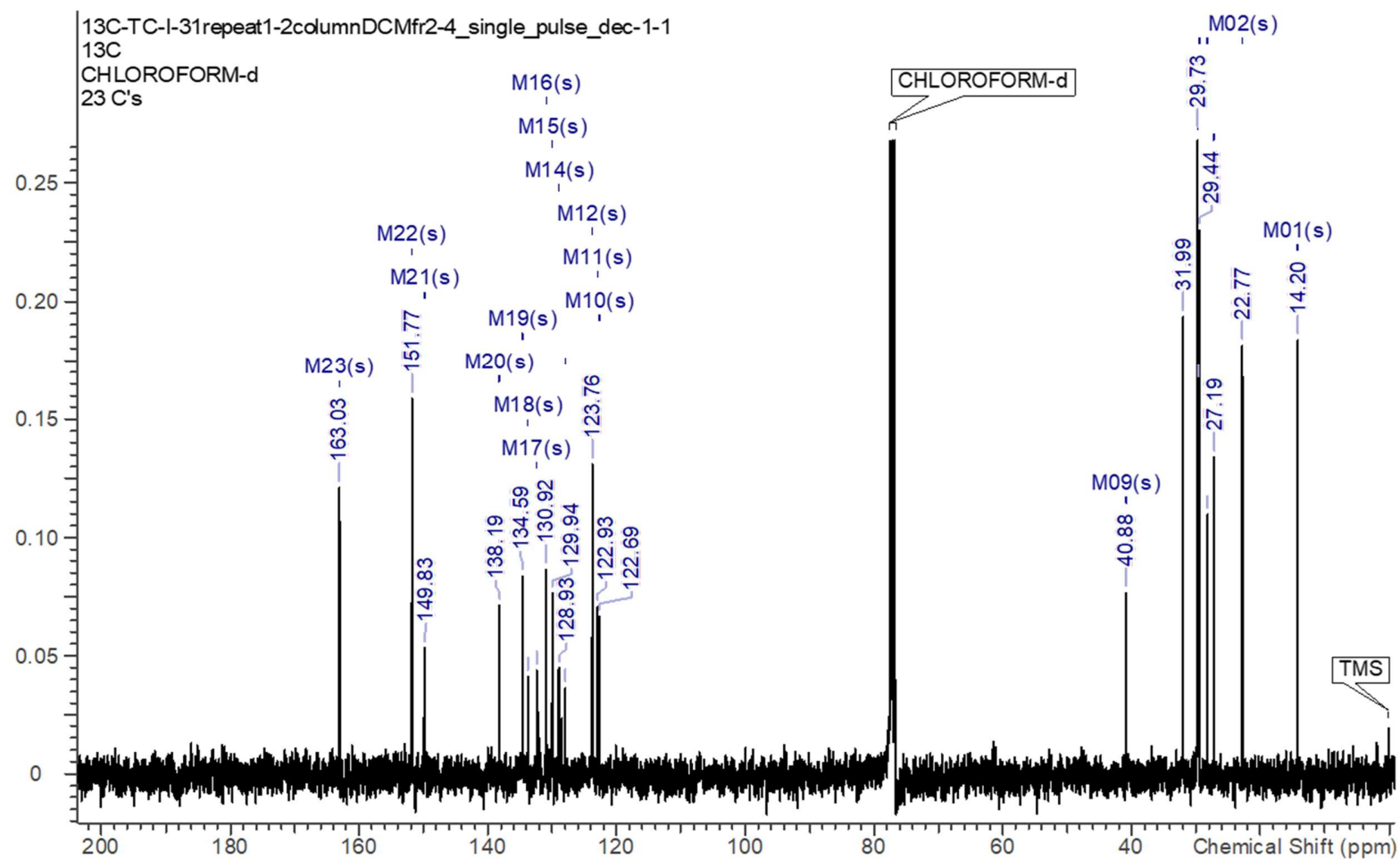


Figure S. 2.3.2.1.11 ^{13}C -NMR spectrum of 1,7-dipyridyl-*N,N*-ditridecyl-perylene-3,4,9,10-tetracarboxylic diimide (DPY-PTCDI-C13) before light exposure

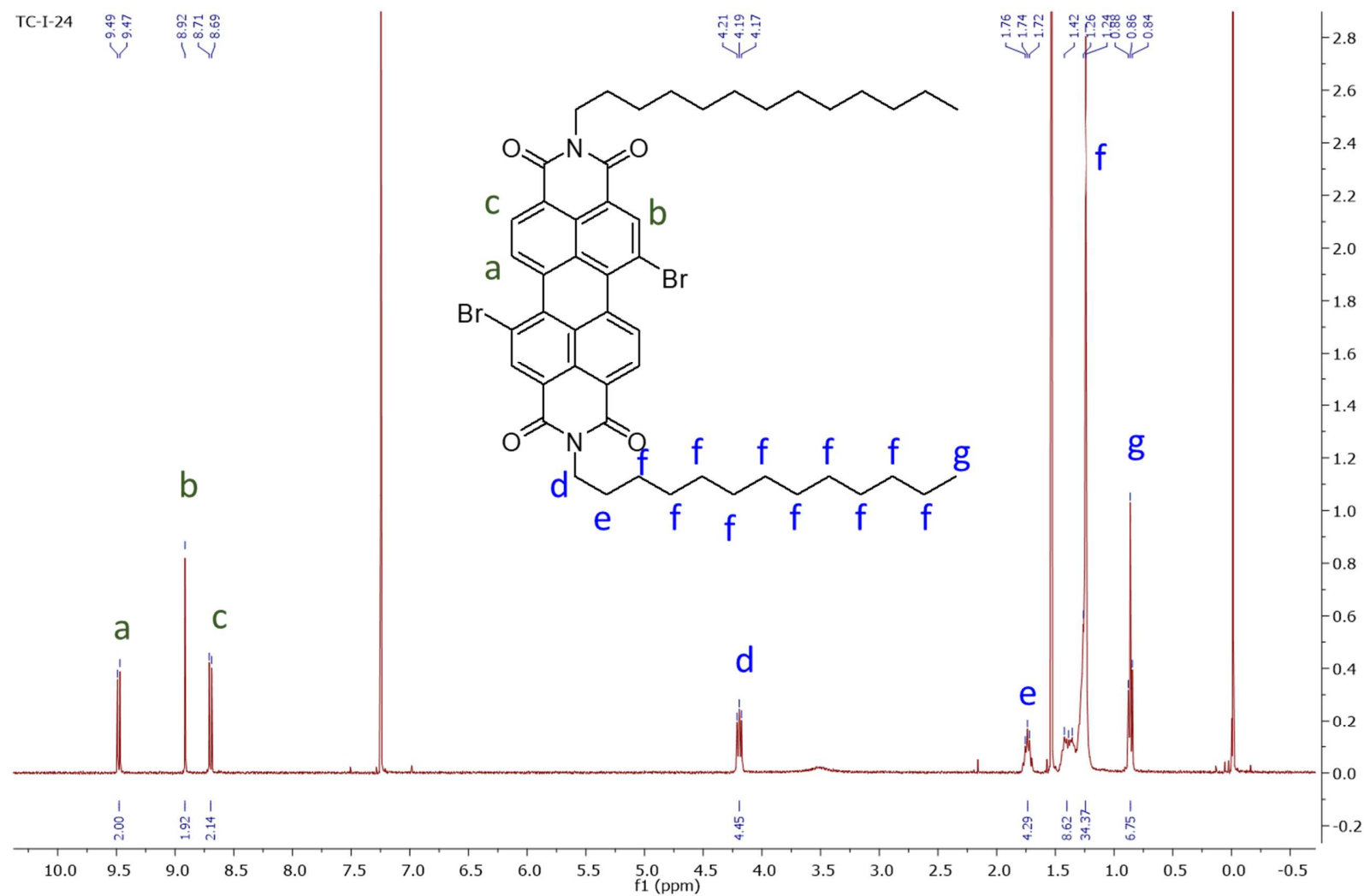


Figure S. 2.3.3.1.1 ¹H-NMR spectrum of 1,7-dibromo-*N,N*-ditridecyl-perylene-3,4,9,10-tetracarboxylic diimide (DB-PTCDI-C13)

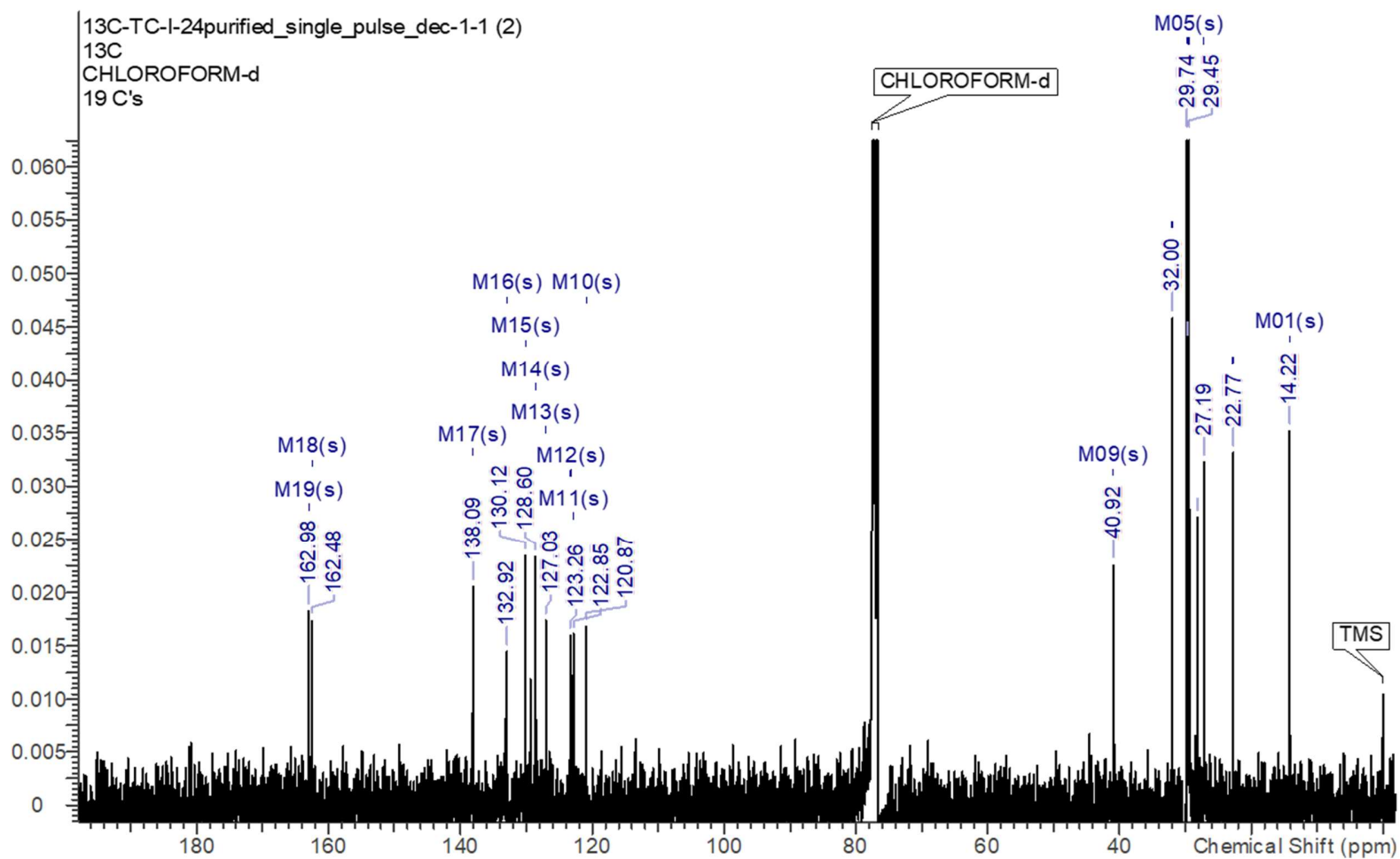


Figure S. 2.3.3.1.2 ^{13}C -NMR spectrum of 1,7-dibromo-*N,N*-ditridecyl-perylene-3,4,9,10-tetracarboxylic diimide (DB-PTCDI-C13)

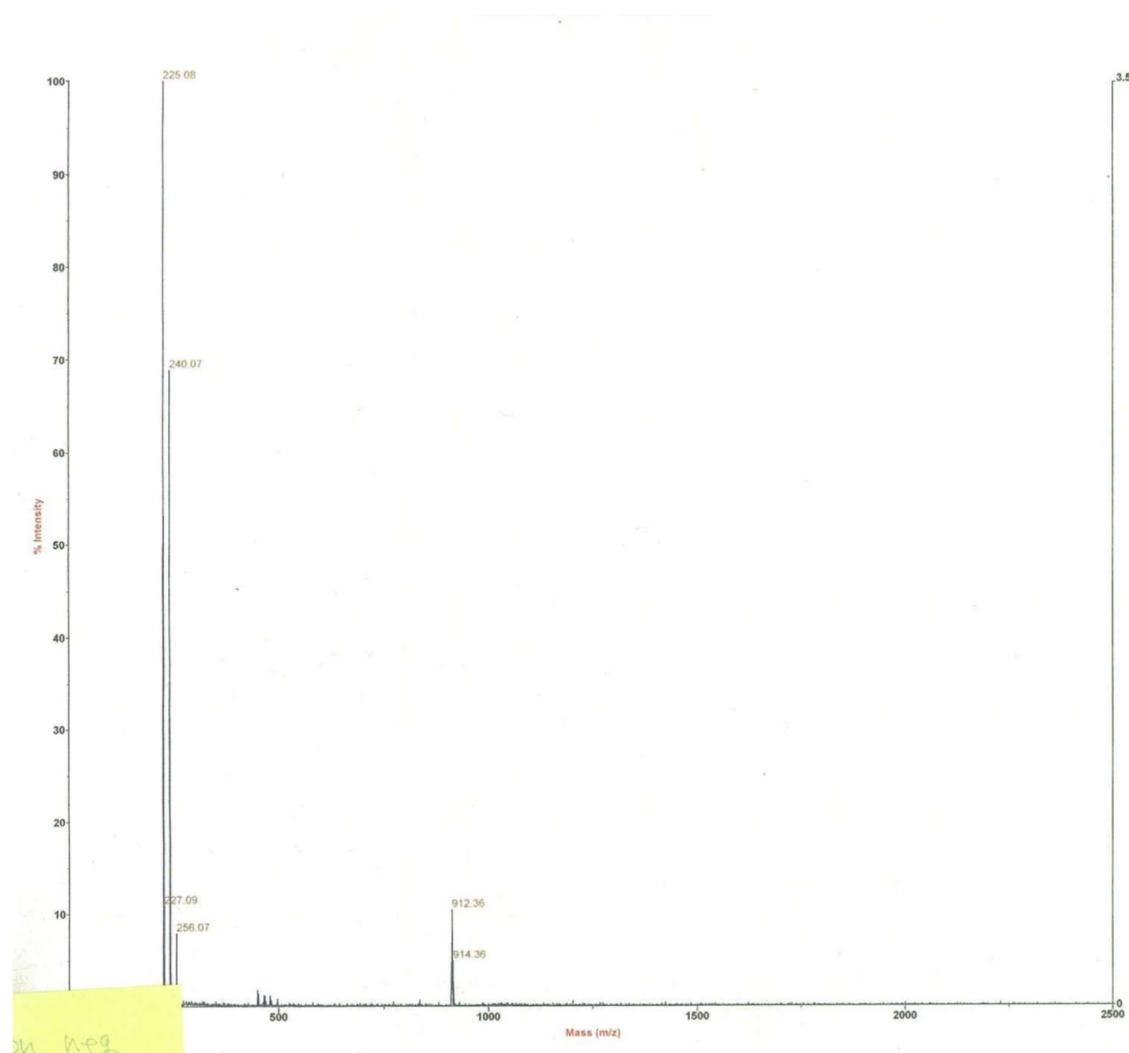


Figure S. 2.3.3.1.3 MALDI-TOF mass spectrum of 1,7-dibromo-*N,N*-ditridecyl-perylene-3,4,9,10-tetracarboxylic diimide (DB-PTCDI-C13)

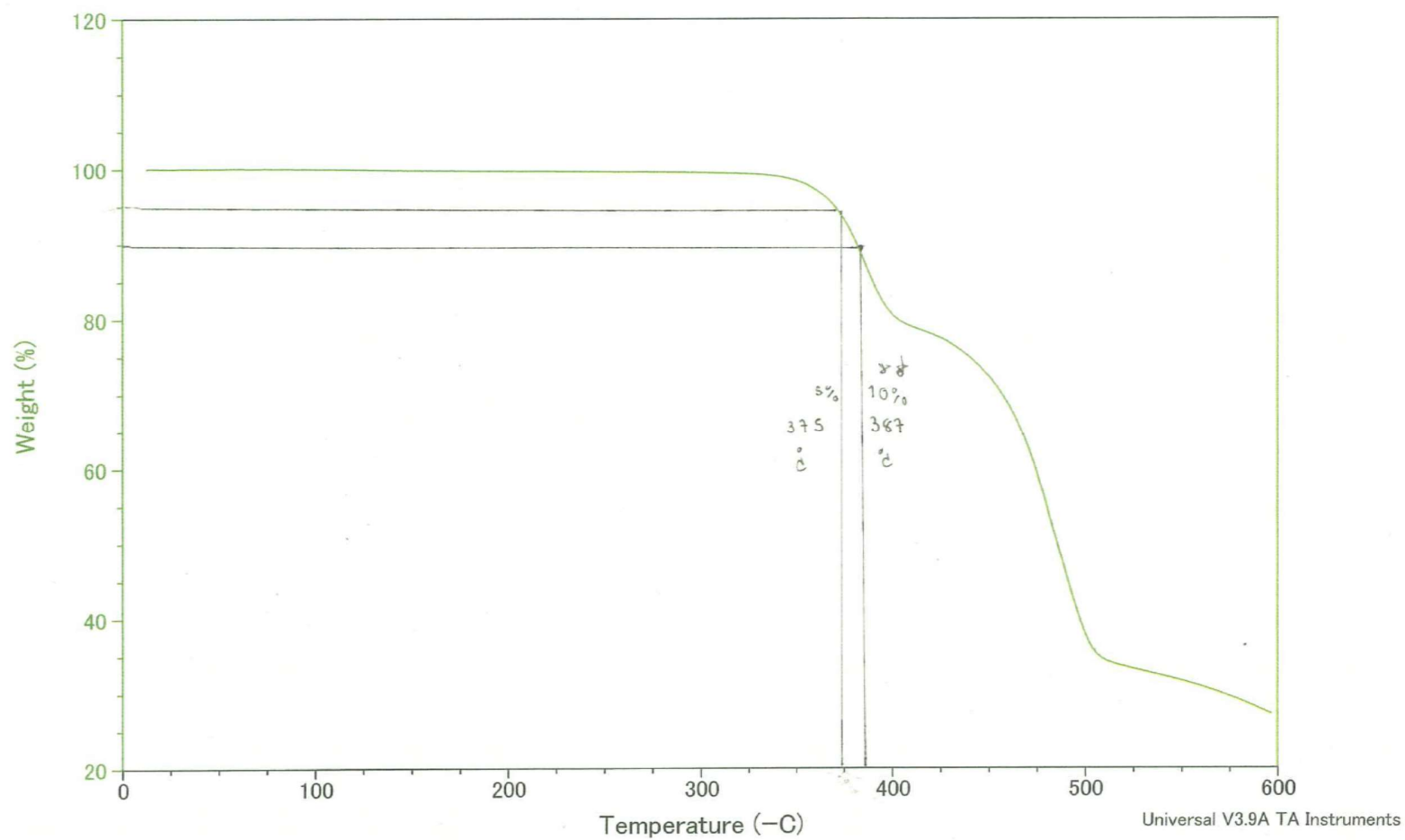


Figure S. 2.3.3.1.4 TGA thermogram of 1,7-dibromo-*N,N*-ditridecyl-perylene-3,4,9,10-tetracarboxylic diimide (DB-PTCDI-C13)

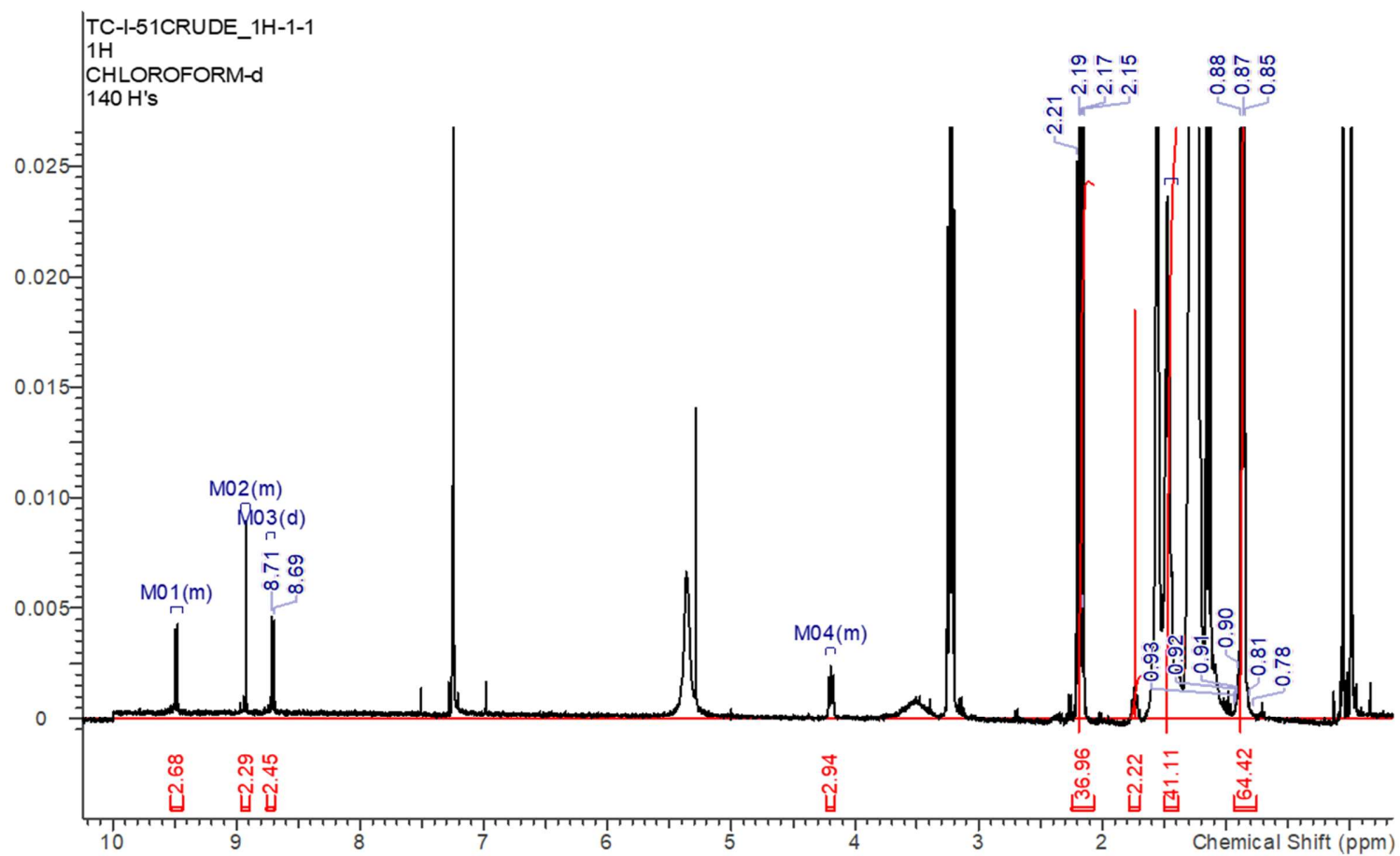


Figure S. 2.3.4.1.1 ^1H -NMR spectrum of 1,7-dibromo-*N,N*-dioctadecyl-perylene-3,4,9,10-tetracarboxylic diimide (DB-PTCDI-C18)

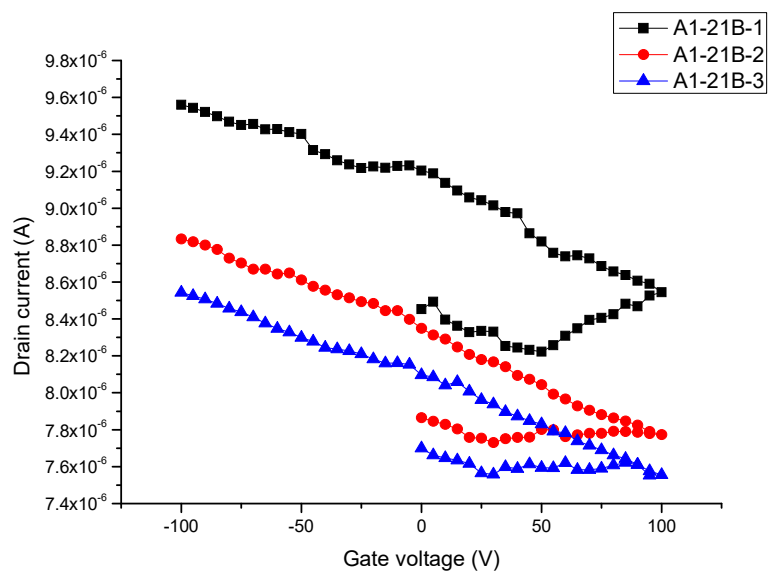


Figure S. 3.3.2.2.1. Result K-TCNQ by recrystallization method without annealing of device 1 at 30 μm

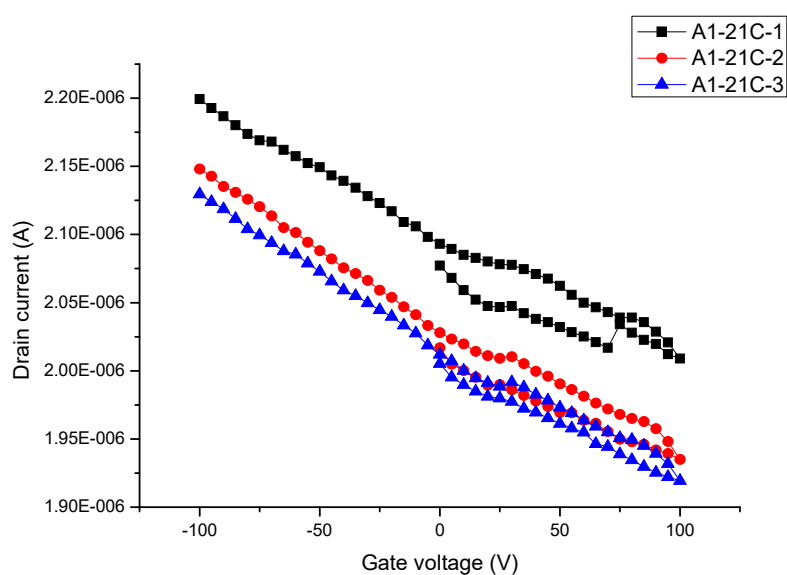


Figure S. 3.3.2.2.2 Result K-TCNQ by recrystallization method without annealing of device 2 at 30 μm

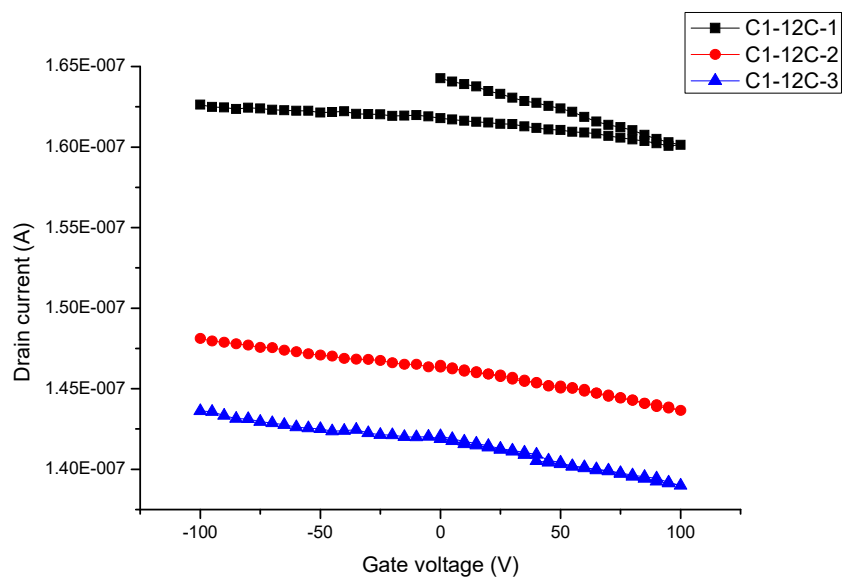


Figure S. 3.3.2.2.3 Result K-TCNQ by recrystallization method without annealing of device 3 at 30 μm

Acknowledgement

This work was partially supported by JSPS KAKENHI (Grant Nos. JP16H04140), JST ERATO (JPMJER1301), MEXT Nanotechnology Platform Program (Molecule and Material Synthesis), and Equipment Development Center (Institute for Molecular Science). T.C. thanks MEXT scholarship for foreign students.

I would like to thank you Professor Hiroshi Yamamoto, Ph.D. my advisor, Assistant Professor Masayuki Suda, Ph.D., my co-advisor, and the team members from Research Center of Integrative Molecular System (CIMoS) for supporting my thesis. Not only giving me an opportunity to study and achieve this research, Professor Hiroshi Yamamoto also provides me MEXT scholarship, from Ministry of Education, Culture, Sport, Science and Technology (MEXT), Japan.

Furthermore, this thesis would not have been accomplished without many precious and valuable advice and comments from all my thesis committee.

Ultimately, I am most grateful to my mother, my aunt, Ms. Sophin, and all family members for their personal supports at all times.

List of Publications

Chapter 2 Development of monolayer n-type field-effect-transistor

Tianchai Chooppawa, Masayuki Suda, Mikio Uruichi, Manaschai Kunaseth, Supawadee Namuangruk, Paitoon Rashatasakhon and Hiroshi M. Yamamoto, “Development of highly soluble perylenetetracarboxylic diimide derivative for n-type monolayer field-effect-transistor”

Molecular Crystals and Liquid Crystals (Accepted)

(Included in this thesis)

Other Publications

Tianchai Chooppawa, Mongkol Sukwattanasinitt, Somboon Sahasithiwat, Vithaya Ruangpornvisuti and Paitoon Rashatasakhon, “Substituent effect on quantum efficiency in 4-aryloxy-*N*-(2' , 6'-diisopropylphenyl)-1,8-naphthalimides: Experimental and computational investigations”,

Dyes and Pigments. **2014**, *109*, 175.